INTERNAL ATOMIC-SCALE STRUCTURE AND PHOTOTHERMAL DYNAMICS OF HETEROSTRUCTURED NANOMATERIALS

BY

CECILIA MARIE GENTLE

DISSERTATION

Submitted in partial fulfillment of the requirements
for the degree of Doctor of Philosophy in Chemistry
in the Graduate College of the
University of Illinois at Urbana-Champaign, 2020

Urbana, Illinois

Doctoral Committee:

Assistant Professor Renske van der Veen, Chair
Professor Catherine J. Murphy
Assistant Professor Josh Vura-Weis
Professor Moonsub Shim

Abstract

In this thesis we adopt a multimodal materials characterization approach to unravel the internal structure and the photoexcited electronic and geometric structural dynamics of $Cd_xZn_{1-x}Te$/CdSe core/shell quantum dots (QDs). These QDs belong to a broader class of heterostructured II-VI semiconducting that are known for their applications in optoelectronics and biomedical imaging.

The foundation of this thesis is the determination of the internal structure of II-VI core/shell quantum dots (CSQDs) using a combination of several characterization modes, with X-ray absorption spectroscopy (XAS) as a crucial element-specific technique. Through a combination of optical spectroscopy, electron microscopy, elemental analysis, and the global analysis of the extended X-ray absorption fine structure (EXAFS) spectrum, we show that the intended ZnTe/CdSe CSQDs, that are synthesized using a common one-pot synthesis procedure, are in actuality nanoparticles with an alloyed core and a patchy CdSe shell. Electronic structure calculations show that the CSQDs essentially behave as one-component QDs with a direct band gap. Cation exchange and the unintended reaction of molecular precursors prevent the formation of a sharp type-II ZnTe/CdSe interface with small lattice mismatch. Instead, the large interfacial strain between $Cd_xZn_{1-x}Te$ ($x = 0.8$) and pure-phase CdSe leads to the growth of islands on the QD surface. Our results corroborate the challenges associated with the synthesis of Zn/Cd chalcogenide type-II heterostructures due to facile ion exchange. This study is an example of how the assessment of heterogeneous nanomaterials on the basis of spectroscopy or size analysis alone is not always sufficient. While our XAS data were obtained at a large-scale synchrotron X-ray facility with specialized infrastructure and limited access, the advent of tunable high-brightness table-top X-ray sources will enable characterization studies on heterostructured photovoltaic and photocatalytic nanomaterials with much higher throughput and more experimental flexibility.

We use density functional theory in combination with state-of-the art theoretical XAS

codes to demonstrate the sensitivity of the X-ray absorption near-edge structure (XANES) to the local structure beyond the first coordination shell. In this way, we are able to corroborate the structural characterization of the alloyed $Cd_xZn_{1-x}Te$ ($x = 0.8$) core as determined by EXAFS analysis. This work underscores the power of XAS, in both experiment and simulation, for understanding the internal structure of heterogeneous nanoparticles.

Ultrafast XAS is a powerful tool to unravel the electronic and geometric structures of photoexcited materials with femtosecond (fs)-nanosecond (ns) resolution. Using systematic DFT-based XAS simulations, we show that the time-resolved XANES spectra of nanoparticles at early time delays after photoexcitation ($\backsim$90 picoseconds, ps) are dominated by thermal effects, such as a 0.2% lattice expansion and disorder, while spectra at later times ($\backsim$2.5 ns) have clear signatures of excited carriers. In combination with heat diffusion simulations we derive the heat interface conductance 7-15 $MW/m^2/K$ for the colloidal $Cd_xZn_{1-x}Te/CdSe$ nanoparticle sample. Application of ultrafast XAS and the data analysis methods to other nanomaterials is an exciting perspective; in particular, in view of the recent development of intense free electron laser sources delivering $\backsim$100 fs X-ray pulses. These state-of-the-art facilities open new opportunities for exploring photoinduced electronic properties of semiconductor nanomaterials on the ultrafast time scale.

Acknowledgements

First and foremost, I must thank my advisor, Professor Renske van der Veen for her guidance throughout my PhD thesis work. I want to thank all my past and present labmates. In particular, I thank Yuanheng Henry Wang. Henry, much of this work would not have been possible without you and you have a bright future ahead of you. Conner Dysktra, Tyler Haddock, Ryan Cornelius, Rachel Wallick and Allan Sykes: thank you for traveling to the synchrotron with me, for sacrificing your sleep, and for dropping everything to help me in moments of need. Thank you for thinking creatively with me to solve problems at the drop of a hat, often at 4 am. Most of all, thanks for your good humor and having fun with me during beam times. Beam times were the most challenging experience of my PhD, but you all also made them also the most fun. Dr. Thomas Rossi, thank you for bringing you expertise of FDMNES to the group. Without your expertise, much of this work would not have been possible. Dr. Omid Zandi thank you for being a sincere and true friend. I will always treasure our deep and thoughtful discussions about life and philosophy. Thank you to Frank Alcorn, Oliver Lin, Jack Burke, Eric Thornburg, Sasha Lamtyugina, Pranav Ghatraju, Margo van Loon, Leo Hamerlynck, Thomas Dixon, Brittany Hagler, Jocelyn Lai, Allwell Worgu, Dr. Offir Cohen, Daniel Munteanu and Bogdan Dryzhakov. Thank you Professor André Schleife and Erick Hernandez Alvarez for being fantastic collaborators and teaching me about the intricacies of theoretical calculations.

I owe my deepest thanks to the AMO group past and present at the Advanced Photon Source including Dr. Don Walko, Dr. Anne-Marie March, Dr. Gilles Duomy, Dr. Andre Al Haddad, and Dr. Ming-Feng Tu. Thank you for all your help, guidance and patience. Thank you for sharing your knowledge and your willingness to push the limits of the beam line's capabilities to help in my experiments. I also owe many thanks to the SCS Machine Shop and the staff scientists at the Materials Research Laboratory Central Facilities for their patience and expertise in training me and for assisting me in so much of this thesis work. Thank you

Dr. Julio Antonio Nieri D. Soares, Dr. Waclaw Swiech, Dr. Richard T. Haasch, and Dr. Jim Mabon.

Thank you to Dr. Michael Enright, Dr. Danielle Henckel, and Dr. Leslie Hamachi for fruitful scientific discussions. Thank you Dr. Jessica White for your mentorship. I thank the Dr. Nuzzo and his lab for hosting my synthetic set up during my PhD. I would be remiss in not also thanking Dr. Girolami and Dr. Brain Trinh for hosting me in their lab during construction of the Nuzzo lab.

I am so grateful for the warm and welcoming IMP office past and present: particularly Theresa Struss, Karen Watson, Stacy Walker, Beth Myler, Katie Trabris, Connie Knight. Thank you all for being my friend. I also thank my funding sources: Springborn Fellowship and NSF Graduate Fellowship Research Program. I am grateful for Dr. Robert and Carolyn Springborn for their endowment which supported my thesis work over the last 5 years.

Through my experience as an analyst the Office of Technology Management at UIUC, I've discovered that I am passionate about helping brilliant science change the world. Thank you to all at OTM. I am especially thankful for Nathan Hoffmann, Brad Edwards, Heather Jones, Dr. Michelle Chitambar, Maria Jaromin, Dr. Kwaku Opoku, Jeff Wallace, Dr. Svetlana Sower, Dr. Mariana Lencina, and Dr. Stephen Fleming. I am so excited to continue working with OTM in my new role! I also an indebted to Dr. Catherine and Dr. Don Kleinmuntz, thank you for your mentorship. You both are inspirations to me.

Serving on the boards of graduate student committees was one of the most rewarding and fulfilling experiences of my PhD. Thank you to all my colleagues who served on the board of DCGSAC and WCC with me. To my undergraduate professors and resaerch mentors, thank you for believing in my potential: Dr. Jerry Cohen and Dr. Adrian Hegeman at UMN, Dr. Song Jin at UW Madison, Dr. Loredana Latterini and University of Perugia, and Dr. Debby Filler, Dr. Patty Pieper, and Lance Lund at Anoka-Ramsery Community College.

There are many friends to thank and I regret that cannot name them all here, but I owe my deepest and sincerest gratitude to Dr. Matthew Hesson-McInnis. Thank you for

mentoring me and editing all my writing. I have lots of other cheesey things to say to you. Dr. David Stevens, Hannah Toru (Shay), Aastha Sharma, Kori Sye, Meredith Rickard, and many others, thank you for your fierce and formidable friendships.

Thank you Joe, your support has helped me in my most difficult moments. Your love is the greatest gift. Thank you to Mocha for being a loving and loyal companion. Above all else, I thank my parents and my brothers. Thank you Mom and Dad for everything. You taught me the value of hard work and education. I am privileged for your knowledge of the higher education system, which without a doubt made my PhD journey easier to navigate. More so, I am indescribably privileged because you always believed in my abilities and have always advocated for me.

Table of Contents

Chapter 1

Introduction

The aim of this thesis is to unravel the internal atomic-scale structure, band alignment, and charge transfer dynamics of ZnTe/CdSe core/shell quantum dots (CSQDs). To achieve this goal, we use a multitude of static and ultrafast characterization tools, and in particular this thesis highlights the use of X-ray absorption spectroscopy (XAS) for the aforementioned aim. This Chapter serves as a general introduction to the thesis topic. In Section 1.1, we provide introductory information to heterogenous quantum dots and specifically review the previous work done on ZnTe/CdSe CSQDs. In Section 1.2, we discuss the challenges in the characterization of nanoheterostructures. Next in Section 1.3, we give a synopsis of the challenges in modeling and simulation of the effects of alloying in XAS spectra. Finally, in Section 1.4, we discuss the use of picosecond-resolved XAS for studying the charge carrier dynamics in nanomaterials.

In Chapter 2, we provide the necessary theoretical background for the analysis of the X-ray absorption spectra in this thesis. Next, in Chapter 3, we provide the experimental and theoretical methods. Chapters 4, 5, and 6 present the results and original findings of this thesis, which we summarize in Sections 1.2, 1.3, and 1.4 of this Chapter.

1.1 Quantum dots

Colloidal semiconductor nanocrystals, that is, quantum dots (QDs), exhibit size-, shape-, and composition-dependent optoelectronic properties due to their quantum-confined (excited) states (Figure 1.1a). Their tunability and synthetic flexibility make them ideal candidates for applications in solar energy harvesting, biomedical imaging, photocatalysis, light emit-

ting devices, and quantum computing.[1–3] QDs exhibit quantum confinement because their particle radius is less than the Bohr radius of the bulk material. The result is simple band gap tunability based solely on controlling the QD size. Colloidal synthesis techniques, where QDs are dispersed in solution using organic ligands, can be performed in controlled batches or continuous reactor processes and easily manipulated for later processing or incorporation into optoelectronic devices.[4–6]

1.1.1 Core/shell quantum dots

QD heterostructures, such as CSQDs, combine the quantum confinement effect with composition control and can be tuned to emit across the entire visible spectrum and into the infrared (Figure 1.1b).[9–14] Compared to pure-phase QDs, CSQDs exhibit two additional degrees of freedom for tuning the energetics of the nanoparticle: the shell material and thickness. The flexibility can lead to three main types of band alignment: type-I, type-II, and pseudo type-II (Figure 1.2). In type-I heterostructures, the band gap of one material is encompassed within the band gap of the other material, which confines excited charge carriers (electrons, holes) exclusively within the material containing the smaller band gap. The overlap of the electron and hole wavefunction increases the probability of radiative recombination. The high quantum yields in type-I CSQDs as compared to single component QDs make them

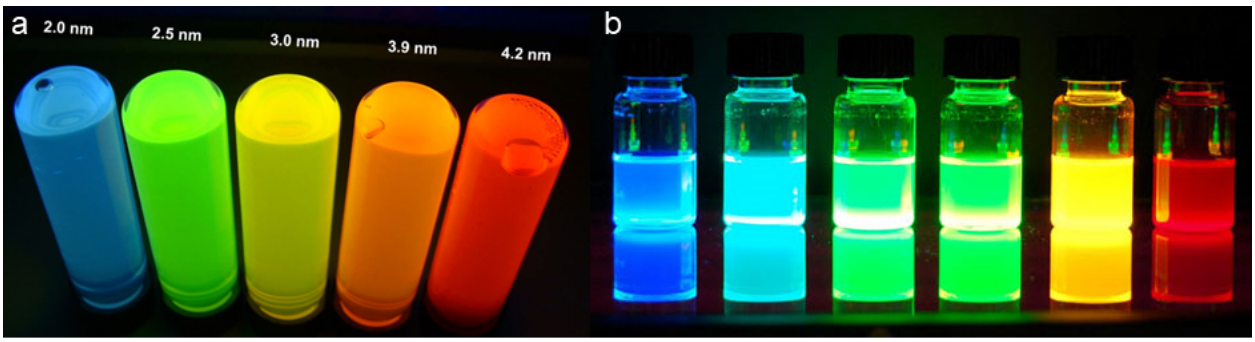

Figure 1.1: (a) CdSe QDs of different sizes. The wavelength of their luminescence is dependent on the size of the QDs. Reproduced and modified from Reference 7. (b) Photoluminescence of alloyed CdS_xSe_{1-x}/ZnS quantum dots of 6 nm diameter. The material emits different colors of light by tuning the composition. Reproduced and modified from Reference 8.

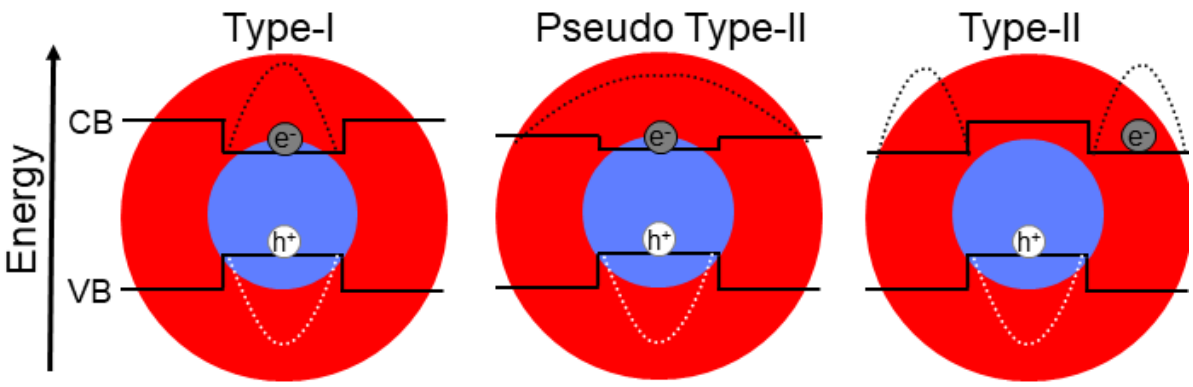

Figure 1.2: Schematic representation of type-I, pseudo type-II and type-II band alignment and carrier localization in CSQDs. The black lines indicate the band edge positions in the core and shell materials. The black and white dotted lines depict the electron and hole envelope functions, respectively.

excellent candidates for biomedical imaging applications and light emitting devices.[2,3] In type-II structures, the band energies have a staggered band alignment, which can result in separation of carriers across the material interface benefitting charge extraction towards the electrodes in a photovoltaic device. In fact, the wave function engineering approach in CSQDs[15,16] that makes use of epitaxial strain and alloying through ion exchange reactions has, for example, led to enhanced photoluminescence quantum yields,[10,11] reduced charge carrier recombination,[17,18] and their use as luminescent solar concentrators.[19,20] Generally in pseudo type-II CSQDs, one carrier is confined to one domain while the other is delocalized across the whole structure. For example, when the offset between the conduction bands of the two materials is significantly smaller than the offset between the valence bands, the electron is delocalized across the whole structure and the hole is localized to the valence band of only one domain. The delocalization of one carrier reduces wavefunction overlap which leads to longer carrier lifetimes, similar to type II alignment

1.1.2 Importance of strain and alloying at interfaces

The extremely high surface area to volume ratio of QDs means that defects at the surface (such as electronic trap states induced by dangling bonds, especially hole traps on unpassi-

vated chalcogen atoms[21–23]) can significantly affect the quality of the QDs.[24] On the other hand, much higher strain can be tolerated in small nanocrystals compared to the bulk. Smith *et. al* showed that lattice strain can significantly affect the location of charge carriers, excited state lifetimes, absorption and emission peaks.[25] For example, materials with type-I band alignment in the bulk and in relaxed nanostructures can be converted to type-II band alignment under strain. Additional control over the spatial distribution patterns of charge carriers is achieved by varying the structure of the heterojunction itself, in other words, making it epitaxial and sharp or alloyed and smooth.[9,26–33] Theoretical and experimental studies have shown that alloyed interfaces due to cation exchange can lead to decreased Auger recombination lifetimes.[34,35]

1.1.3 Review of ZnTe/CdSe Core/Shell Quantum Dots

ZnTe/CdSe CSQDs are the material of interest for this thesis. ZnTe/CdSe CSQDs have been proposed as a promising type-II heterostructure due to the very small lattice mismatch between the ZnTe and CdSe zinc blende crystal structures (0.8%, Figure 1.3).[36] The large conduction band offset between ZnTe and CdSe minimizes overlap between electron and hole carriers,[37,38] enhances photovoltage[39] and enables tunable emission in the near-IR.[36,40,41] The majority of previously reported synthetic procedures for colloidal ZnTe/CdSe CSQDs rely on the successive ion layer adsorption and reaction (SILAR) method.[36,39,40] In SILAR, the alternation of successive injections of elemental precursor solutions is used to control shell growth and avoid the formation of pure QD byproducts, ideally growing single monolayers of material per injection cycle. However, under reaction conditions that are prevalent in SILAR synthesis of colloidal CSQDS, specifically the elevated temperatures and the presence of excess precursors, competing reactions such as ion exchange[42] and unintended precursor reactions and growth may occur.

Xie *et. al* first proposed a synthetic method for ZnTe/CdSe CSQDs in 2005[36] and there has been interest in synthesizing ZnTe/CdSe CSQDs since.[38–40,42,43] A red shift in absorption

is commonly reported as the nanoparticles grow in size, which is attributed to increased charge transfer character across the core-hole interface as a result of the hole and the electron each becoming more localized to the core and the shell, respectively.[36,38,43] The increase in shell thickness is assumed, but we will show in Chapter 4 that alloying and incorporation of excess precursors can also be responsible for this.

More recent papers have studied the inhomogeneous outer surface and possible gradient interface due to cation exchange.[38,43] Jiang *et al.* asserted that the inhomogeneity of the shell thickness must be taken into account in interfacial charge transfer dynamics.[43] Hole transfer rates were studied by coupling a molecular quencher (phenothiazine) to the surface of the QDs. Much higher than predicted hole quenching rates lead the authors to conclude that the QDs have a rough surface, which is unexpected since ZnTe and CdSe have very small lattice mismatch (0.8%). The much larger mismatch (6%, Figure 1.3) and resulting increased strain at the CdTe/CdSe interface instead could be responsible for island type

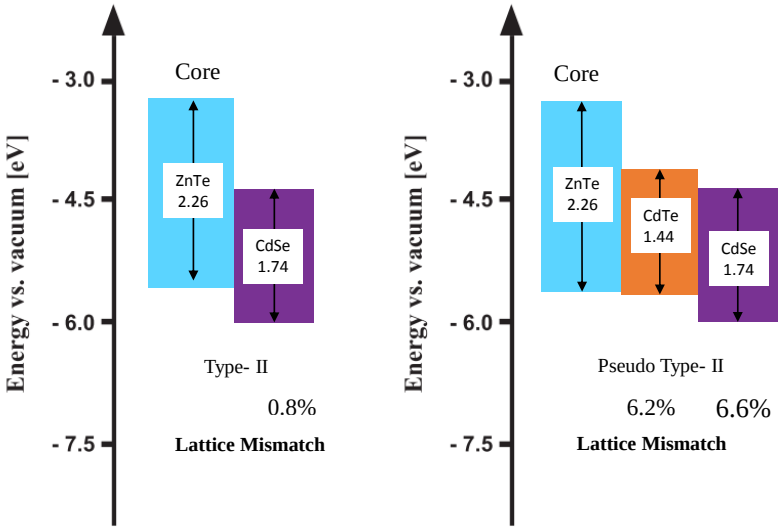

Figure 1.3: Bulk values of the band-edge positions and band gaps for different II–VI semiconductors. On the left is the band offset and lattice mismatch for the ideal ZnTe/CdSe heterostructure. On the right is the band offset and lattice mismatch for a ZnTe/CdTe/CdSe heterostructure. The lattice mismatch values at the interfaces are much higher with the incorporation of CdTe into the structure. The band offsets and lattice mismatch (in %) are given relative to ZnTe. Reproduced and modified from Reference 36.

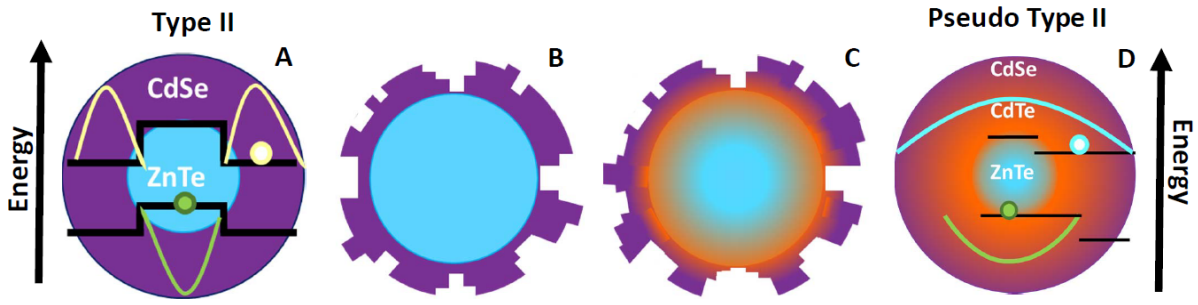

Figure 1.4: Proposed ZnTe/CdSe core/shell structures in the literature. Schematic showing the various structures proposed for ZnTe/CdSe core/shell QDs. Structure A is the proposed Type II by the original synthesis with a hard interface between the core and the shell.[36] Structures B[43] and C[38] proposes a rough shell. Structure C shows the affects of cation exchange creating an CdTe intermediate layer due to annealing.[38] Structure D[42] is based on ICP-MS elemental ratios which show the CdTe intermediate layer as the dominate species in the QDs and thus proposes a pseudo type-II band alignment.

growth on the surface of the particles. The authors speculate the presence of CdTe due to cation diffusion during the synthesis (reaction temperature 240°C) which results in a particle composition of ZnTe/CdTe/CdSe with gradient alloying at the interfaces. This structure is speculated, however, with no direct structural information to support this claim and no mention on how this varied structure would affect the band structure and the modeling of hole transfer dynamics.

In follow up studies,[38] hole transfer rates were studied again, but this time the authors annealed the CSQDS to understand the effect of cation exchange. The SILAR reactions were performed at 215 °C and then annealed at higher temperatures (240 °C). The annealed particles have nearly identical quenching and PL decays as CSQDs with no annealing. The shell morphology is an equilibrium that is determined by a combination of lattice strain and surface energies. Annealing or changes in the deposition temperature does not significantly change the morphology. More recently, quantification of elemental composition reveal that ZnTe/CdSe CSQDs synthesized by SILAR methods are actually largely CdTe.[42] The final elemental ratios of Zn:Cd:Te:Se were 1.0:8.6:7.4:1.7 starting with ZnTe cores of 1.0:0.5 Zn:Te.[42] We summarize the various structures for ZnTe/CdSe CSQDs in the literature prior to the work in this thesis in Figure 1.4.

1.2 Characterization of nanoheterostructures

Despite the myriad of synthetic and theoretical approaches that have recently been put forward to control the properties of heterostructured nanomaterials, their internal atomic-scale characterization remains challenging. Optical methods such as ultraviolet/visible (UV/vis) spectroscopy and photoluminescence (PL) are indispensable; but without much *a priori* knowledge about the heterostructure, the assignment of spectroscopic features can be ambiguous. Structural tools such as X-ray diffraction (XRD) provide information about the crystal symmetry and lattice spacing, but due to nanocrystal size broadening effects, structural subtleties such as strain and alloying remain hidden.[44] Angle-resolved X-ray photoelectron spectroscopy (XPS) was applied in the characterization of heterostructured nanomaterials,[44,45] but it has the drawback that the relatively small attenuation length of the photoelectrons limits the layer/shell thickness that can be studied. Recently, atom probe tomography (APT) has been used in the three-dimensional reconstruction of core/shell nanoparticles.[46–48] Although this technique is powerful and promising, the sample preparation and experiment procedures for nanoparticles are challenging.[49] Finally, whereas high-resolution electron microscopy has been successfully applied in the characterization of heterostructured nanomaterials,[46,50–53] its use for core/shell QDs is limited due to their spherical symmetry, especially in the case of semiconducting materials with similar lattice spacing, similar atomic Z numbers, or both.

In Chapter 4, we address the above challenges and make use of XAS in the construction of atomic-scale structural models of CSQDs. XAS is ideally suited for probing the internal structure of multicomponent materials because of its elemental specificity and sensitivity to local structure surrounding the absorbing atom.[54–61] In particular, the use of extended X-ray absorption fine structure (EXAFS) region of the XAS spectrum can allow us to ascertain coordination numbers, distinguish between types of scattering atoms, calculate bond lengths, and determine bond angles in the local (6 Å) environment of the absorbing atom

in alloyed semiconductor materials.[62–69] We apply a multimodal approach based on UV/vis spectroscopy, transmission electron microscopy (TEM), elemental analysis, and XAS to determine the internal structure of intended II-VI ZnTe/CdSe core/shell nanoparticles. We show that ZnTe/CdSe CSQDs synthesized according to the commonly employed SILAR method[36] are in actuality alloyed $Cd_xZn_{1-x}Te$/CdSe core/shell quantum dots. We studied the local structure of each elemental component of these complex nanoparticles by individually probing the Zn, Te, Cd, and Se X-ray absorption K-edges. By combining our XAS results with TEM sizing and elemental analyses, we propose models of the internal particle structure for a range of samples synthesized with different numbers of SILAR cycles. Our multimodal characterization approach confirms (1) the abundance of Cd-Te bonds, (2) cation alloying in the particle core (and the absence of anion alloying), (3) significant particle growth due to unreacted precursors, and (4) a patchy pure-phase CdSe shell. We extend our structural analysis with electronic band structure calculations and UV/vis absorption spectroscopy, demonstrating that the alloyed $Cd_xZn_{1-x}Te$/CdSe CSQDs behave as type-I materials with a direct band gap, different from the predicted type-II band alignment of the intended ZnTe/CdSe CSQDs.

1.3 Simulating X-ray absorption spectra of alloys

While EXAFS only probes the first-shell bond lengths, XANES is sensitive to local electronic structure and long-range multiple scattering effects (up to ~ 10Å from the absorbing atom).[70] XANES also is less affected by structural disorder relative to EXAFS, the interpretation of which becomes more complicated with highly disordered materials, like nanomaterials.[70–74] Analysis and simulation of XANES has made a significant contribution to the identification of the occupation sites of dopants in nanostructured semiconductors.[75–81]

Chapter 5 we implement *ab initio* XANES simulations as a way to corroborate the structural characterization of the alloyed $Cd_xZn_{1-x}Te$ core using EXAFS, TEM and elemental

analysis in Chapter 4. We employ density functional theory (DFT) to relax a supercell of a representative $Cd_xZn_{1-x}Te$ (x=0.8) alloy. The supercell is used as an input structure in Finite Difference Method Near Edge Spectroscopy (FDMNES) program, the DFT-based X-ray spectroscopy simulation code used in this work. The simulation of the XANES spectrum of the alloy supercell is in agreement with the experimental spectrum. Due to difficulty in controlling the synthesis of the alloy and limited access to large-scale X-ray facilities, we were not able to experimentally determine which features in the XANES spectrum are a result of alloying. Through simulation, however, we easily varied the composition of the supercell and showed via simulation which XANES features may be due to alloying. This thesis highlights the synthetic challenges associated with accessing colloidal type-II II-VI heterostructures[42] and the power of XAS for understanding the internal structure of heterogeneous nanoparticles.

1.4 Charge carrier dynamics in nanomaterials

In the optoelectronic application of quantum dots, whether for the purposes of charge separation (*e.g.* photovoltaics) or for radiative recombination (*e.g.* LEDs or biomedical imaging), it is crucial to understand the creation, transport, and trapping of the photogenerated holes and electrons over a wide distribution of time and length scales. Yet, the dynamics of these processes remain poorly understood, in part due to the complex interplay of structural and electronic effects that affect the various relaxation pathways. Furthermore, understanding how the thermal and electronic processes work together is important for improving the overall performance of QD based optoelectronic devices. Photovoltaics, QD based lasers, and LEDs often must perform at elevated temperatures. For example, the emissive layer of an LED typically experiences temperatures of 85–150°C.[82] Elevated temperatures, however, reduce device performance and QD integrity.[83]

Pump-probe experimental techniques have been developed to observe real-time evolution

of photochemical reactions. In this technique, a sample is first excited by a pulse of light (the pump) and then, after a short time delay, a second pulse of light (the probe) interrogates the excited sample. The properties of the dynamics that can be observed depend on the probe pulse. In ultrafast optical spectroscopy, both pulses lie in the ultraviolet to infrared region of the spectrum, and these optical pulses probe valence orbitals. However, signals become complex in condensed phase, in particular, suspension of nanomaterials. Optical spectroscopy also lacks information on atomic structure. X-ray transient absorption (XTA) is ideally suited for the study of nanoheterostructures due to its element specificity and combined local electronic and structural sensitivity.[84] As opposed to laser-only techniques, which often suffer from convolved signatures of carrier dynamics, X-ray spectroscopy offers the advantage of being able to unambiguously detect and characterize the electron and, most importantly, hole states separately.[84,85] While XTA has been extensively applied to molecular systems,[86–89] only very recently have applications in the field of nanoscience appeared.[90–100] Examples include the identification of trap states,[91,99] charge carrier separation,[90,92,94–97,100] and polaron formation.[100]

XTA spectroscopy on nanomaterials poses its own unique challenges. The mismatch of the absorption cross sections between the optical pump and the X-ray probe in solids leads to a smaller population of excited atoms relative to the total atoms in the sample compared to molecular systems.[101] Most of the sample is not excited by the pump laser, and thus much smaller transient signals are measured. As a result, the dilution of solid samples, such as in colloidal nanoparticle solutions, and an increase in laser fluence are necessary for achieving measurable signals in XTA experiments. The high fluences necessary also induce heating of the nanoparticles.

Many studies have been designed to understand the electronic charge carrier dynamics in QDs under high fluence conditions via optical studies.[102–108] Recently studies examining the nuclear structure of QDs under high fluence conditions via time-resolved X-ray and electron diffraction have emerged.[109–111] A recent review summarizes the optical and physical

probing of thermal processes in QDs.[83] Kischner *et al.* sought to identify optical signatures of transient thermal disorder in QDs. The combined local electronic and structural sensitivity of XAS, however, is well suited for understanding the interplay of photoinduced electronic and thermal processes in QDs. Thermal effects in XTA have only recently been explicitly discussed for thin film hematite and cuprous oxide materials.[112,113] The consideration of such effects for colloidal nanoparticle samples have been largely neglected. The current challenge in the field of XTA is to disentangle the signatures of both electronic and thermal dynamics in nanoparticles.

The motivation of Chapter 6 is therefore twofold: first, our results show that under excitation conditions prevalent in common XTA experiments, a large thermal response is expected, and sophisticated theoretical and analytical methods are needed to disentangle thermal from electronic effects in the spectra. Second, we show that with the right procedures in place, XTA can be used to characterize materials under high-carrier injection conditions and to determine, for example, the thermal interface conductance in colloidal nanomaterial samples.

Chapter 2

Theory of X-ray absorption by matter

This chapter provides the necessary theoretical background for the analysis of the X-ray absorption spectra of heterogeneous QDs described in Chapters 4-6. First in Section 2.1, we overview a general introduction to the interaction of X-rays with matter. XAS spectra can be split up into two regions: the X-ray absorption near edge structure (XANES) and the extended X-ray absorption fine structure (EXAFS). Because the theory involved in EXAFS spectroscopy is simpler than XANES, we cover EXAFS first in Section 2.2. Finally, in Section 2.3, we cover the theory of XANES spectroscopy as it relates to the Finite Difference Method Near Edge Spectroscopy (FDMNES) program which is the DFT-based X-ray spectroscopy simulation code used in this thesis work.

2.1 X-ray interaction with matter

X-rays are a form of electromagnetic radiation in the energy range from $\backsim$100 eV to $\backsim$200 keV, which corresponds to wavelengths in the range of $\backsim$10 nm to $\backsim$10 pm, respectively (Figure 2.1). X-rays can be either scattered or photoelectrically absorbed by matter. There are two kinds of X-ray scattering: elastic and inelastic. In inelastic scattering, part of the X-ray photon energy is transferred to an electron, and the scattered X-ray photon is lower in energy. In elastic scattering, the X-ray photon does not lose energy when scattering with an electron. Finally, in the X-ray photoelectron absorption process, the energy of the X-ray photon is transferred as kinetic energy to an electron, leading to an electronic excitation or ionization of the atom.

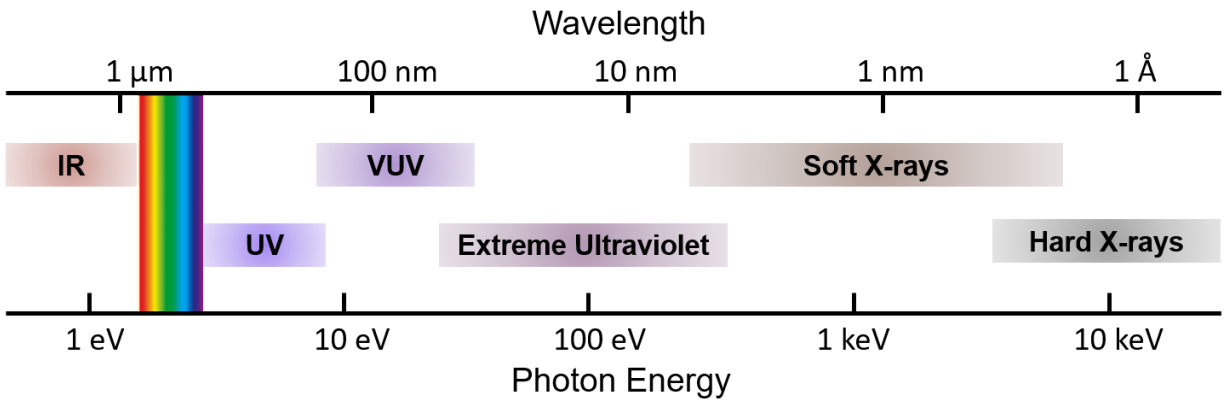

Figure 2.1: The electromagnetic spectrum. Reproduced and modified from Reference 114.

2.1.1 Absorption coefficients and cross-sections

The attenuation of an X-ray beam through matter follows Lambert-Beer's law, which takes a simple exponential form for a monochromatic X-ray beam transmitted through a homogeneous material:

$$I = I_0 \exp[-\mu x] \tag{2.1}$$

where I_0 and I are the initial and final X-ray intensity, respectively, μ is the material's linear attenuation coefficient (units 1/length) and x is the length of the X-ray path through the material. If the sample consists of several different materials in sequence, the argument of the exponential becomes a sum over the product of the material-specific attenuation coefficients

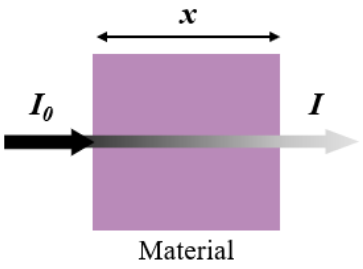

Figure 2.2: X-ray absorption and Lambert-Beer's law: the transmitted intensity I equals the incoming intensity I_0 times the exponential of the material's linear attenuation coefficient, μ, times the path length, x, through the material. (Eq. 2.1)

and path lengths:

$$I = I_0 \exp\left[\sum_i (-\mu_i x_i)\right] \ , \tag{2.2}$$

where each increment i reflects a single material with attenuation coefficient μ_i and path length x_i. μ incorporates the electron density and electron binding energy, which can be expressed in terms of a more fundamental, element-specific parameter, the atomic absorption cross-section, σ_a:

$$\mu = \rho_a \sigma_a = \left(\frac{\rho_m N_\mathrm{A}}{A}\right) \sigma_a = c_\mathrm{mol} N_\mathrm{A} \sigma_a \tag{2.3}$$

where N_A, ρ_m, A and c_mol are Avogadro's number, the mass density, the atomic mass number, and the molar concentration, respectively.

Figure 2.3 demonstrates the dependence of the atomic absorption cross-section on photon energy for the Zn atom. The absorption cross-section is approximately proportional to $1/E^3$, below and above the discontinuities. The discontinuities occur at characteristic energies and are known as absorption edges. We will discuss absorption edges in more detail in the

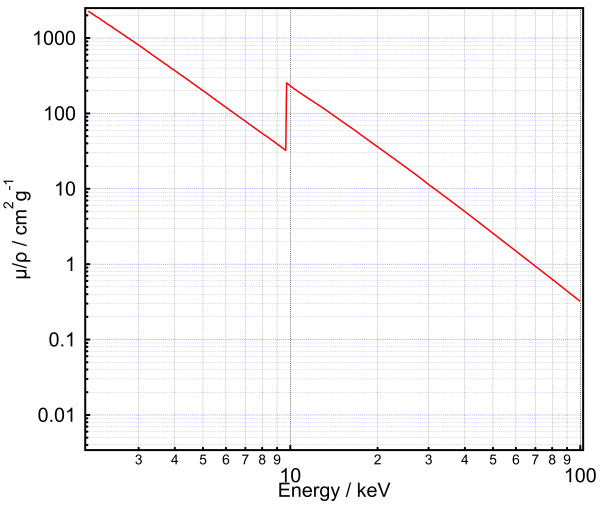

Figure 2.3: X-ray absorption cross-section for the element zinc as a function of photon energy. Note that both axes are in logarithmic scale and the nominal density, ρ, is 7.1120 g/cm^3. Data plotted from Reference 115.

following section.

2.1.2 Absorption edges

The discontinuities in the atomic absorption cross-section (Fig. 2.3) are characteristic to each element, and they occur when the X-ray photon has enough energy to eject an electron from an atomic core level. The electron can be promoted to either a valence orbital (a bound-bound transition) or to a quasi-continuum level above the ionization energy. For the bound-bound transitions, optical dipole selection rules ($\Delta j = 0, \pm 1, \Delta m = 0, \pm 1$; ignoring spin) apply. The promotion of a core level electron to the quasi-continuum ionizes the atom and leads to the sudden increase of the absorption cross-section.

In this thesis, the absorption edges of interest are all known as K-edge transitions. X-ray edges still follow a now-outdated nomenclature for the shell model of the atom. As depicted in Figure 2.4, the K-edge transitions correspond to the excitation of an s-orbital

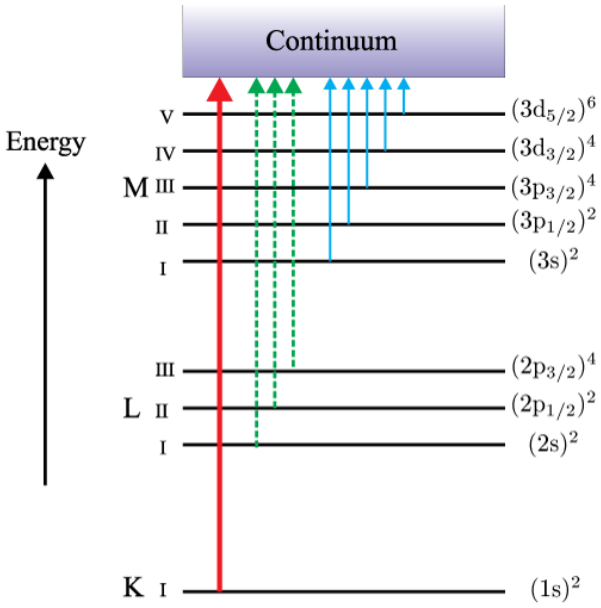

Figure 2.4: A schematic of the transitions for absorption edges and their corresponding labels. The K edge corresponds to the energy required to remove an electron from the 1s shell to the continuum of free states, etc. The electronic shells are labelled as $(\mathrm{n}l_j)^{2j+1}$, where n, l and j are the principal, orbital angular momentum, and total angular momentum quantum numbers, respectively, of the single-electron states. The multiplicity is $2j+1$. Reproduced from Reference 116.

electron, L edges correspond to p-level transitions, and-so-on. Due to the three sub-shells of the p-orbitals with different total angular momentum quantum number j, the L edges split into three levels. There are several qualitative trends for absorption edges:[117] (1) The energy difference between the sub-shells within each shell are always much smaller than that between the different shells; (2) The difference in energy between the successive absorption edges, K, L, M, ..., decreases with increasing principal quantum number, n; (3) The magnitude of the increase in the absorption cross-section (the so-called edge jump) generally decreases in going from low-to high-energy edges (e.g. $L_{III} > L_{II} > L_I >$K); (4) With increasing atomic number Z, the absorption edge energy increases, and the edge jump decreases.

2.1.3 X-ray relaxation processes

Following an absorption event, the atom is left with one of its core electron levels empty (a so-called core hole). The atom is in a high-energy excited state and relaxes within several femtoseconds through several mechanisms, as shown in Figure 2.5. Radiative decay, or X-ray fluorescence, occurs when an outer-shell electron fills the core hole and emits a photon equal to the energy difference between the two shells. The intensity of the emitted fluorescent X-rays is proportional to the number of core holes created and therefore to the absorption cross-section. The core hole can also be filled through non-radiative decay of a high-level electron while simultaneously ejecting another valence electron, referred to as an Auger electron. This process can be seen a one−step two−electron Coulombic readjustment to the initial core hole.[116]

XAS spectra can be split in two regimes: the X-ray absorption near edge (XANES) and the extended X-ray absorption fine structure (EXAFS). The energy at which the transition between XANES and EXAFS occurs is loosely defined as $\backsim$50 eV above the ionization edge. A representative XAS spectrum highlighting these two regimes is given in Figure 2.6. The XANES region is sensitive to both local geometric and electronic structure. EXAFS can ascertain coordination numbers, distinguish between types of scattered atoms and calculate

bond lengths in the local (∼6 Å) environment of the absorbing atom.

2.2 Theory of EXAFS spectroscopy

EXAFS refers to the oscillatory variation of the absorption coefficient as a function of photon energy starting ∽ 50 eV above an absorption edge. Oscillations in the absorption spectrum occur because the photoelectron scatters from neighboring atoms. The return of the scattered

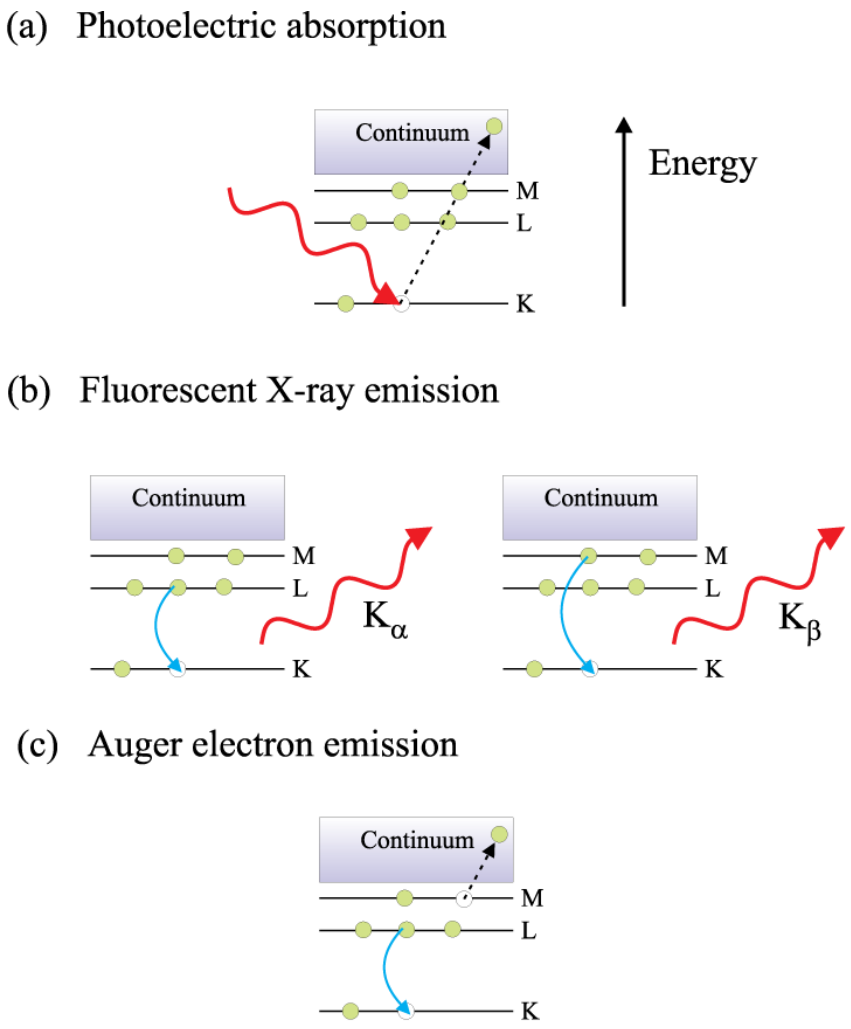

Figure 2.5: Schematic of relaxation processes after (a) X-ray photoelectric absorption. (b) In fluorescent X-ray emission, an electron in the outer shell fills the core hole and creates an X-ray photon. Depending on the level from which the filling electron originates, the emission is labeled K_α (L-shell) or K_β (M-shell). (c) An atom relaxes by emitting an Auger electron. The ejected electron can either originate from the same level as the electron that fills the core-hole, or from a higher-energy level. Reproduced from Reference 116.

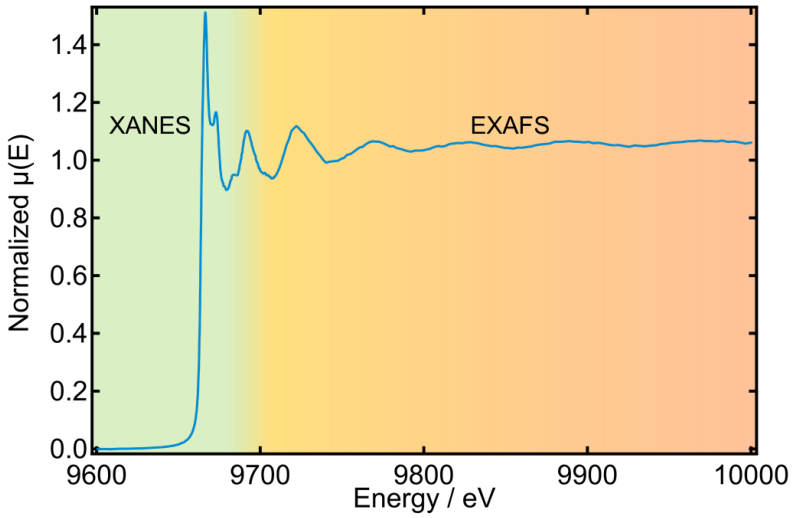

Figure 2.6: XAS spectrum of $Zn_xCd_{1-x}Te/CdSe$ nanoparticles illustrating the two regions: the low-energy XANES region up to $\backsim$50 eV above the ionization energy, highlighted in green, and the high-energy EXAFS region $\gtrsim$50 eV, highlighted in orange. The spectrum has been normalized to the edge jump as described in Section 2.2.1

photoelectron to the absorbing atom modulates the amplitude of the absorption coefficient $\mu(E)$ at the absorbing atom.[118] As such, EXAFS is a final-state quantum-interference effect involving scattering of the outgoing photoelectron from the neighboring atoms. The X-ray absorption cross-section obeys the Fermi golden rule, which is at the heart of any spectroscopy. The probability that an X-ray photon will be absorbed by a core electron depends on both the initial $|i\rangle$ and the final states $|f\rangle$ of the electron via the transition matrix element $\langle f|\hat{\varepsilon}\cdot\mathbf{r}|i\rangle$ where $\hat{\varepsilon}\cdot\mathbf{r}$ is the electric dipole operator. The initial state is the localized core level, while the final state is that of the ejected photoelectron, which is represented as an outgoing spherical wave with its origin at the absorbing atom. A simplified representation of the effect of a photoelectron scattering off a neighboring atom is depicted in Figure 2.7. The interference of all the reflected waves at the absorbing atom with the outgoing photoelectron wave modulate the matrix element that controls the strength of the transition (and thus the magnitude of $\mu(E)$). The phase difference between the two outgoing and incoming components is approximately $2k_{el}R$, where R is the distance to the neighboring atoms (in the case of a single-scattering pathway, *vide infra*) $k_{el} = 2\pi/\lambda_{el}$. Thus the de Broglie wavelength λ_{el}

decreases with increasing energy. The modulation in μ is a result of the constructive and destructive interference between these components as the photon energy is varied. The bonding, number, and type of neighboring atoms and their distances from the absorbing atom all modulate the amplitude and frequency of μ. There is, however, a maximum interatomic distance that can contribute to the interference pattern. Because of inelastic interactions of the photoelectron with the electrons and phonons of the surrounding atoms, the coherence of the waves is destroyed. If the photoelectron scatters off a neighboring atom only once (to and from), this is referred to as a single scattering (SS) pathway. In contrast, multiple scattering (MS) pathways are when the wave scatters off a neighboring atom two or more times before returning to the absorbing atom.

Within this picture, EXAFS can be phenomenologically described by the so-called EXAFS equation. Its derivation can be abundantly found in the literature.[116,118] Here we focus on the physical meaning of its various components and how the equation is used to extract structural information from the XAS spectrum. The EXAFS spectrum is defined as the normalized, oscillatory part of the absorption coefficient above a given absorption edge:

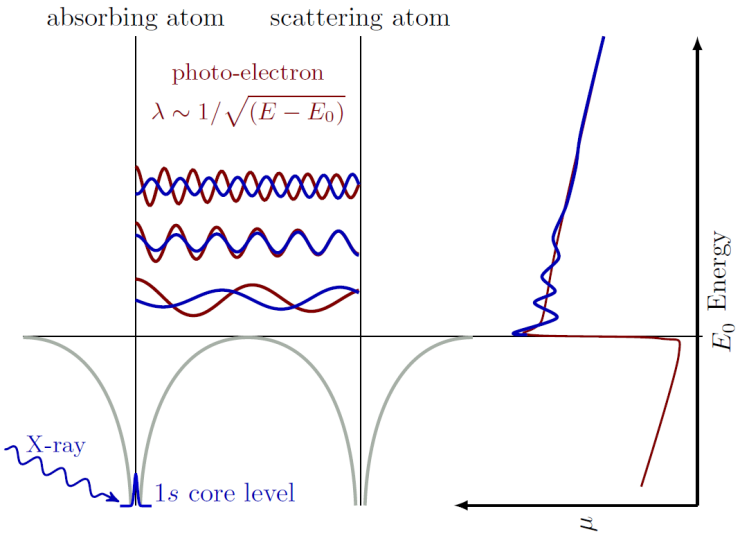

Figure 2.7: Schematic of oscillations in XAS as a result of the photoelectron scattering from a neighboring atom, modulating the amplitude of the photoelectron wave-function at the absorbing atom. Figure reproduced from Reference 119.

$$\chi(E) = \frac{\mu(E) - \mu_0(E)}{\mu_0(E)} \ , \tag{2.4}$$

where $\mu_0(E)$ is the smoothly varying atomic-like background absorption of an isolated atom, that is an atom in the absence of neighboring scatterers but incorporated in the lattice of neighboring potentials. The kinetic energy of the photoelectron is given by the difference in energy E of the X-ray photon and the ionization potential, E_0, which is the energy necessary to expel the electron from its core level. In order to relate $\chi(E)$ to structural parameters, we transform from (absolute) energy space into (relative) k-space:

$$k_{\mathrm{el}} = \sqrt{\frac{2m_e}{\hbar^2}\left(E - E_0\right)} \ , \tag{2.5}$$

which can be used to transform $\chi(E)$ into $\chi(k)$ (from now on, the wave vector subscript referring to the photoelectron is omitted). The latter is given by the EXAFS equation:

$$\chi(k) = \sum_j \frac{N_j f_j(k) e^{-2R_j/\lambda(k)} e^{-2k^2\sigma_j^2}}{kR_j^2} \sin[2kR_j + \delta_j(k)] \ , \tag{2.6}$$

where $f_j(k)$ is the scattering amplitude of the neighboring atom, j, and $\delta_j(k)$ is the phase shift. Both are photoelectron scattering properties of the atom and depend on the atomic number Z of the scattering atom. $\lambda(k)$ is the photoelectron mean free path representing inelastic scattering (*i.e.* the imaginary part of the electron's self-energy). While the properties, $f(k)$, $\delta(k)$ and $\lambda(k)$, can be calculated, we can determine by means of fitting: (i) half scattering distance R_j, which equals the distance to neighboring atoms in the case of SS pathways, (ii) the coordination number, N_j, of the neighboring atom or path degeneracy, and (iii) the σ_j^2 mean-square disorder of neighbor distances. Expansions of the EXAFS equation to include MS pathways can be found elsewhere.[118,120] Analysis of EXAFS can yield the numbers and types of atoms in the local (∼6 Å) environment of the absorbing atom and an accurate determination of absorber-neighbor bond distances.[118]

2.2.1 EXAFS data reduction

In this section we describe the steps for reducing raw data from a synchrotron experiment to normalized EXAFS data, $\chi(k)$. Because all data in this thesis was measured in fluorescence mode, we will cater our discussion to that and will not highlight procedures used for transmission mode XAS. We note that the data reduction procedures for XAS collected in transmission and fluorescence modes are similar.[119]

1. **Conversion of measured intensities to absorption.** X-ray absorption is determined from the measured fluorescence intensity, I_F, and the incoming X-ray intensity, I_0. The probability of fluorescence is proportional to the absorption probability : $\mu(E) \propto I_F/I_0$.

2. **Energy calibration.** The energy of the X-rays is calibrated using a standard foil. These foils are available at most synchrotron beam lines.[121] The user measures the XAS spectrum of a standard foil of the element of interest or, if not available, an element whose absorption edge is closest to the element of interest. The exact energy of the absorption edge, E_0, is determined typically as the energy of the maximum of the first derivative of $\mu(E)$. The difference between the measured E_0 and reference E_0 is used to calibrate the energy axis for the experiment of interest.[121] Energy calibration is important for reproducibility and comparability of samples measured at different synchrotrons and at different times. Moreover, it can be used for obtaining chemical information about the sample itself, since the absolute edge position is sensitive to the effective charge density of the absorbing atom. With proper energy calibration, we can therefore determine the oxidation state of a compound by comparing it to the spectra of known compounds.

3. **Subtraction of pre-edge background.** To get rid of any instrumental background and absorption from other edges, we subtract a smooth pre-edge function from $\mu(E)$.

4. **Normalization of data.** The edge jump, $\Delta\mu$, at the absorption edge is determined and $\mu(E)$ is normalized so that the pre-edge goes from approximately 0 below the threshold energy to 1 well above the threshold energy. This normalization procedure effectively converts the spectrum into the absorption spectrum of a single atom, removing contributions from variations in sample preparation, sample thickness, absorber concentration, detector and amplifier settings and so on, which is particularly important for the comparison of experimental data with theoretical spectra. An example of a normalized XAS spectrum is presented in Figure 2.8a.

5. **Subtraction of post-edge background.** A smooth post-edge background function is subtracted, which approximates $\mu_0(E)$. $\mu_0(E)$ represents the absorption coefficient from an absorbing atom without the presence of any neighboring atoms, which is a hypothetical spectrum. Instead, it is determined empirically by fitting a spline function to $\mu(E)$. A spline is a piece-polynomial function that is designed to be adjustable enough to smoothly approximate an arbitrary waveform, while maintaining convenient mathematical properties such as continuous first and second derivatives.[119] The removal of the post-edge background function thereby isolates the EXAFS oscillations: $\chi = (\mu - \mu_0)/\Delta\mu$. An example of a XAS spectrum converted to k-space is presented in Figure 2.8b.

6. **Conversion from energy to wavenumbers.** EXAFS is best understood in terms of the wave behavior of the photoelectron created in the absorption process, so we convert the X-ray energy to k, the wave number of the photoelectron. k has dimensions of 1/distance and is defined as in Equation 2.5. An example of an EXAFS spectrum converted to k-space is presented in Figure 2.8b.

7. **Fourier Transformation.** Using a Fourier transformation, the oscillations are converted to R-space, to yield the effective radial distribution function (RDF), which is the distribution of distances between the absorbing atom and surrounding atoms in a

sphere of $\backsim$6 Å, as shown in Figure 2.8c. We note that in R-space a phase correction is necessary to obtain the true radial distribution function of bond distances, which is primarily due to the atomic phase shift $\delta_j(k)$ in the argument of the sine function in Eq. 2.6.[122]

8. **Data Fitting.** The oscillations are fit to the model crystal structure for the material. Programs such as Larch[123] and the Demeter XAS[124] suite are commonly used for EXAFS data processing and fitting. We describe the specific fitting procedures used for the data obtained in this thesis in Chapter 3.

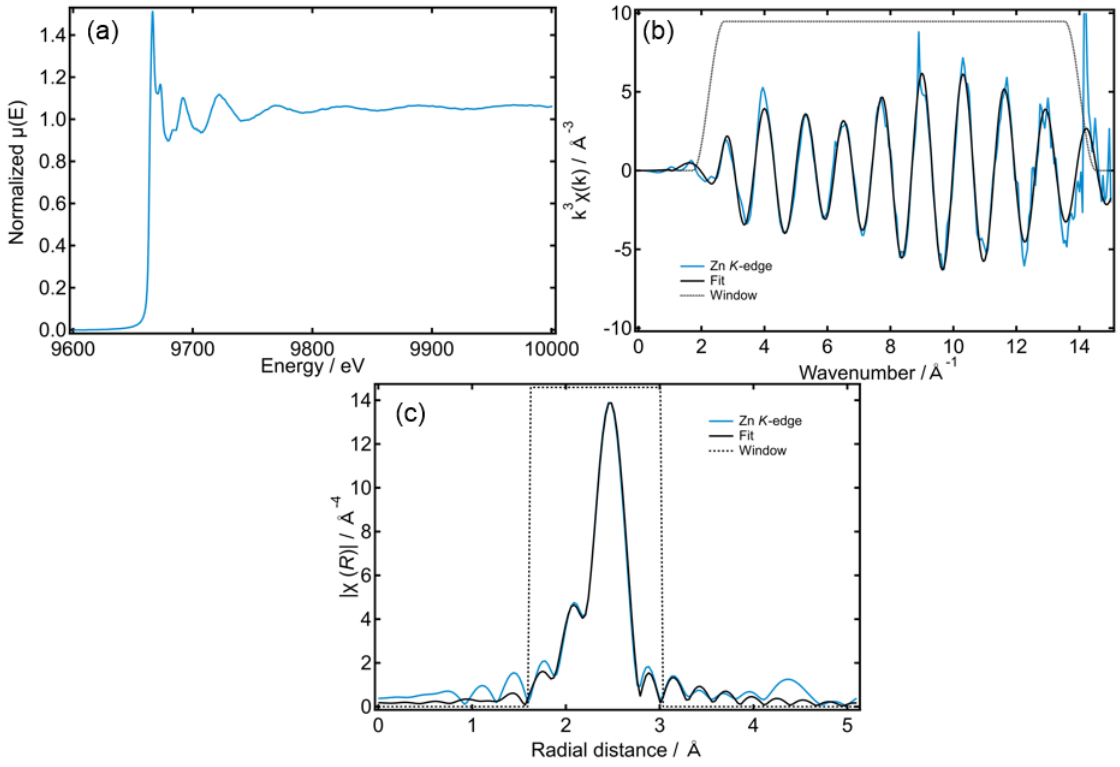

Figure 2.8: An example of XAS data presented in terms of energy, k-space and R-space. (a) An example Zn K-edge XAS spectrum of a $Zn_xCd_{1-x}Te/CdSe$ sample. (b) EXAFS data obtained after pre-edge and background subtraction, edge normalization, E-to-k space conversion and weighting by k^3. (c) The Fourier transform of the data presented in (b), which represents an effective and local radial distribution function of the absorbing atom. The abscissa is shifted with respect to the real distances in the material due to k-dependent parameters that affect the frequencies.

2.3 Theory of XANES spectroscopy

XANES is a powerful tool for probing the electronic and geometric structure around an absorbing atom due to the sensitivity of the near-edge region to the surroundings of the absorbing atom. The interpretation of XANES spectra has come a long way from the qualitative fingerprinting approach of comparing the data with the spectra of model compounds[125,126] to a quantitative or semi-quantitative probing tool to determine the structure of molecules in solution,[127–129] bulk solids,[130] or heterogeneous nanomaterials.[131]

As we have described in Section 2.1.3, XAS deals with the transition of a core electron to an upper empty bound or continuum state. Just like in the EXAFS region, the transition probability is given by Fermi's Golden Rule including the transition matrix element $\langle f|\hat{\varepsilon}\cdot\mathbf{r}|i\rangle$ with initial state $|i\rangle$ and the final state $|f\rangle$. While the initial core state, $|i\rangle$, is relatively straight-forward to calculate and while the transition operator can be well approximated in either the dipole or quadrupole approximations,[132] the calculation of the final states for the XANES region is challenging. The field of XAS has great interest in codes that are able to simulate XANES; however, the complex electronic many-body phenomena these codes seek to describe is a theoretical challenge.

Computational tools now allow us to quantitatively confirm or discard structural models. Such codes include FEFF-9[122,133,134] which is based on full multiple scattering (FMS) theory, discussed in more detail below. Several DFT-based codes also exist. DFT is one of the most popular and diverse quantum mechanical modeling methods in chemistry and materials science. DFT is used to determine the properties of a many-electron system by using functionals, in other words, functions of another function, which in this case is the spatially dependent electron density. In general, DFT is useful for understanding ground-state properties of bulk materials, such as atomic positions, atomic potentials, bond angles, and bond lengths. These ground state properties ultimately determine how the material behaves. Wien2k[135,136] makes use of periodic basis sets. Additionally, ORCA[137] and XSpectra[138] are

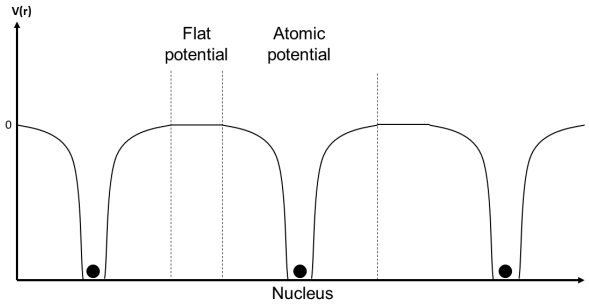

Figure 2.9: Schematic of the muffin-tin potential approximation. The potential is spherical around the atoms in the ground state. The interstitial potential region between the spheres is flat and set to zero.

codes with localized orbitals in a basis set that are able to directly compute the pre-edge region within the time-dependent DFT approximation (TDDFT). TDDFT can provide reasonable simulation for XANES up to 40 eV above the absorption edge. The FDMNES package implements a full-relativistic description in the monoelectronic approximation within the DFT-local density approximation (LDA).[132,139,140] FDMNES has the choices of the FMS method or finite difference method (FDM) for calculations, both of which we will discuss in more detail below. At energies greater than $\backsim$50 eV, in the EXAFS region, the photoelectron wave function can be approximated as the superposition of an outgoing spherical wave and a spherical wave back scattered by neighboring atoms. At lower energies, in the XANES region, the single scattering approximation no longer holds due to multiple scattering and many body effects. FMS is a common approach to calculate photoelectron wave function. An important approximation of FMS is that the potential is spherically symmetric around the atoms in a crystal and is constant in the surrounding region, the so-called muffin-tin approximation (Figure 2.9). The muffin-tin approximation is typically a valid approach in highly symmetric and dense systems, for example, copper metal. Often, the scattering in the interstitial area between atoms is taken into account via overlapping muffin-tin spheres. While this is only an approximation to the real, varying interstitial potential, the errors remains reasonable for overlap values of 10 to 15%.[133] When a system is dense, the inter-

stitial region is small and can be well-described by a constant potential. The choice of the muffin-tin radius and the value of the constant potential in the interstitial region are the key parameters in this approximation. In a lower symmetry system, the interstitial region is not easy to define. Thus in a sparse system with low symmetry, such as zinc blende chalcogenides of interest in this thesis, the the muffin-tin approximation does not hold well. We therefore sought a code with a higher level of theory than FMS for our simulations of the XANES spectra in II-VI transition metal chalcogenides.

The *ab initio* calculations of the XAS presented in this thesis have been performed with the FDMNES package developed by Yves Joly and coworkers.[132,139,140] FDMNES is an X-ray spectroscopy simulation code which has the option to use FMS or FDM to calculate the near-edge structure. FDM is another, albeit more computationally expensive, way to calculate the final states and avoids the muffin-tin approximation. Generally, FDM is a method to solve differential equations by creating a discrete grid of points in the whole volume of the calculation. FDM allows for a completely free potential shape and is thus an *ab initio* calculation.[132] We will next describe the steps of the calculation in FDMNES and then details on the implementation of the FDM method.

2.3.1 Calculation procedure

FDMNES is a real-space code which builds clusters around the absorbing atoms performing several independent calculations when there are several non-equivalent absorbing atoms. The minimum inputs needed to start a calculation are: (1) the energy range to calculate around the Fermi energy, (2) the radius of the cluster (number of atoms which are explicitly considered in the calculation) (3) the crystal or molecular structure: point group, unit cell dimension and angles, atomic positions in the unit cell, atomic numbers, and (4) the atom absorbing the X-ray radiation and the ionized core orbital (choice of the X-ray edge).

In the FDMNES code, the user first selects the absorbing atom and the size of the cluster around the absorbing atom. This cluster must be large enough to capture the back-

scattering from neighboring atoms which is dictated by the inelastic mean free path of a photoelectron with 0-40 eV kinetic energy.[132] FDMNES calculates the initial ground state of the absorbing atom in a self-consistent field (SCF) manner.[139] Briefly, SCF calculation means that electronic density from the first calculation is used to derive the potential for the next calculation. These steps are iterated until the difference between results is minimized. The user can define the difference tolerance. Convergence is considered achieved once the difference between iterations is sufficiently small. FDMNES assumes the absorbing atom has an excited electronic configuration with the core electron on the first unoccupied level available. To calculate the charge density of the real-space cluster, FDMNES creates a superposition of the atomic densities and solves the Poisson equation to get the Coulomb potential. FDMNES improves the potential by considering an energy-dependent exchange-correlation correction using LDA-DFT. With the potential constructed, FDMNES gets the final states by solving the Schrödinger-like equation using the FDM (*vide infra*). It then calculates the matrix elements of the absorption cross-section, and sums over the final states. Finally, the user can convolute the spectrum to account for core-hole life time broadening and energy-dependent inelastic scattering of the photoelectron.

FDMNES decomposes the calculation into three different regions, which are depicted in Figure 2.10, and is bound by an outer sphere where the potential is considered constant. The area of these zones is minimized by symmetry planes. The first zone is an outer zone of the calculation itself. This zone is defined as the overall scattering radius and defines where the wave functions are calculated. Consequentially, the outer radius of the calculation needs to extend until the back-scattered wave functions do not contribute to the scattering wave field of the absorbing atom, which is typically 5-8 Å. Outside the outer radius, the potential is assumed to be constant with spherical symmetry. The second zone is *inside* the outer radius where the FDM is used to calculate the potential between atomic cores. The third zone is inside the atomic cores themselves. In the atomic cores, the potential is calculated by the expansion of spherical waves in tiny spheres, much smaller than the spheres used in

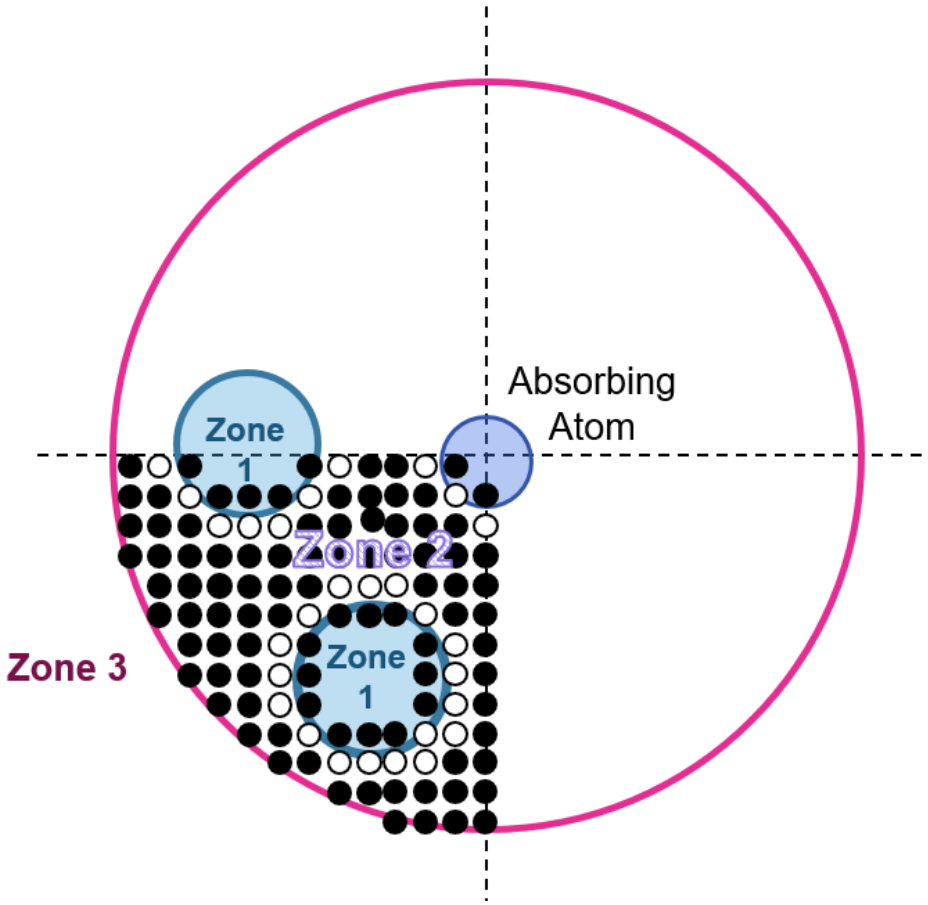

Figure 2.10: There are three main zones of calculations in FDMNES. The calculation is performed in real space. Zone 1 atomic cores: the potential is decomposed into spherical harmonics, and the FDM is not used (blue regions). Zone 2 interstitial region: the FDM calculation is performed in this region (pink region). Zone 3: outer sphere. The potential is kept constant (outside of pink region). The calculation is performed in the minimum size of this region, also known as the cluster sphere. The area of these zones is minimized by symmetry planes of the crystal space group.

the muffin-tin approximation. These inner atomic spheres are typically about 0.5-0.7 Å in radius.

Chapter 3

Methods

This chapter provides the experimental and theoretical methods of the work performed in this thesis. In Sections 3.1 and 3.2 we describe the synthetic procedures and materials characterization of the QDs of interest. Next, in Section 4.3 we present the equations used to build structural models of the nanoparticle based on the characterization data. In Section 3.4, we describe the methods for modeling cation diffusion. The methods used to calculate the band structure for the particle models follow in Section 3.5, and in Section 3.6 we describe the details of the density functional theory (DFT) calculations that are part of Chapter 5. Finally, the technical details of the static and ultrafast spectroscopy experiments are given in Section 3.7.

Acknowledgements The nanoparticle models, band structure, and heat equation calculations were performed by Yuanheng Wang, and the DFT calculations were done by Erick Hernandez Alvarez. The majority of the sample characterization was performed at the Materials Research Laboratory (MRL) Central Facilities at the University of Illinois at Urbana-Champaign (UIUC). Inductively coupled plasma-optical emission spectrophotometer (ICP-OES) measurements were carried out by the Microanalysis Laboratory in the School of Chemical Sciences at UIUC. In particular, we acknowledge Dr. Jim Mabon for assistance in S/TEM on the Themis Z, Dr. Rick Haasch for help with the XPS measurements, and Frank Alcorn for high resolution imaging on Hitachi TEM. We gratefully acknowledge Insung Han and Prof. Shoemaker for measuring the X-ray Diffraction (XRD) pattern. This research used resources of the Advanced Photon Source (APS), a U.S. Department of Energy (DOE) Office of Science User Facility operated for the DOE Office of Science by Argonne National

Laboratory (ANL) under Contract No. DE-AC02-06CH11357. We thank Dr. Gilles Doumy, Dr. Anne Marie March, Dr. Don Walko, Dr. Andre Al Haddad, and Dr. Ming-Feng Tu, Dr. George Sterbinsky, Dr. Tianpin Wu, and Dr. Steve Heald for assistance during measurements at the APS. We also thank the members of the van der Veen lab for their assistance during all the beam times: Dr. Renske van der Veen, Conner Dysktra, Tyler Haddock, Ryan Cornelius, Rachel Wallick, Allan Sykes, Thomas Dixon, and Yuanheng Wang. We thank Dr. Thomas Rossi, Dr. Michael Enright, and Dr. Leslie Hamachi for fruitful discussion.

3.1 Synthetic methods

In this work, we followed the protocol for the synthesis of ZnTe/CdSe core/shell quantum dots (CSQDs), which was published in 2005 by Xie *et al.*[36] The protocol makes use of successive ion layer adsorption and reaction (SILAR) for shell growth. SILAR was developed in the mid-1980s for deposition of thin films.[141] For thin films, one SILAR cycle consists of the substrate being immersed into two precursor solutions, and washed in between to remove excess precursor, followed by room temperature reaction.[141] However, in the variation of SILAR used most commonly in the production of CSQDs,[10,142] including that used by Xie *et al.*,[36] the solution is not washed between the injection of precursor solutions, and the reaction occurs at elevated temeratures (240 ℃). Both of these conditions make this synthesis more susceptible to ion diffusion, which results in the possibility of a gradient interface or a new intermediate layer between the core and the shell.[143] On the other hand, this one-pot type synthesis reduces of the number of purification steps, which is advantageous for potential use in scaled up industrial processes. The ZnTe cores are very air sensitive, which renders a one-pot synthesis less susceptible to oxidation.

We begin this section with the necessary chemicals and the procedure for the preparation of the precursors. We then cover the synthetic procedures for the CSQDs, CdTe QDs, and CdSe QDs. Finally, we describe the conditions of the anion exchange control experiment.

3.1.1 Chemicals and precursors

Tellurium powder (99.8%, 200 mesh), cadmium oxide (CdO, 99.5%), selenium powder (99.5%, 100 mesh), oleic acid (OA, 90 %), 1-octadecene (ODE, 90 %), trioctylphosphine (TOP, 90 %), hexadecylamine (HDA, 90%), diethylzinc ($ZnEt_2$, 1.0 M in hexanes), toluene (ACS reagent, 99.5%) were purchased from Millipore Sigma.

The 0.1 M cadmium precursor solution used for the CdSe shell growth was prepared by dissolving 0.1602 g of CdO in a mixture of 3.09 g of oleic acid and 9 mL of ODE at 240 °C under nitrogen atmosphere. The 0.1 M selenium precursor solution was prepared by dissolving 0.1580 g of Se in 5 mL of TOP and 15 mL of ODE in a glove box. TOP-Te was prepared by dissolving 0.638 g of Te in 20 mL of TOP at about 80 °C for 1 h in a glove box.

3.1.2 Synthesis of core/shell nanoparticles

CSQDs were synthesized via the one-pot SILAR method[36] which is summarized in Figure 3.1. Four QD samples were prepared using this method: SILAR 0.5, SILAR 1, SILAR 2 and SILAR 3. First, the 2.5 nm diameter ZnTe cores were grown by quickly injecting a solution of 0.50 mmol of Te and 0.50 mmol of $Zn(Et)_2$ in 2 mL of trioctylphosphine into the reaction flask containing 3 g of hexadecylamine and 4 g of 1-octadecene at 300 °C and under a nitrogen atmosphere. Following injection, the reaction temperature was set to 270 °C to allow nanoparticles to grow for 3 min. The ZnTe core solution was then cooled to 240 °C and exposed to successive injections of Cd and Se precursor solutions. The SILAR 0.5 sample was prepared by adding 2.3 mL of a 0.1 M Cd-oleate solution dropwise to the ZnTe core solution, letting it react for 10 min, and quenching the reaction by removing the reaction flask from the heat and cooling the flask quickly with compressed air. No Se was added for this sample. In the case of the SILAR 1 sample, after 10 min of reaction with the Cd-oleate precursor, the same amount of Se precursor solution (0.1 M Se in TOP and ODE) was also added dropwise. After another 10 min the reaction was quenched by removing the

reaction flask from the heat and cooling the flask quickly with compressed air. Subsequent shell growth was done by repeating these SILAR cycles with 10 min reaction time in between additions and increasing amounts of precursor to account for particle growth (2.9 mL for SILAR 2, 3.6 mL for SILAR 3). After quenching, the nanocrystals were washed 3 times in toluene/acetone and suspended in 20 mL of toluene.

3.1.3 Synthesis of CdSe QDs

CdSe QDs (3.4 ± 0.3 nm) were prepared by a common hot-injection approach as described by Yang *et al.*[144] The reaction flask was prepared by loading 60 mg of CdO, 2 g of oleic acid, and 14 mL of ODE into a three-neck flask under argon flow, and stirred at 255 °C until CdO was completely dissolved. The selenium precursor was prepared in a glove box by dissolving 160 mg of Se powder in 2 mL of TOP and loaded into a syringe. The TOP-Se solution was then injected into the Cd precursor solution with rapid stirring, and kept at 255 °C for 8 min, followed by cooling down to room temperature. The product was then washed with acetone and re-dispersed in 20 mL of toluene.

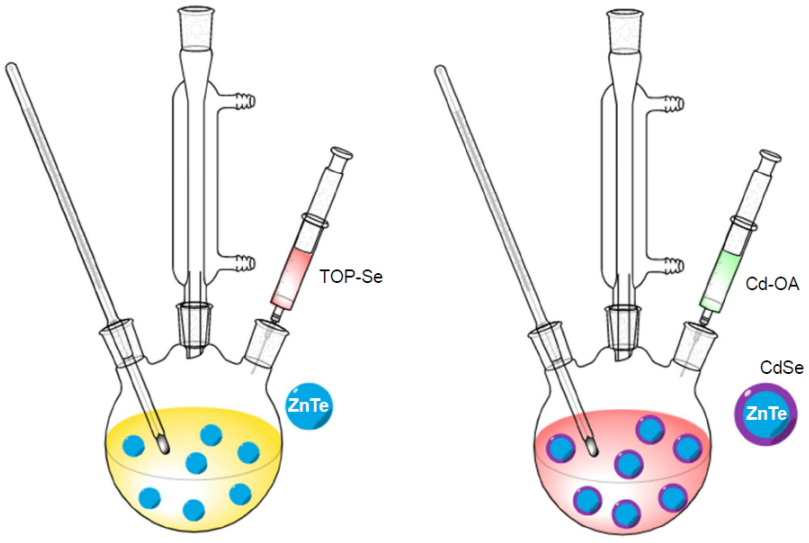

Figure 3.1: SILAR synthesis schematic for the ZnTe/CdSe sore/shell quantum dots. The two steps of the SILAR synthesis are highlighted. On the left is the injection of TOP-Se precursor into the reaction vessel containing ZnTe cores is shown. On the right the injection of Cd-OA is shown. The intention of these SILAR steps is to create a complete CdSe shell surrounding the cores.

3.1.4 Synthesis of CdTe QDs

CdTe QDs (6.3 ± 0.5 nm) were prepared by the common hot-injection procedure of Dorfs *et al.*[145] The Cd-tetradecylphosphonic acid (TDPA) precursor was prepared by degassing 0.24 g TDPA under nitrogen flow for 1 h at 100 °C, followed by dissolving 0.033 g CdO under a nitrogen atmosphere between 250 and 300 °C until the mixture became clear. TOP-Te was prepared by dissolving 0.19 g of Te in 10 mL of TOP at about 80 °C for 1 h under a nitrogen atmosphere. The Cd-TDPA precursor, 0.22 g of HDA, and 7.8 mL of ODE were degassed under a nitrogen flow for 1 h at 100 °C. The temperature was then raised to 280 °C, and 2 mL of the TOP-Te precursor is subsequently injected. After the injection, the temperature of the mixture is reduced and maintained at 260 °C for the growth of nanocrystals. The reaction was stopped by temperature quenching with a water bath. The product obtained was purified using toluene as the solvent and an isopropanol/methanol mixture as the nonsolvent. The final purified product was suspended in 10 mL of toluene.

3.1.5 Anion exchange control experiment

We synthesized and purified CdTe quantum dots as described in Section 3.1.4 using the method by Dorfs *et al.*[145] and resuspended in 5 mL of degassed ODE in the glove box. 0.1 M TOP-Se was prepared in the glove box by dissolving 0.158 g of Se powder in 5 mL of TOP and 15 mL of degassed ODE. 7 mL of the 0.1 M TOP-Se was degassed under vacuum in a flask on the Schlenk line at 100 °C for 1 hour. The TOP-Se was heated to 270 °C under N_2 atmosphere. 5 mL of the CdTe quantum dots in ODE were injected, and the mixture was held at 240 °C for 40 mins. The reaction was quenched by removing from heat and cooling the reaction flask with compressed air. The mixture was washed by centrifugation with toluene/IPA. ICP-OES of the resulting mixture contained a molar ratio of 1:0.53:0.03 Cd:Te:Se, indicating no significant amount of anion exchange.

3.2 Materials characterization methods

Several modes of standard techniques were used to characterize the CSQDs. In this section we describe the instrumental details and experimental procedures for each technique. These techniques provide information pertinent to the optical properties, crystallinity, elemental compositions, and nanoparticle size of the CSQDs. The information obtained from these characterization techniques was used to build the nanoparticle models described in the next section. Results and discussion of the materials characterization are covered in Chapter 4.

Ultraviolet/visible (UV/vis) absorption spectroscopy was performed using a Varian CARY 5G spectrophotometer. Samples were typically diluted by a factor of 100 in toluene. Photoluminescence (PL) quantum yields were determined using an integrating sphere. PL spectra were collected with a Horiba Jobin Yvon FluoroMax-3 fluorometer (excitation wavelength: 532 nm), and decay curves were obtained by time-correlated single-photon counting (excitation wavelength: 532 nm, 120 ps pulse width, 3.13 MHz repetition rate, 200 μJ/cm^2). Powder XRD patterns were obtained by a Bruker D8 ADVANCE diffractometer with a Mo-Kα radiation source and a LYNXEYE XE detector. Samples were evaluated for Zn, Te, Cd, and Se composition using a Perkin Elmer Optima 8300 ICP-OES.

Transmission Electron Microscope (TEM) measurements were performed using a JEOL 2100 Cryo TEM operating at 200 kV acceleration voltage. The samples for electron microscopy were prepared by drop casting a suspension (typically 10 μL of 100x diluted as-synthesized sample) on a holey carbon film supported by a copper TEM grid. TEM grids with ZnTe QDs were prepared inside a glove box and transferred inside the TEM as rapidly as possible (1 min). On the basis of the TEM images, size histograms, mean diameters, and size dispersions of the QDs are determined by analyzing 100-200 particles for each sample using the Image J program. The diameter for each nanoparticle was calculated from the measured area. High annular dark-field (HAADF) scanning TEM (STEM) and high-resolution TEM (HRTEM) images were taken using a FEI Themis Z advanced probe aberration corrected

analytical TEM/STEM.

X-ray photoelectron spectroscopy (XPS) was measured on four samples: SILAR 0.5 SILAR 1, SILAR 2, and SILAR 3. XPS measurements were performed on a Kratos Axis Ultra spectrometer, using a monochromatized Al Kα source. Wide survey scans and high-resolution narrow scans were performed. The binding energy (BE) scale was internally referenced to the C 1s peak (BE for C–C = 285.0 eV). The data were converted to VAMAS format, processed, and fit using CasaXPS software, version 2.3.22PR1.0.

3.3 Nanoparticle structure models

We used results from TEM and ICP-OES to construct nanoparticle models for the four CSQD samples (SILAR 0.5, SILAR 1, SILAR 2, SILAR 3). For simplicity, a perfect spherical model was considered. Another assumption was that the material in each layer will adopt a perfect crystal structure, neglecting the possible distortions from lattice mismatch or defects. The results and discussion of the structure models are covered in Chapter 4.

3.3.1 Model I: ZnTe/CdTe/CdSe core/interlayer/shell QDs

In this model, sharp interfaces between layers were assumed, that is, no alloying was taken into account. The number of atoms, n, of each element in the particle regions (core, shell) were calculated as:

$$
\begin{aligned}
n_{\mathrm{Zn}} &= 4 \times \frac{V_{\mathrm{ZnTe}}}{V_{\mathrm{ZnTe\ unit\ cell}}} = 4 \times \frac{\frac{4}{3}\pi R_1^3}{a_{\mathrm{ZnTe}}^3} \\
n_{\mathrm{Te}} &= 4 \times \frac{V_{\mathrm{ZnTe}}}{V_{\mathrm{ZnTe\ unit\ cell}}} + 4 \times \frac{V_{\mathrm{CdTe}}}{V_{\mathrm{CdTe\ unit\ cell}}} = 4 \times \left(\frac{\frac{4}{3}\pi R_1^2}{a_{\mathrm{ZnTe}}^3} + \frac{\frac{4}{3}\pi \left(R_2^2 - R_1^2\right)}{a_{\mathrm{CdTe}}^3} \right) \\
n_{\mathrm{Cd}} &= 4 \times \frac{V_{\mathrm{CdTe}}}{V_{\mathrm{CdTe\ unit\ cell}}} + 4 \times \frac{V_{\mathrm{CdSe}}}{V_{\mathrm{CdSe\ unit\ coll}}} = 4 \times \left(\frac{\frac{4}{3}\pi \left(R_2^3 - R_1^3\right)}{a_{\mathrm{CdTe}}^3} + \frac{\frac{4}{3}\pi \left(R_3^3 - R_2^3\right)}{a_{\mathrm{CdSe}}^3} \right) \\
n_{\mathrm{Se}} &= 4 \times \frac{V_{\mathrm{CdSe}}}{V_{\mathrm{CdSe\ unit\ cell}}} = 4 \times \frac{\frac{4}{3}\pi \left(R_3^3 - R_2^3\right)}{a_{\mathrm{CdSe}}^3} \ ,
\end{aligned}
\tag{3.1}
$$

where V_X is the total volume of material, X, in the QD, and R_1, R_2 and R_3 represent the radii of the core, interlayer and shell. Since R_3 is also the overall size of the QD, it was determined from TEM image analysis. a_X is the bulk lattice parameter of material X.[146] By varying $R_1$and R_2, the ratio between numbers of atoms for different elements ($n_{\mathrm{Zn}}/n_{\mathrm{Te}}$, $n_{\mathrm{Zn}}/n_{\mathrm{Cd}}$, *etc.*) was adjusted to best match the molar ratios from elemental analysis.

3.3.2 Model II: $Cd_xZn_{1-x}Te$/CdSe alloyed CSQDs

In this model, the core is assumed be a homogeneous alloy of ZnTe and CdTe, $\mathrm{Cd}_x\mathrm{Zn}_{1-x}\mathrm{Te}$. The number of atoms, n, of each element in the particle regions (core, shell) were calculated as:

$$\begin{aligned}
n_{\mathrm{Zn}} &= 4 \times \frac{\frac{4}{3}\pi R_{\mathrm{core}}^3}{\left(a_{\mathrm{ZnTe}_x} + a_{\mathrm{ZnTe}_{1-x}}\right)^3} \\
n_{\mathrm{Te}} &= 4 \times \frac{\frac{4}{3}\pi R_{\mathrm{core}}^3}{\left(a_{\mathrm{CdTe}_x} + a_{\mathrm{ZnTe}_{1-x}}\right)^3} \\
n_{\mathrm{Cd}} &= 4(1-x) \times \frac{\frac{4}{3}\pi R_{\mathrm{core}}^3}{\left(a_{\mathrm{CdTe}_x} + a_{\mathrm{ZnTe}_{1-x}}\right)^3} + 4 \times \frac{\frac{4}{3}\pi \left(R_{\mathrm{shell}}^3 - R_{\mathrm{core}}^3\right)}{a_{\mathrm{CdSe}}^3} \\
n_{\mathrm{Se}} &= 4 \times \frac{\frac{4}{3}\pi \left(R_{\mathrm{shell}}^3 - R_{\mathrm{core}}^3\right)}{a_{\mathrm{CdSe}}^3} \ .
\end{aligned} \tag{3.2}$$

All variables are defined the same way as in the previous model, except there is no R_2, and $R_1 = R_{\mathrm{core}}$ and $R_3 = R_{\mathrm{shell}} = R_{\mathrm{TEM}}$. The lattice parameter of the $\mathrm{Cd}_x\mathrm{Zn}_{1-x}\mathrm{Te}$ alloyed core is assumed to follow Vegard's law.[147] By varying $R_1 = R_{\mathrm{core}}$ and x, the ratio between numbers of atoms for different elements was adjusted to best match the molar ratios from elemental analysis.

3.3.3 Model III: Linearly-varying ZnTe + CdTe/CdTeSe CSQDs

In this model, Zn-Te bonds are assumed to occur over the whole quantum dot due to cation diffusion. The mole fraction of ZnTe is assumed to be a linear function of radius, that is $x_{\mathrm{Zn}}(r) = x_0 \frac{R_{\mathrm{shell}} - r}{R_{\mathrm{shell}}}$. The ZnTe concentration at the center of the QD (x_0) is a fitting variable.

The ZnTe concentration at the surface of QD ($x_{\mathrm{ZnTe}}(R_{\mathrm{shell}})$) is taken to be zero, since all zinc cations which have reached the surface will diffuse further into the solvent. The anions are assumed not to diffuse,[148] so Se will not enter the core, but an alloy of $CdTe_{1-x}Se_x$ can form in the shell.

The Figure 3.2 below illustrates the model.

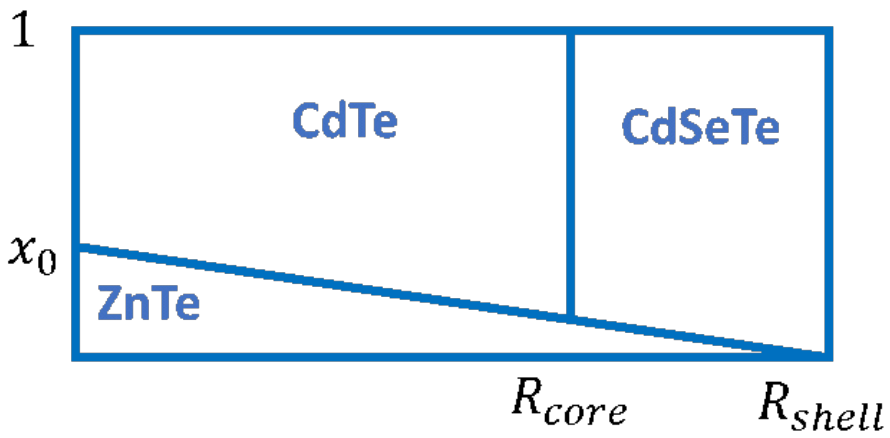

Figure 3.2: The material composition of QD at varying radius. The y-axis is the mole fraction.

The number of atoms, n, of each element in the particle regions (core, shell) were calculated as:

$$
\begin{aligned}
n_{\mathrm{Zn}} &= \int_0^{R_{\mathrm{core}}} \frac{4\pi r^2 dr \cdot 4x_{\mathrm{Zn}}(r)}{\left(a_{\mathrm{CdTe}}x_{\mathrm{Zn}}(r) + a_{\mathrm{CdTe}}\left(1 - x_{\mathrm{Zn}}(r)\right)\right)^3} + \\
&\int_{R_{\mathrm{core}}}^{R_{\mathrm{shell}}} \frac{4\pi r^2 dr \cdot 4x_{\mathrm{Zn}}(r)}{\left(a_{\mathrm{ZnTe}}x_{\mathrm{Zn}}(r) + a_{\mathrm{CdTe}}\left(1 - x_{\mathrm{Zn}}(r)\right)\left(1 - x_{\mathrm{Se}}\right) + a_{\mathrm{CdSe}}\ \left(1 - x_{\mathrm{Zn}}(r)\right)x_{\mathrm{Se}}\right)^2} \\
n_{\mathrm{Se}} &= \int_{R_{\mathrm{core}}}^{R_{\mathrm{shell}}} \frac{4\pi r^2 dr \cdot 4\left(1 - x_{\mathrm{Zn}}(r)\right)x_{\mathrm{Se}}}{\left(a_{\mathrm{ZnTe}}x_{\mathrm{Zn}}(r) + a_{\mathrm{CdTe}}\left(1 - x_{\mathrm{Zn}}(r)\right)\left(1 - x_{\mathrm{Se}}\right) + a_{\mathrm{CdSe}}\left(1 - x_{\mathrm{Zn}}(r)\right)x_{\mathrm{Se}}\right)^2} \\
n_{\mathrm{Cd}} &= \int_0^{R_{\mathrm{core}}} \frac{4\pi r^2 dr \cdot 4\left(1 - x_{\mathrm{Zn}}(r)\right)}{\left(a_{\mathrm{ZnTe}}x_{\mathrm{Zn}}(r) + a_{\mathrm{CdTe}}\left(1 - x_{\mathrm{Zn}}(r)\right)\right)^3} + \\
&\int_{R_{\mathrm{core}}}^{R_{\mathrm{shell}}} \frac{4\pi r^2 dr \cdot 4\left(1 - x_{\mathrm{Zn}}(r)\right)}{\left(a_{\mathrm{ZnTe}}x_{\mathrm{Zn}}(r) + a_{\mathrm{CdTe}}\left(1 - x_{\mathrm{Zn}}(r)\right)\left(1 - x_{\mathrm{Se}}\right) + a_{\mathrm{CdSe}}\left(1 - x_{\mathrm{Zn}}(r)\right)x_{\mathrm{Se}}\right)^2} \\
n_{\mathrm{Te}} &= \int_0^{R_{\mathrm{core}}} \frac{4\pi r^2 dr \cdot 4}{\left(a_{\mathrm{ZnTe}}x_{\mathrm{Zn}}(r) + a_{\mathrm{CdTe}}\left(1 - x_{\mathrm{Zn}}(r)\right)\right)^3} + \\
&\int_{R_{\mathrm{core}}}^{R_{\mathrm{shell}}} \frac{4\pi r^2 dr \cdot 4\left(\left(1 - x_{zn}(r)\right)\left(1 - x_{\mathrm{Se}}\right) + x_{\mathrm{Zn}}(r)\right)}{\left(a_{\mathrm{ZnTe}}x_{\mathrm{Zn}}(r) + a_{\mathrm{CdTe}}\left(1 - x_{\mathrm{Zn}}(r)\right)\left(1 - x_{\mathrm{Se}}\right) + a_{\mathrm{CdSe}}\left(1 - x_{\mathrm{Zn}}(r)\right)x_{\mathrm{Se}}\right)^3}\ .
\end{aligned}
\tag{3.3}
$$

The x_0 in $x_{\mathrm{Zn}}(r)$ and R_{core} are fitting variables, and the Se ratio in the shell x_{Se} is a fixed variable. $x_{\mathrm{Se}} = 1$ corresponds to no CdSe and CdTe mixing. Vegard's law is assumed for all alloys, but since the amount of ZnSe is very little, it is ignored. By varying R_{core} and x_0, the ratio between numbers of atoms for different elements was adjusted to best match the molar ratios from elemental analysis. The integrals are performed using MATLAB numerical integral functions.

3.3.4 Error propagation using the Monte Carlo method

The error propagation for fitting the radii of the above models was done using a Monte Carlo method, which involves a nonlinear minimization procedure. There are 5 experimental values involved in all fittings: the elemental ratio of 4 elements and the TEM particle radius (the lattice constants from the literature are assumed to be exact). Each of them has a corresponding standard deviation value for experimental error, and the error is assumed to be Gaussian. 10,000 sample points were generated using Matlab, each of which has random Gaussian errors for the 5 experimental values. For each value (ratio or radius), the standard deviation of the Gaussian error distribution is the same as the standard deviation of the experimental error. The core radius (R_{core}), interlayer radius (R_2) or the ZnTe/CdTe ratio in core (x), for all the sample points, are determined using the same procedure (refers to the radius calculation). The standard deviation of the result of all sample points is taken as the propagated error.

3.4 Cation diffusion simulations

Cation diffusion calculations were done using the theory described in Jiang, *et al.*[38] where the authors experimentally measured the cation diffusion rate to be 1.3x10^2 nm^2/min. Diffusion is described by a continuum, radially symmetric diffusion equation:

$$\frac{\mathrm{d}C(r,t)}{\mathrm{d}t} = D\nabla^2 C(r,t) = D\frac{1}{r^2}\frac{\mathrm{d}}{\mathrm{d}r}\left(r^2\frac{\mathrm{d}C(r,t)}{\mathrm{d}r}\right) , \tag{3.4}$$

where $C(r,t)$ is the composition profile for a certain radius r at time, t, and D is the interdiffusion constant. We use the MATLAB partial differential equation (PDE) solver, *pdepe*,[149] as shown in the code shown below. We assume that Zn^{2+} ions will immediately diffuse out of the particle into solution once they reach the surface.

Listing 3.1: MATLAB code used for cation diffusion calculations. The variable R_C is the radius of the core, determind by the model from Section 3.3, and R_S is the radius of the whole particle, determined by TEM sizing. The code below uses the values for SILAR 2 as an example.

```
function a()
D=1.3*10^-2;%Interdiffusion constant (nm^2/min)
R_C=1.46; R_S=2.9;%nm
x=[0:0.005:R_S];%nm
t=[0:10:40];%min
function [c,f,s]=pdex1pde(x,t,u,dudx)%c*d(u)/dt=x^-m*d(x^m*f)/dx+s
    c =1/D;
    f=dudx;
    s=0;
end
function u0=pdex1ic(x)
    u0=(sign(x - R_C) -1)/-2;
end
function [pl,ql,pr,qr]=pdex1bc(xl,ul,xr,ur,t) % p + q * f = 0
    pl=0; ql=1; %Boundary at the center.
    pr=ur; qr=0;
end
sol=pdepe(2,@pdex1pde,@pdex1ic,@pdex1bc,x,t);
u=sol(:,:,1);
end
```

3.5 Band structure simulation

A wavefunction engineering method, proposed by Şahin *et al.*,[150] was applied to determine the band properties of the CSQDs. In this method, an effective mass approximation was made to simplify the atomic-scale variation of potentials. The hole and electron were assumed to move freely in averaged valence-band and conduction-band potentials respectively, with certain effective masses (see Table S3 below). As a result, both charge carriers can be treated by a simple particle-in-a-sphere model. The Schrödinger equations of both particles were solved using the finite difference method (FDM). A mean field approximation was applied to account for the Coulomb interaction between electron and hole (exciton binding energy), meaning that the electron moves in a mean potential induced by the hole Φ_h and the hole moves in a mean potential of the electron Φ_e. These potentials cannot be determined beforehand but can be calculated by Poisson equations if the electron and hole wavefunctions were known. As a result, a self-consistent computation of wavefunctions and band energies was applied. Results and discussion of the wavefunction engineering method for band structure simulation are covered in Chapter 4.

3.5.1 Schrödinger equation

The carriers' Schrödinger equations are:

$$\begin{aligned}\left[-\frac{\hbar^2}{2}\nabla\cdot\frac{1}{m_h^*(r)}\nabla - e\Phi_e(r) + \frac{l(l+1)\hbar^2}{2m_h^*(r)r^2} + V_h(r)\right] R_h^{nl}(r) = E_h^{nl} R_h^{nl}(r) \\ \left[-\frac{\hbar^2}{2}\nabla\cdot\frac{1}{m_e^*(r)}\nabla - e\Phi_h(r) + \frac{l(l+1)\hbar^2}{2m_e^*(r)r^2} + V_e(r)\right] R_e^{nl}(r) = E_e^{nl} R_e^{nl}(r)\ ,\end{aligned} \tag{3.5}$$

where $R^{nl}(r)$ is the radial wavefunction for electron or hole. Only the radial wavefunction is considered due to the symmetry. $m^*(r)$ is the effective mass, and $V(r)$ is the confinement potential for both particles. For zinc blende structure crystals, the highest energy valence band states are made up of two degenerate states, described by light hole and heavy hole in the effective mass approximation. The heavy hole is the dominating one because of its larger density of states. Inside each layer, these properties are assumed to be constant and identical to the corresponding bulk values, as shown in Table 3.1.

Table 3.1: The constants used for bandgap calculation, including the confinement potentials, effective masses, and dielectric constants of ZnTe, CdTe, CdSe and toluene. The parameters for semiconductors all come from bulk values.[146]

	ZnTe	CdTe	CdSe	Toluene
Description	Core	Interlayer	Shell	Solvent
Radius range (nm)	0-1.46	1.46-2.76	2.76-2.95	2.95-2.95 × 3
Effective heavy hole mass	0.810[a]	0.982[a]	1.217[a]	1
Effective electron mass	0.151[a]	0.098[a]	0.116[a]	1
Valence band potential (V)	0[b]	-0.13[b]	-0.70[b]	-6.726[152] + 5.64[36]
Conduction band potential (V)	2.26[b]	1.31[b]	1.04[b]	-0.261[152] + 5.64[36]
Dielectric constant (ε_0)	6.9[153]	7.1[153]	6.2[153]	1.375[c]

[a] The theoretical result using GGA as the exchange–correlation functional.[151]

[b] The valence band potential of ZnTe is set to zero, and all other potentials are shifted respectively.[36]

[c] The infinite-frequency dielectric constant of hexane,[12] used to estimate the dielectric constant of toluene.

3.5.2 Poisson equation

After determination of the radial wavefunction, the electron and hole potentials are calculated based on the Poisson equation:

$$\begin{aligned} \nabla \cdot \varepsilon(r)\varepsilon_0 \nabla \Phi_h(r) &= -e\rho_h(r) \\ \nabla \cdot \varepsilon(r)\varepsilon_0 \nabla \Phi_e(r) &= e\rho_e(r) \ , \end{aligned} \tag{3.6}$$

where ε is the infinite-frequency dielectric constant (relative to vacuum permittivity ε_0), and ρ_e and ρ_h are the electron and hole density, respectively. For a single exciton, the densities are related to the radius wavefunctions by:

$$\begin{aligned} \rho_h(r) &= \frac{1}{4\pi} \left| R_h^{nl}(r) \right|^2 \\ \rho_e(r) &= \frac{1}{4\pi} \left| R_e^{nl}(r) \right|^2 \ , \end{aligned} \tag{3.7}$$

where the $1/4\pi$ is a normalization term, which accounts for the difference ways of normalization for ρ and R.

The electron and hole potentials far outside the QD ($r > 3R_{\text{out}}$) are derived from Gauss' law for D-field, with the assumption that solvent molecules fill up all the outside space:

$$\begin{aligned} \Phi_h\left(3R_{\text{out}}\right) &= \tfrac{1}{4\pi\overline{\varepsilon_{\text{QD}}}\varepsilon_0} \tfrac{e}{3R_{\text{out}}} \\ \Phi_e\left(3R_{\text{out}}\right) &= -\tfrac{1}{4\pi\overline{\varepsilon_{\text{QD}}}\varepsilon_0} \tfrac{e}{3R_{\text{out}}} \end{aligned} \tag{3.8}$$

where $\overline{\varepsilon_{\text{QD}}}$ is the average dielectric constant of the QD.

The derivative of the electron and hole potentials at the boundary are set to be continuous with the potential outside the considered region:

$$\left.\frac{d\Phi_n}{dr}\right|_{r=3R_{\text{out}}} = -\frac{1}{4\pi\overline{\varepsilon_{\text{QD}}}\varepsilon_0} \frac{e}{\left(3R_{\text{out}}\right)^2} \ , \tag{3.9}$$

ε and Φ are projected to the same finite difference grid as described in section 3.5.1. The finite difference Poisson equations are solved using a least square method.

3.5.3 Self-consistent computation of band structure

The self-consistent computation procedure is implemented in the following way. The Schrödinger equations for the electron and hole are solved separately in the first round, neglecting the interaction, and the non-interactive electron and hole energies (E_e^{nl-0} and E_h^{nl-0}) are determined. The non-interactive wavefunctions are applied to the Poisson equation to find the potential caused by electron and hole, and the potential is inserted into the Schrödinger equation for the second cycle. The scheme for the self-consistent cycle is Schrödinger equation $\rightarrow R_h,\ R_e \rightarrow$ Possion equation $\rightarrow \Phi_h$, $\Phi_e \rightarrow$ Schrödinger equation $\rightarrow \ldots$

The loop reaches convergence if the eigen energy derived from the Schrödinger equation is similar in successive rounds for both particles:

$$\begin{aligned} \left| E_h^{nl-kth \text{ cycle}} - E_h^{nl-(k+1) \text{ th cycle}} \right| &< 0.01 \text{ eV} \\ \left| E_e^{nl-kth \text{ cycle}} - E_e^{nl-(k+1) \text{ th cycle}} \right| &< 0.01 \text{ eV} . \end{aligned} \tag{3.10}$$

Since the electron-hole Coulomb interaction is counted twice (the electron was considered feeling the hole potential, and the hole was considered feeling the electron potential as well), half of the calculated attraction energy is subtracted to give the exciton binding energy:

$$E_{\text{exciton}}^{nl} = E_e^{\text{nl-last}} - E_h^{\text{nl-last}} - \frac{\left(E_e^{nl-0} - E_e^{nl-\text{last}}\right) + \left(E_h^{nl-\text{last}} - E_h^{nl-0}\right)}{2} \tag{3.11}$$

$$P(r) = 4\pi r^2 \left(R^{nl}(r)\right)^2 \tag{3.12}$$

The wavefunction overlap between two energy states is calculated as:

$$P_{12}(r) = 4\pi r^2 R_1^{nl}(r) R_2^{nl}(r) . \tag{3.13}$$

The overlap between $1S_h$ and $1S_e$ states is taken as an estimation of band alignment.

3.6 Density functional theory methods

In this section, we present the DFT methods performed by Erick Hernandez Alvarez in collaboration with Professor Andre Schleife. Because the experimental results presented in Chapter 4 provide evidence of cation alloying in the particle core (and the absence of anion alloying), we employed DFT to relax a supercell of a representative $Cd_xZn_{1-x}Te$ (x=0.8) alloy. The supercell is then used as an input structure in FDMNES, an X-ray spectroscopy simulation code described in Chapter 3. The results and discussion of the DFT methods for simulation of the XANES spectra are discussed in Chapter 5.

The Vienna Ab Initio Simulation Package (VASP) was used for DFT calculations.[154] Calculations using three types of exchange-correlation approximations/functionals are used: the local density approximation (LDA), the Perdew-Burke-Ernzerhof-type generalized gradient approximation (PBE-GGA), and the HSE06 hybrid functional.[155,156] Electron-ion interactions are modeled using the projected augmented wave (PAW) method.[157] Electronic wave functions are expanded in plane-wave basis sets with an energy cutoff of 450 eV. The Brillouin zone is sampled by 6x6x6 and 2x2x2 Gamma-centered k points in the PBE and HSE06 approach respectively. CdTe and ZnTe HSE06 calculations are performed with a 6x6x6 Gamma-centered k-point grid and a conventional unit cell.

For alloyed cells the initial supercell geometry for zinc blende cells containing 20 atoms is determined using the atomic simulation environment software package tools for constructing optimal supercells.[158,159] Alloy supercells are then determined using a cluster expansion method.[160] For the 20% Zn supercells, the equilibrium cell volumes and total energies are obtained by minimizing total energy for multiple cell volumes and fitting the volume dependence of the total energy to the Murnaghan equation of state.[161] The cell volume for other alloy supercells is determined while optimizing the cell atomic positions. Each supercell geometry's atomic positions are fully relaxed, that is, lattice constants and internal cell parameters are optimized, until the residual forces are below 1 meV/Å. Then the cell volume

is contracted to match the experimentally measured lattice parameter. The density of states is calculated using the tetrahedron method with Blöchl corrections for 672 bands and atomic orbital projections are calculated for each ion and band.

3.7 Experimental XAS methods

In this section, we will cover the basics of synchrotron radiation and the major components of the APS at ANL. Next, we will discuss the details of the steady-state XAS experiments and the methods used in fitting the XAS data. Finally, we will present the details for the time resolved-XAS (TR-XAS) experiments.

3.7.1 Synchrotron radiation

The X-ray spectroscopy experiments were done at the APS, which is a third-generation synchrotron facility. The X-rays produced by synchrotron radiation facilities are a billion times brighter than the X-rays used in a dentist's office. Scientists travel from all around the globe to use the APS facility, coming from variety of fields including, but not limited to, materials science, biology, physics, chemistry, geology, and planetary science.

Figure 3.3: Aerial view of the APS. Reproduced from Reference 162.

X-rays are produced by the acceleration of charged particles. A synchrotron light source is composed of several several electron accelerator components. The APS contains a linear accelerator (linac) and a smaller synchrotron, called a booster ring (Figure 3.3). The linac and booster ring are used to accelerate the electrons to the required GeV energy before injection into the storage ring. The storage ring is where the X-ray radiation is generated, which is then used in experimental end stations. We will explain briefly each component below. There are many textbooks on the subject for further reading.[116,117]

The electron source for the APS is a cathode heated to 1100 °C. Electrons are emitted by way of thermionic emission; that is to say, the increased heat of the cathode knocks electrons out of the atoms at the surface of the cathode into the vacuum chamber in which the cathode is housed. High voltage alternating electric fields in a linac accelerate the electrons produced by the cathode to an energy of 450 MeV. At these energies the electrons are relativistic, meaning that they are traveling at >99.999% of the speed of light (299,792,458 m/s). Next, the electrons are injected in the booster ring which comprises electromagnets that further accelerate the electrons from 450 MeV to 7 GeV, which corresponds to >99.999999% the speed of light. Four radio frequency (RF) cavities replenish the energy of the electrons that is lost by radiation. Dipole, quadrupole and sextupole magnets maintain the path of electrons. From the booster ring, the electrons are injected into the storage ring. The APS storage ring is composed of over 1,000 electromagnets and is just over 1.1 km in circumference.

The storage ring gets filled with many electron bunches, which circulate around the ring. Typically our experiments were done in what is called "24 bunch mode" at the APS. The ring current is maintained at 102 mA in 24 singlets (single bunches) with a nominal current of 4.25 mA and a spacing of 153 nanoseconds between singlets. The revolution frequency of the electron bunches is 272 kHz, and an electron bunch length is 33.5 ps (rms). The refill schedule is a continuous "top-up" with single injection electron pulses occurring at a minimum of two minute intervals. "Top-up mode" maintains an average current stability over all 24 bunches of <0.3%. The decay of a single bunch between top-ups can be as much

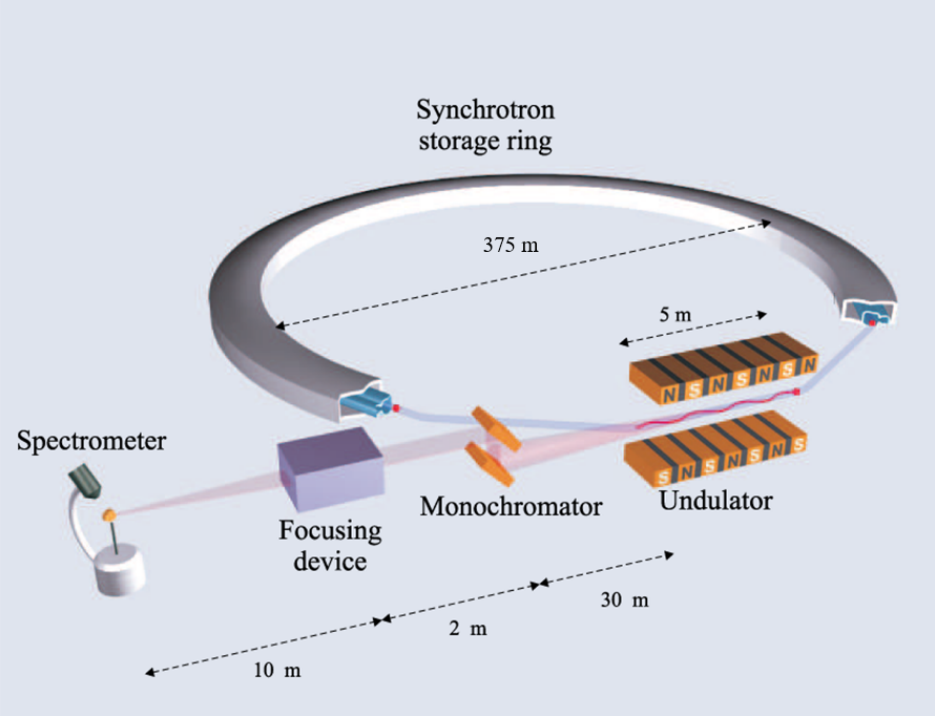

Figure 3.4: Schematic of the key elements of a typical beam line at a third-generation synchrotron X-ray source. The lattice of magnets in the radiation sources (bending magnets and undulators) force the electron bunches to oscillate along their path, and the electrons emit synchrotron radiation. Taken and modified from Als-Nielsen and McMorrow[116]

as 15%. Gated avalanche photodiodes (APD) or other flux detectors are used to monitor the time varying flux produced by selected electron bunches. X-ray pulses are produced at a repetition rate of 6.52 MHz and have a similar pulse duration as the electron bunches ($\backsim$40 ps rms).

There are two kinds of synchrotron radiation sources that comprise the storage ring: bending magnets (BMs), which provide a uniform magnetic field, and an insertion devices (IDs), which use a spatially periodic magnetic field. Insertion devices are inserted in the straight sections between adjacent BMs. The synchrotron radiation from IDs is coherent and much more intense than that from BMs. The APS consists of 34 sectors; each sector contains one or more beamlines. The emitted radiation ranges from infrared to gamma rays. The desired energy is selected by passing the X-ray beam through a monochromator. Most monochromators are Si(111) or (311) crystals that have an energy resolution of $\Delta E/E \approx$

1.4×10^4. Beamlines comprise additional crystals, mirror optics, and slits to control the beam size and divergence (Figure 3.4).

We performed experiments at both BM and ID beam lines at APS. The EXAFS data presented in Chapter 4 were collected at 9BM and 20BM, whereas the transient XANES data in Chapter 6 were collected at 7ID-D. For our time resolved XAS experiments, it was imperative for us to work at an insertion device beam line because of their higher flux and narrow X-ray beams. The changes in XAS spectra measured by time-resolved techniques are typically quite low ($\backsim$ 0.1 to 0.5 percent relative to the ground state spectrum). Therefore we need as much flux as possible. The small X-ray beam size achievable is important for the time resolved XAS experiments as will be discussed further in Section 3.7.3.

3.7.2 Steady-state XAS

An X-ray absorption spectrum can be measured by monitoring the transmitted X-ray intensity or by monitoring a secondary emission, such as X-ray fluorescence or Auger electrons, as a function of incoming X-ray energy. In transmission mode, the linear attenuation absorption coefficient $\mu(E)$ is expressed as:

$$\mu(E) = \frac{\ln\left(I_0/I\right)}{x} \ . \tag{3.14}$$

In X-ray fluorescence emission mode, μ is proportional to the ratio of the detected fluorescent photon intensity I_f and the incoming X-ray intensity I_0, as:

$$\mu(E) \propto I_f/I_0 \ , \tag{3.15}$$

where the proportionality constant includes factors that depend on the sample-detector geometry, and absorption of the fluorescent X-rays by other elements than the element of interest (*vide infra*).

Steady-state XAS experiments were performed at the 9 BM and 20 BM beam lines at

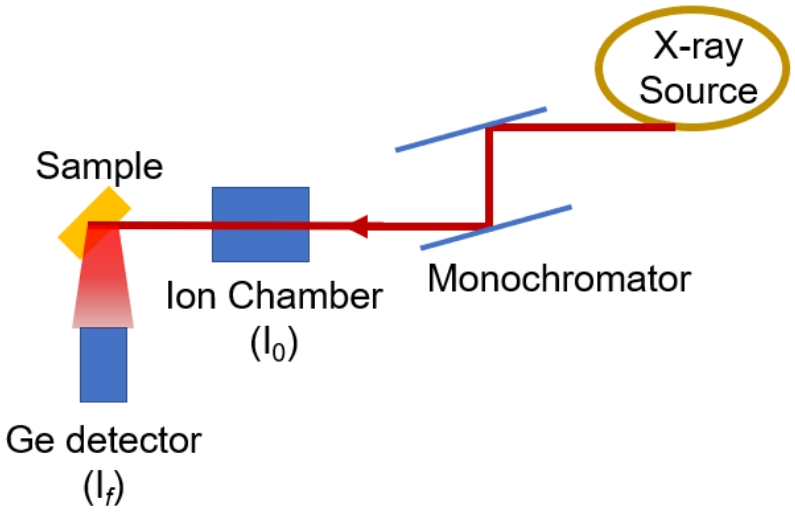

Figure 3.5: Sketch (top-view) of the detector setup used to measure the steady-state X-ray fluorescence spectra.

the APS. 1 mL of sample (approximately 800 nM particle concentration, which corresponds to elemental concentrations of 2 mM Se and 4 mM Zn in toluene) was loaded into a custom-made Teflon or aluminum liquid sample cell (see Figure 3.6). A 2.5-micron thin Mylar sheet was used to seal the sample cell. An ion chamber detector was used to monitor the X-ray intensity before the sample. Signal collection was done in partial fluorescence yield (PFY) mode with a Canberra 13-element Ge detector as shown in Figure 3.5. In PFY, photons resulting from a fluorescence process are discriminated with respect to their energy and selectively collected by a detector. Using this method, unwanted background radiation, such as elastic scattering, is removed to prevent distortion of the absorption spectra.

An ion chamber is used to measure I_0. The number of absorbed photons N_{ph} in the ion chamber is given by:[163]

$$N_{\mathrm{ph}}[\mathrm{ph/s}] = \frac{C[\mathrm{A}] \cdot E_1\,[\mathrm{eV}/e^-]}{E[\mathrm{eV}] \cdot e[C]}\ , \tag{3.16}$$

where C is the measured current, E_I is the ionization energy of the gas in the ion chamber, E is the energy of X-rays after the monochromator, and e is the elementary charge (the units are given between square brackets). The ion chamber is typically filled with 1 bar He gas which

absorbs about 0.1% of the incoming X-ray flux. Prior to the measurements, it should be checked that the detectors exhibit linear behavior for the range of fluxes and energies during the experiment. While this is usually easily achieved for ion chambers, the linearity of solid-state fluorescence detectors should be carefully checked. The monochromator energies were calibrated by measuring the spectra of a Zn, Se, and Sb (for the Cd and Te K-edges) foil in transmission.[121]

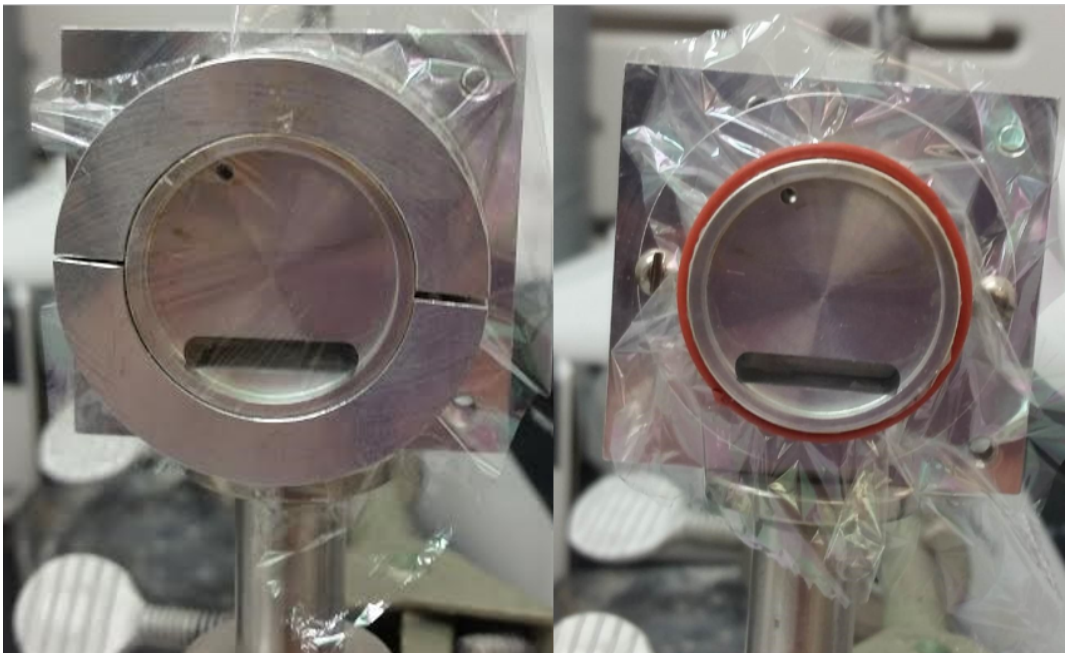

Figure 3.6: An aluminum liquid cell for steady sate fluorescence measurements.

Fluorescence modes of detection and the self-absorption effect

The relation $\mu(E)\ \alpha\ I_F/I_0$, which we introduced in Chapter 2, is oversimplified. While the probability of fluorescence is proportional to the absorption probability, the measured fluorescence intensity has traveled back through the sample to get to the detector. Since all matter attenuates X-rays, the fluorescence intensity, and therefore the EXAFS oscillations, are damped due to the so-called self-absorption effect.[164,165] In thin concentrated samples, the short absorption length leads to fewer photons being absorbed and more photons passing through the sample unabsorbed. The difference in the number of fluoresced photons is what is measured by the detector. In a thick sample, essentially no photons make it through

the sample unabsorbed; the sample is much thicker than an absorption length. In this scenario, small deviations of the absorption length will not lead to fewer absorbed photons because the sample is much thicker than an absorption length. The elements other than the primary absorbing element (referred to as matrix elements), aid our measurements. At any given energy, multiple elements compete to absorb incident photons. For example, in a fluorescence experiment setup as in Figure 3.7, where the sample is at an angle to the incoming X-ray beam and the detector, an increase in the absorption length (decrease in the absorption coefficient of element of interest) will lead to more incident and fluoresced photons being absorbed by the matrix elements. In other words, incident photons will travel deeper into the sample before being absorbed and fluoresced, and the fluoresced photons will have to travel through more sample to make it to the detector. Thus, the detector will measure a decrease in the signal due to the decreased absorption coefficient.

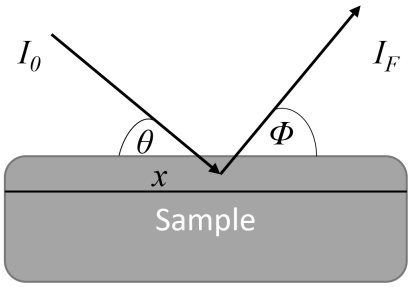

Figure 3.7: A fluorescence experiment setup with incident beam at 90° angle to the detector.

The full expression for measured fluorescence intensity is described by:[119,166]

$$I_F(E) = I_0(E)\frac{\epsilon_f \Omega}{4\pi}\frac{\mu_\chi(E)\left\{1 - e^{-\left[\mu_{\text{tot}}\ (E)/\sin\theta + \mu_{\text{tot}}\ \left(E_f\right)/\sin\phi\right]d}\right\}}{\mu_{\text{tot}}\ (E)/\sin\theta + \mu_{\text{tot}}\ \left(E_f\right)/\sin\phi}\ , \tag{3.17}$$

where θ and ϕ are the incident (I_0) and outgoing (I_F) angles with respect to the sample surface, respectively; ϵ_f is the fluorescence yield, Ω is the solid angle of detection; E_f is the energy of the fluorescent X-ray; $\mu_\chi(E)$ is the absorption from the element of interest, and $\mu_{\text{tot}}\ (E)$ is the total absorption in the sample: $\mu_{\text{tot}}\ (E) = \mu_\chi(E) + \mu_{\text{other}}\ (E)$. For the case of the sample holder like in Figure 3.6, $\theta + \phi = 90°$ and there is no longer dependence on the

angles, resulting in:

$$I_F(E) = I_0(E)\frac{\epsilon_f \Omega}{4\pi}\frac{\mu_\chi(E)\left\{1 - e^{-\left[\mu_{\text{tot}}\ (E)+\mu_{\text{tot}}\ \left(E_f\right)\right]d}\right\}}{\mu_{\text{tot}}\ (E) + \mu_{\text{tot}}\ (E_f)}\ . \tag{3.18}$$

In the case of our sample, which is a thick, dilute sample, the exponential term goes to zero, so that

$$I_F(E) = I_0(E)\frac{\epsilon_f \Omega}{4\pi}\frac{\mu_\chi(E)}{\mu_{\text{tot}}(E) + \mu_{\text{tot}}\ (E_f)}\ . \tag{3.19}$$

The EXAFS signal can then be approximated as:[164]

$$\chi_{\text{exp}} = \chi\left[1 - \frac{\mu_K(E)}{\mu_{\text{tot}}(E) + g\mu_{\text{tot}}\ (E_{fl})}\right] \equiv \chi[1 - S(E, \phi, \theta)] \tag{3.20}$$

where χ and χ_{exp} are the true EXAFS signal and the experimental EXAFS signal respectively, μ_K and μ_{tot} are the smoothly varying absorption coefficients of the element of interest and the total sample respectively, and g is the geometric factor $\sin\phi/\sin\theta$ (1 for our geometry). The reduction of the EXAFS signal due to self-absorption is then $1-S(E)$, and the correction factor is $1/(1 - S(E))$. Since μ_{tot} total includes μ_K, the numerator and denominator will have the same energy dependence, leading to a partial dampening of the EXAFS signal.

Looking at this function, we can tell that if the absorption coefficient is primarily due to Se ($\mu k \cong \mu_{tot}$) then there will be a very large impact on the data due to self-absorption. There could be two reasons that Se dominates the absorption: (1) Selenium is the most abundant element or (2) No other element significantly absorbs at the Se K-edge. From ICP-OES measurements discussed in Chapter 4, we know Se is not the most abdundant element, so we can discard the former possibility. In the latter, the composition of the nanoparticles does not change, so the impact of self-absorption does not depend on the concentration of nanoparticles, only the composition, which seems counterintuitive.[119] No matter how concentrated the sample, we will measure the same EXAFS spectrum. However, the impact of self-absorption will vary strongly with the edge measured.

XAS data reduction

Static X-ray spectra were analyzed using the FEFF-based Athena and Artemis EXAFS fitting packages,[124] including background subtraction, normalization, energy calibration, and single-shell Fourier analysis as described in Chapter 2. Bulk zinc blende ZnTe, CdTe, and CdSe crystal structures[146] were used as an input from which bond distances were refined. EXAFS analysis is prone to overfitting due to the large number of fitting parameters necessary for each coordination shell and the overlap of single- and multiple-scattering pathways resulting from similar bond distances in the vicinity of the absorbing atom. The guideline to prevent overfitting in the EXAFS community is that the number of variables should not exceed $\backsim 2/3$ of the number of independent points.

Global analysis is a very powerful approach to link data sets and reduce the number of fitting parameters in multicomponent samples. As such, we reduced the number of parameters significantly by performing a global fit of all four EXAFS data sets simultaneously and by using the same ΔR and σ^2 parameters at different ionization edges (*e.g.* the Zn-Te bond length change and mean-square disorder parameter are identical at the Zn and Te edges). The energy shift, ΔE_0, and coordination numbers,N, were fit for each absorption edge separately. To further reduce the number of fitting parameters, we measured EXAFS spectra on pure-phase CdSe and CdTe QDs and used the fitted amplitude reduction factors, S_0^2, at the Cd, Se, and Te edges as fixed parameters in the EXAFS fits of the CSQDs. Due to facile oxidation, we did not measure the EXAFS of pure-phase ZnTe QDs. Instead, we use the S_0^2 parameter obtained from EXAFS fitting of a Zn foil. In this way, we were able to reduce the total number of free fitting parameters to 16, which is significantly less than the number of independent data points (47, see below for for details). Data were fit in R- and k-space simultaneously, and k-space EXAFS spectra were weighted with k, k^2, and k^3 to alleviate the correlation between parameters.

3.7.3 Time-resolved X-ray absorption spectroscopy

One common approach for studying photoinduced dynamics is by way of a pump-probe scheme. The sample is first excited by a pulse of light (the pump) and at a short time delay later, a second pulse of light (the probe) interrogates the excited sample. We gain time dependent information about the excited state and the subsequent relaxation back to ground state by scanning the delay between the two pulses. The time resolution is determined by the convolution of the pump and probe pulses. In this section, the first pulse is a 10 ps laser light pulse and the second is a 90 ps X-ray pulse. The experimental setup data acquisition process are described in Section 3.7.3. Results and discussion of the data collected from the time-resolved XAS methods are presented in Chapter 6.

Experimental setup

TR-XAS experiments were perform in the AMO hutch in sector 7ID-D at the APS. This insertion device beamline has an undulator and a double-crystal Si (111) monochromator. A silicon (311) is also available. Together the monochromator and undulator set the x-ray energy to either the Zn K-edge (9.6 keV) or to the Se K-edge (12.6 keV). The X-rays are focused in both directions by two Kirkpatrick-Baez (KB) mirrors to a spot size of $\backsim$3 by 5 μm at the sample position, as determined by scanning a pinhole with 50 μm diameter through the X-ray beam and measuring the transmitted intensity.

Sample environment

Nanoparticle samples suspended in toluene were circulated using a sapphire nozzle (Kyburz) to produce a flat liquid jet with thickness 200 μm and width of 6 mm. The jet was oriented 45° relative to the X-ray beam. A gear pump was used to flow the sample. The fastest we could run the jet and still achieve a stable jet was at a rate of $\backsim$ 173 mL/min, which is equivalent to 283 kHz. Due to the volatile nature we also set up a peristaltic pump to

refresh the evaporated toluene. The flow rate varied, but a typical value was a replenish rate of 0.1-0.2 mL per min. Due to the varied nature of the toluene solvent evaporation, the volume in the sample reservoir was monitored constantly to ensure the pump did not run dry or that the reservoir did not overflow. The volume in the sample reservoir was monitored from a camera outside the hutch. A portable exhaust hose was placed above the sample jet due to the toluene vapors.

The time-resolved experiments were performed during the 24 bunch electron filling pattern at the APS. The laser used for sample excitation was a Duetto (10 ps bandwidth) laser at its second harmonic (532 nm). The laser repetition rate was set to 283 kHz in accordance with the flow rate of the jet to refresh the sample between laser shots. Signal collection was done in total fluorescence mode with two APD detectors. The overall 90 ps time resolution was determined by the X-ray pulse length. Difference (on minus off) spectra were generated on a pulse-by-pulse basis in order to eliminate systematic errors due to drifts. We used two different laser the fluences at 532 nm to pump the sample: 30 mJ/cm^2 and 82 mJ/cm^2 (both in $(1/e^2)$ diameters). The pulse duration was 10 ps (FWHM) with a laser spot size of 24.47 $\pm$ 0.44 μm (H) and 23.07 $\pm$ 0.42 μm (V).

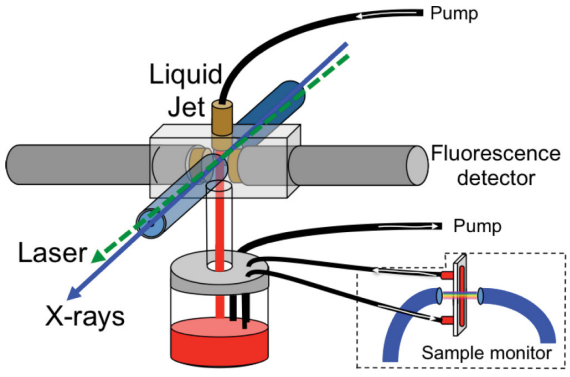

Figure 3.8: Schematic showing the liquid jet setup for flowing samples in a closed loop refresh fashion. The setup also includes a separate loop intended for monitoring the sample for damage via UV/vis spectroscopy. reproduced from Reference 167.

Experimental challenges for XTA on nanoparticle suspensions

We intended to monitor damage to the sample through monitoring the UV/vis absorption spectrum. The sample was sent through a flow cell through which the transmission of a white light source was monitored on a small spectrometer (Ocean Optics), as shown in Figure 3.8. This strategy has been successful for solutions of molecular complexes like as described by March and coworkers.[167] The approach, however, was not useful for our nanoparticle suspension due to the lack of sharp absorption features in the UV/vis spectrum (see Chapter 4) and the slight variations in sample concentration due to solvent evaporation. In addition, we observed aggregation of the sample on the window of the quartz flow cell. The deposition of the sample on the window of the flow cell inhibited our ability to detect changes in sample intensity. Because monitoring sample damage by way of *in situ* UV/vis was unsuccessful, we instead watched for changes in the X-ray absorption intensity and spectral features, particularly changes or shifts of the white line, on a scan by scan basis.

As alluded to above, the flow rate which produces a stable jet ultimately determines the repetition rate of the experiment. We initially intended to circulate the sample by a high-performance liquid chromatography (HPLC) pump through a 130 μm diameter quartz nozzle that produced a cylindrical liquid jet available at Sector 7.[168] The flow rate required to fully refresh the sample volume between laser shots is 25 ml/min, which equates to jet speed of $\backsim$ 25 m/s. In this configuration, the repetition rate of the experiment is 1.3 MHz, and the laser pulses overlaps every 5th x-ray pulse. Increasing the repetition rate has been revolutionary in the field of TR-XAS because it significantly reduces the time required to average data to achieve a good signal to noise. Unfortunately, the nature of the aggregation damage of the nanoparticle lead to clogging of the HPLC pump. While these fast flowing experimental set-ups have been successfully carried out for molecular complexes,[168] future work is required to adapt these set-ups to nanoparticle suspensions.

Data acquisition scheme

The experimental set up at Sector 7 at APS was such that the laser beam crossed the X-ray beam with a small (5-10°) angle. The laser was spatially overlapped with the X-rays at the jet position using a 50 μm diameter pinhole. Temporal overlap between laser and X-rays was achieved using a metal-semiconductor-metal (MSM) detector (Hamamatsu) to 10 ps precision, with a rise time of 30 ps. During the timing overlap, the MSM detector was positioned in place of the sample. The X-ray beam and attenuated laser beam were shone on the detector. A 3.5 GHz, 40 Gs/s digital oscilloscope (LeCroy, Wave-Pro 735Zi) was used to monitor pusles from both the laser and X-ray beams. Pluses from each beam are displayed on the oscilloscope as a single trace. To overlap the laser pulses and X-ray pulses in time, the delay of the laser pulses was electronically adjusted. The temporal overlap was then precisely determined by cross correlation of the laser and X-rays monitoring by a laser-induced feature in the X-ray absorption spectrum. More details on the set up at Sector 7 can be found in the work by March and coworkers.[167,168]

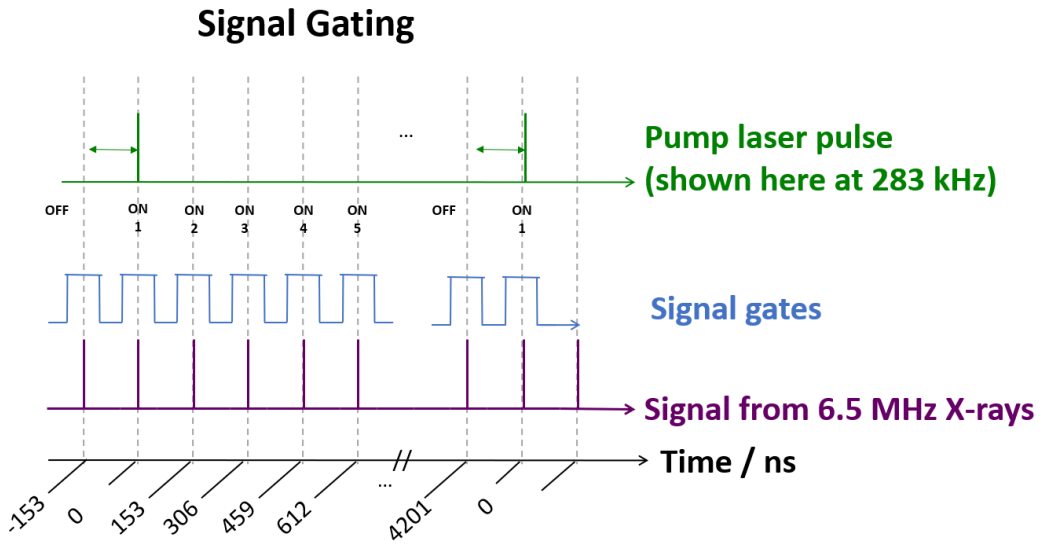

Figure 3.9: Data acquisition scheme to record laser-on/laser-off data at 283 kHz. Electronic gates are used to distinguish counts from X-ray pulses from a selected bunch and also those from X-ray pulses that are overlapped with the laser pulses. Adapted from Reference 167.

XAS spectra were collected in fluorescence mode using an avalanche photodiode (APD, Oxford Instruments) and a scintillator detector positioned at 90° relative to the incident X-ray beam, as pictured in Figure 3.8. The APD detector was operated in analog mode to detect multiple fluorescence photons per shot. A MHz digital boxcar average (UHFLI, Zurich Instruments) provided average signals for the X-ray pulses input from the APD. During this experiment, we were limited to just two gates for box car averaging. The signals just preceding the laser-overlapped pulses (OFF) and the X-ray pulses overlapped with laser pulses (ON) were averaged by the box car. The averaging time per data point was 11 seconds. Transient spectra shown in Chapter 6 were constructed by the difference between pumped (laser excited) and unpumped (ground state) XAS spectra. The scintillator signals were not input into a boxcar, and as such we were able to use up to 6 gates, as shown in Figure 3.9. Due to the low signal intensity and the lower efficiency of the scintillator, the signals were much noisier than the signals from the boxcar averaged APD.

Pump-probe XAS signals

In TR-XAS, we measure the difference between pumped (laser-excited) and unpumped (ground-state) XAS spectra. We the define the transient fluorescence spectrum as

$$\Delta I_F(t,E) = \frac{I_F^{\mathrm{pu}}(E,t) - I_F^{\mathrm{up}}(E)}{I_0(E)} \tag{3.21}$$

where $I_F^{\mathrm{pu}}(E,t)$ is the fluorescence intensity from the pumped sample, and $I_F^{\mathrm{up}}(E)$ is the fluorescence from the unpumped sample from the boxcar gates, and $I_0(E)$ is the incident X-ray intensity. The normalized signal is obtained by dividing by the edge jump, according to

$$\Delta I_F^{\mathrm{norm}}\,(t,E) = \frac{\Delta I_F(t,E)}{\Delta I_F^{\mathrm{edge}}}\ , \tag{3.22}$$

where $\Delta I_F(E,t)$ is the difference of the pumped and unpumped fluorescence intensity, and

ΔI_F^{edge} is the approximate edge-jump magnitude of the steady-state fluorescence spectrum $I_F^{\text{up}}(E)/I_0(E)$.

3.8 Heat equation and temperature profile

Temperature profile calculations were performed by Yuanheng Wang. To estimate the temperature profile of QDs after laser excitation, the heat equation [169] is solved, with the assumption of classical (no quantum confinement effects), spherical, and homogeneous nanoparticles:

$$c_p \rho \frac{\partial \tau}{\partial t} = \nabla \cdot (k \nabla T) + q_v = k \left(\frac{\partial^2 \tau}{\partial r^2} + \frac{\partial}{r} \frac{\partial \tau}{\partial r} \right) + q_V \ , \tag{3.23}$$

where $T(r,t)$ is the temperature at time t and radius r inside the QD, c_p, ρ and k are the average specific heat capacity, density and thermal conductivity of the QD, and q_V is the volumetric heat source. Since the laser spot size is much larger than QD size, each QD is assumed to heat up evenly (q_V is not a function of r). We assume that the time between successive laser pulses is long enough for QDs to cool down to room temperature $T_{r.t.}$, so there is no heat accumulation, and q_V can be described by a single Gaussian laser pulse:

$$q_V = \frac{(1-P) \cdot q_{QD}}{\left(\frac{4}{3}\pi R^3\right) \cdot \sqrt{2\pi}\tau} e^{-\frac{(t-t_0)^2}{2\tau^2}} \ , \tag{3.24}$$

where R and $\frac{4}{3}\pi R^2$ are the radius and volume of the spherical QD, and τ is related to the full-width-half-max (FWHM) duration of laser pulses by $\tau = \frac{\text{duration}}{2\sqrt{2\ln 2}} \cdot P$ is the conversion rate of laser energy to electronic energy, and is estimated by the difference between pump laser wavelength and the first excitonic peak wavelength (from UV-vis spectra):

$$P = \frac{h v_{\text{exciton}}}{h v_{\text{total}}} = \frac{\lambda_{\text{pump}}}{\lambda_{\text{exciton}}} \ . \tag{3.25}$$

q_{QD} is the average energy received by one QD for each laser pulse, and for colloidal QD solution in a sample holder (a liquid jet in our setup), it can be approximated using Beer's

law:

$$q_{QD} = \frac{\ln 2 \cdot f \text{ luence}}{\text{lc}\, N_A} \left(1 - 10^{-\varepsilon l c}\right) \ , \tag{3.26}$$

where ε, l and c are the molar absorptivity, light path length and molar concentration of the QD sample, respectively and N_A is Avogadro's number. The laser fluence is defined by laser pulse energy divided by spot size and is given in J/cm^2. The constant $\ln 2$ is related to the ways of description of the spot size. Assuming a Gaussian shaped laser spot, if the spot diameter is defined in FWHM, the constant is ln(2); if it is defined in $1/e^2$, the constant is 2 instead.

The boundary condition of the heat equation is determined by interface property between a QD and the solvent, the interfacial thermal conductance G:

$$G\left(T_{r,t} - T(R)\right) = k \frac{\partial \tau}{\partial r}\bigg|_{r=R} \ . \tag{3.27}$$

A pure CdTe QD is considered here, since the thermal properties of CdSe, CdTe and ZnTe, three materials show up in our CSQDs, are similar. The maximum temperature of QDs after laser absorption is mainly determined by the laser fluence and the heat capacity of the material. This maximum temperature is higher than the boiling point of the solvent (toluene) regardless of G value, suggesting a more complex system with likely bubble formation around the nanoparticles. We use two G values from the literature as extremes: 90×10^6 W/m^{2}K which describes a hexane/hexylamine/CdSe interface, that is a CdSe with complete ligand coverage in a nonpolar solvent, and 3.6×10^6 W/m^{2}K which is a bare hexane/CdSe interface.[170] The time scale of heat diffusion depends mainly on the interfacial thermal conductance. MATLAB code used for temperature profile calculations can be found in the Supplementary material.

3.9 Supplementary material

3.9.1 MATLAB code used for temperature profile calculations

```
function a()
R = 3; nm
G = 100*10^6; units of W/m2K
t_end = 35*10^5; units of fs
timestep = 10000; units of fs; 10000 fs = 10 ps
fluence = 80 * 0.622 units of mJ/cm2 including the conversion rate
conductivity = 9; units of W/mK
capacity = 262; units of J/kgK
density = 5.8; units of g/cm3
T_environment = 298; units of K
concentration = 5.15*10.^9; units of mol/L
path_length = 200*10^4; units of cm
epsilon = 1.46.*10.^6; units of L/molcm
duration = 10*10^3; units of fs
initialtime = 40*10^3; units of fs
x = linspace(0, R); 100 elements array for radius r
t = [0 :  timestep :  t_end];
G = 90*10^6; hexane/hexylamine/CdSe(WZ) interface
sol = pdepe(0, @pdefun, @pdeic, @pdebc, x, t);
T_t_x1 = sol(:, :, 1);
plot(t/10^3, T_t_x1(:,1),'color',[0.8,0.8,0.8], 'linewidth',2);
xlabel('t (ps)');
ylabel('T (K)');
set(gca,'fontsize',15);
hold on;
G = 3.6*10^6; bare hexane/CdSe(WZ) interface
sol = pdepe(0, @pdefun, @pdeic, @pdebc, x, t);
T_t_x2 = sol(:, :, 1);
plot(t/10^3, T_t_x2(:,1),'-','color',[0.5,0.5,0.5], 'linewidth',2);
legend('High G limit','Low G limit');
save HeatSimData
function [c, f, s] = pdefun(x, t, u, du) Partial differential equation c * du/dt =
d/dx(f) + s
c = capacity * density / conductivity;
f = du;
pulse_width = duration * 0.424661;
pulse_height = fluence / concentration / path_length / pulse_width / (R^3) * (1 - 10^(-
concentration * path_length * epsilon)) * 0.1581504674;
s = 2 ./ x .* du + pulse_height ./ conductivity .* exp(-((t - initialtime) ./
pulse_width).^2 ./ 2);
end
```

MATLAB code used for temperature profile calculations cont.

```
function [pl, ql, pr, qr] = pdebc(xl, ul, xr, ur, t) Boundary condition
pl = 0; r=0 value
ql = 1; r=0 derivative
pr = ur - T_environment; r=R value
qr = conductivity / G * 10.9̂;  r=R derivative
end
function [u0] = pdeic(x) Initial condition
u0 = T_environment;
end
end
```

Chapter 4

Internal and electronic structure determination

In this chapter, we show that ZnTe/CdSe core/shell quantum dots synthesized by a standard literature procedure in actuality have an alloyed $Cd_xZn_{1-x}Te$ core. We employ global fitting analysis of XAS at all four K-shell ionization edges (Zn, Te, Cd, Se) to extract the first-shell bond distances. We combine our XAS results with TEM sizing and elemental analyses, which allows us to propose models of the internal particle structure. Our multimodal characterization approach confirms (1) the presence of Cd-Te bonds, (2) cation alloying in the particle core (and the absence of anion alloying), and (3) a patchy pure-phase CdSe shell. Our structural analysis is extended with electronic band structure calculations, demonstrating that the alloyed $Cd_xZn_{1-x}Te$/CdSe core/shell quantum dots exhibit a direct band gap, different from the predicted type-II band alignment of the intended ZnTe/CdSe core/shell quantum dots. We highlight the challenges with synthesizing II-VI quantum dot heterostructures and the power of XAS for understanding the internal structure of heterogenous nanoparticles. The results from this chapter are published in part in Reference 171.

Acknowledgements The nanoparticle models and band structure calculations were performed by Yuanheng Wang. The majority of the sample characterization was performed at the Materials Research Laboratory (MRL) Central Facilities at the University of Illinois at Urbana-Champaign (UIUC). Inductively coupled plasma-optical emission spectrophotometer (ICP-OES) measurements were carried out by the Microanalysis Laboratory in the School of Chemical Sciences at UIUC. In particular, we acknowledge Dr. Jim Mabon for assistance

in S/TEM on the Themis Z, Dr. Rick Haasch for help with the XPS measurements, and Frank Alcorn for high resolution imaging on Hitachi TEM. We gratefully acknowledge Insung Han and Prof. Shoemaker for measuring the X-ray Diffraction (XRD) pattern. This research used resources of the Advanced Photon Source (APS), a U.S. Department of Energy (DOE) Office of Science User Facility operated for the DOE Office of Science by Argonne National Laboratory (ANL) under Contract No. DE-AC02-06CH11357. We thank Dr. George Sterbinsky, Dr. Tianpin Wu, and Dr. Steve Heald for assistance during measurements at the APS. We also thank the members of the van der Veen lab for their assistance during the EXAFS beam times: Dr. Renske van der Veen, Conner Dysktra, Tyler Haddock, Rachel Wallick, and Yuanheng Wang. We thank Dr. Thomas Rossi, Dr. Michael Enright, and Dr. Leslie Hamachi for fruitful discussion.

4.1 Materials characterization

Conventional techniques including UV/Vis and PL spectroscopy, XRD, TEM, ICP-OES, and XPS, were used to characterize the CSQDs. CSQDs were synthesized via the one-pot SILAR method as discussed in Section 3.1.2. Four QD samples were prepared using this method: SILAR 0.5, SILAR 1, SILAR 2 and SILAR 3. The SILAR 0.5 sample was prepared by adding Cd prescursor only, which is the first half of the SILAR procedure, and with no subsequent addition of no Se. The results of these techniques presented in this section, provide information pertinent to the optical properties, crystallinity, elemental compositions, and nanoparticle size of the CSQDs. The knowledge obtained from these characterization techniques was used to build the nanoparticle models described later in Section 4.3.

4.1.1 UV/vis and photoluminescence spectroscopy

Figure 4.1a shows the results from UV/Vis spectroscopy on the ZnTe cores and the SILAR 1, SILAR 2, and SILAR 3 samples. As the number of SILAR cycles increases and the

particles grow, a clear red shift and decrease in the first exciton intensity is observed. This behavior is typically interpreted as the appearance of a spatially indirect transition, that is, a charge transfer state across the interface between the two semiconductors, which extends the absorption of type-II CSQDs to longer wavelengths and reduces the electron-hole wave function overlap.[36,40,43,172] As discussed below, however, the red shift can also be due to alloying. In Figure 4.1b, we show the UV/vis spectra and corresponding PL spectra for SILAR 2 and SILAR 3. These are the only two samples which had detectable PL. The low quantum yield can indicate either Type-II charge transfer or the presence of many charge carrier traps which are a detriment to radiative decay.[22,173,174] In Figure 4.1b, we also plot the data with the first derivative of the SILAR 2 UV/vis spectrum to highlight the features of the UV/vis at 705, 605, and 465 nm. Finally, in Figure 4.1c, we compare the time-resolved PL for SILAR 2 and SILAR 3. We obtained $\backsim$10 $\pm$ 0.1 ns and $\backsim$75 $\pm$ 2 ns (mean decay time) for the SILAR 2 and SILAR 3 sample, respectively.

4.1.2 XRD

The XRD data on SILAR 2 (Figure 4.2) shows that the CSQDs are highly crystalline. As expected, the peaks are broadened due to small crystallites present in nanoparticles.[116] The Debye-Scherrer equation gives a crystal domain size of 1.67 nm for the SILAR 2 sample. Given that the particles are 5.8 $\pm$ 0.7 nm (shown by TEM analysis below), we infer that each QD has multiple crystal domains present,[175] which is in agreement with HR-STEM (Figure 4.4). The fit of XRD to a zinc blende lattice yields a lattice constant of 6.3 $\pm$ 0.1 Å, which is larger than the bulk lattice constants of ZnTe (a = 6.10 Å)[146] and CdSe (a = 6.08 Å).[146] Although XRD could indicate a contribution of CdTe, which has a larger lattice component (a = 6.48 Å),[146] the size-broadened peaks make it difficult to uniquely identify and quantify the contribution of CdTe to the overall nanoparticle structure. In addition, conventional UV/vis, TEM, and XRD characterization methods are not ideally suited to determine the nature of the interface in nanoheterostructured materials, that is, whether or

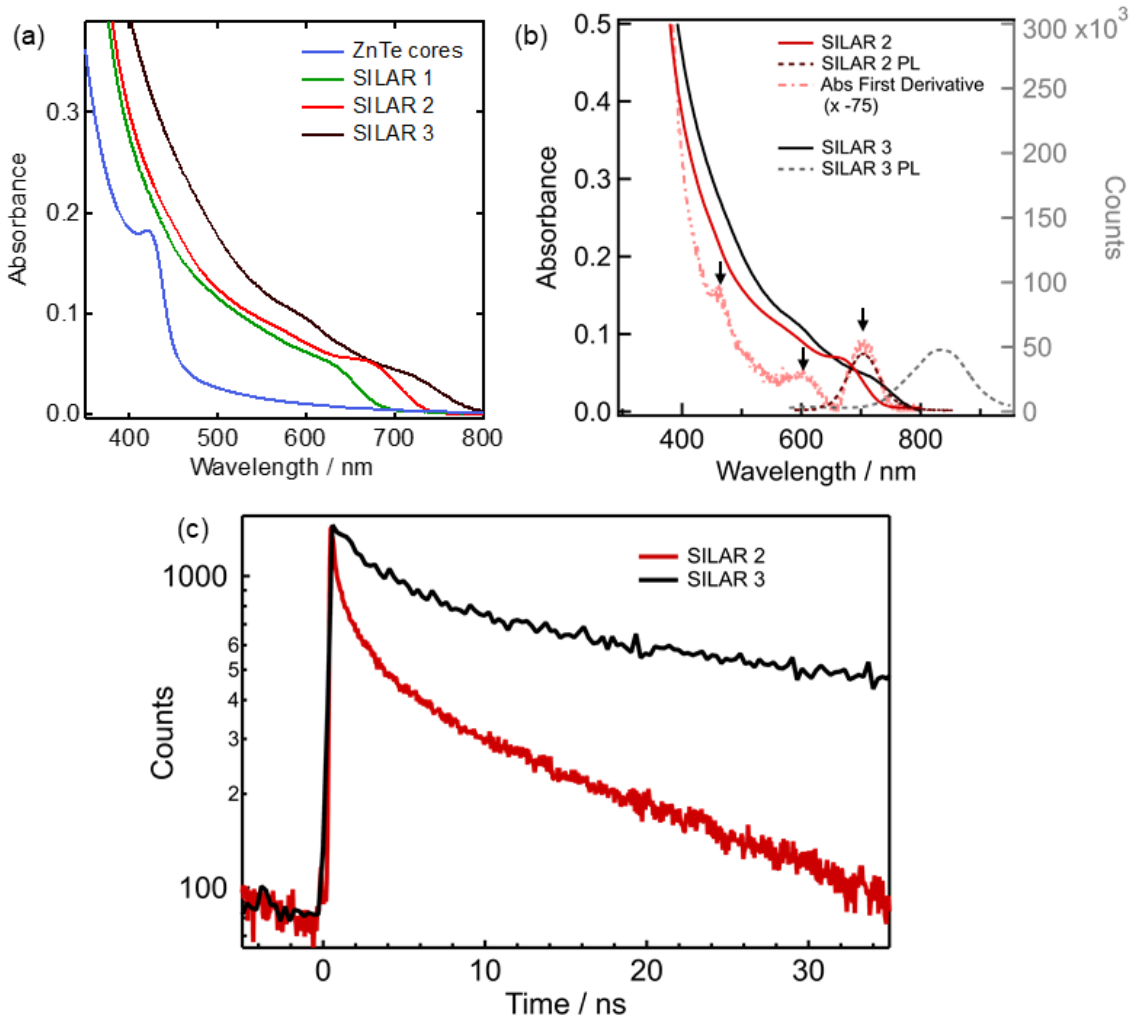

Figure 4.1: a). UV/vis spectra of 3.1 ± 0.5 nm ZnTe cores (blue), 5.0 ± 0.8 nm CSQDs after one SILAR cycle (SILAR 1, green), 5.7 ± 0.7 nm CSQDs after two SILAR cycles (SILAR 2, red), and 6.6 ± 0.6 nm CSQDs after three SILAR cycles (SILAR 3, black). (b) UV/vis spectra (left axis) of the SILAR 2 (5.7 ± 0.7 nm, red) and SILAR 3 (6.6 ± 0.6 nm, black) CSQD sample (6.6 ± 0.6 nm, black). The dashed dark red and gray traces are PL at 535 nm excitation for SILAR 2 and SILAR 3, respectively (right axis). Quantum yields were less than 1% for the washed SILAR 2 and SILAR 3 samples. (c) Photoluminescence decay curve at 535 nm excitation for SILAR 2 (red) and SILAR 3 (black).

not there is an (gradient) alloy or sharp interfaces with epitaxial strain.

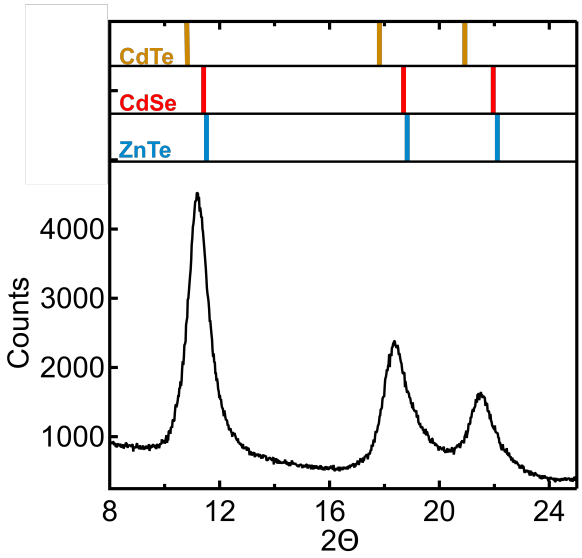

Figure 4.2: Powder XRD pattern of SILAR 2 CSQDs. The top of the plot shows line spectra for bulk zinc blende ZnTe (blue), CdSe (red), and CdTe (yellow). Lattice constants obtained from Reference 146.

4.1.3 TEM size analysis

TEM is a reliable method for determining the overall particle size and crystallinity of semiconducting nanoparticles. Here, we show representative TEM images of the ZnTe cores and the CSQD samples SILAR 0.5 through SILAR 3 (see Figure 4.3 a through j). In Figure, 4.3k, we include a representative high resolution TEM image of a SILAR 2 CSQD sample (5.8 ± 0.7 nm) taken on the Themis Z TEM at the MRL. The line profile (Figure 4.3l) across the length of a representative QD reveals a d_{111}=0.37 nm lattice spacing. In Figures 4.4, we include representative high-resolution STEM images of CSQD sample SILAR 2 taken on a Themis Z TEM. The TEM data demonstrate the crystallinity of the CSQDs, but a detailed atomic-scale structural analysis is precluded due to the absence of intraparticle contrast variations in the STEM images. Energy dispersive spectroscopy (EDS) STEM was attempted, but due to substantial electron-beam induced sample damage, it could not be used to obtain element-specific information about the particle structure.

High-resolution electron microscopy has been successfully applied in the characterization

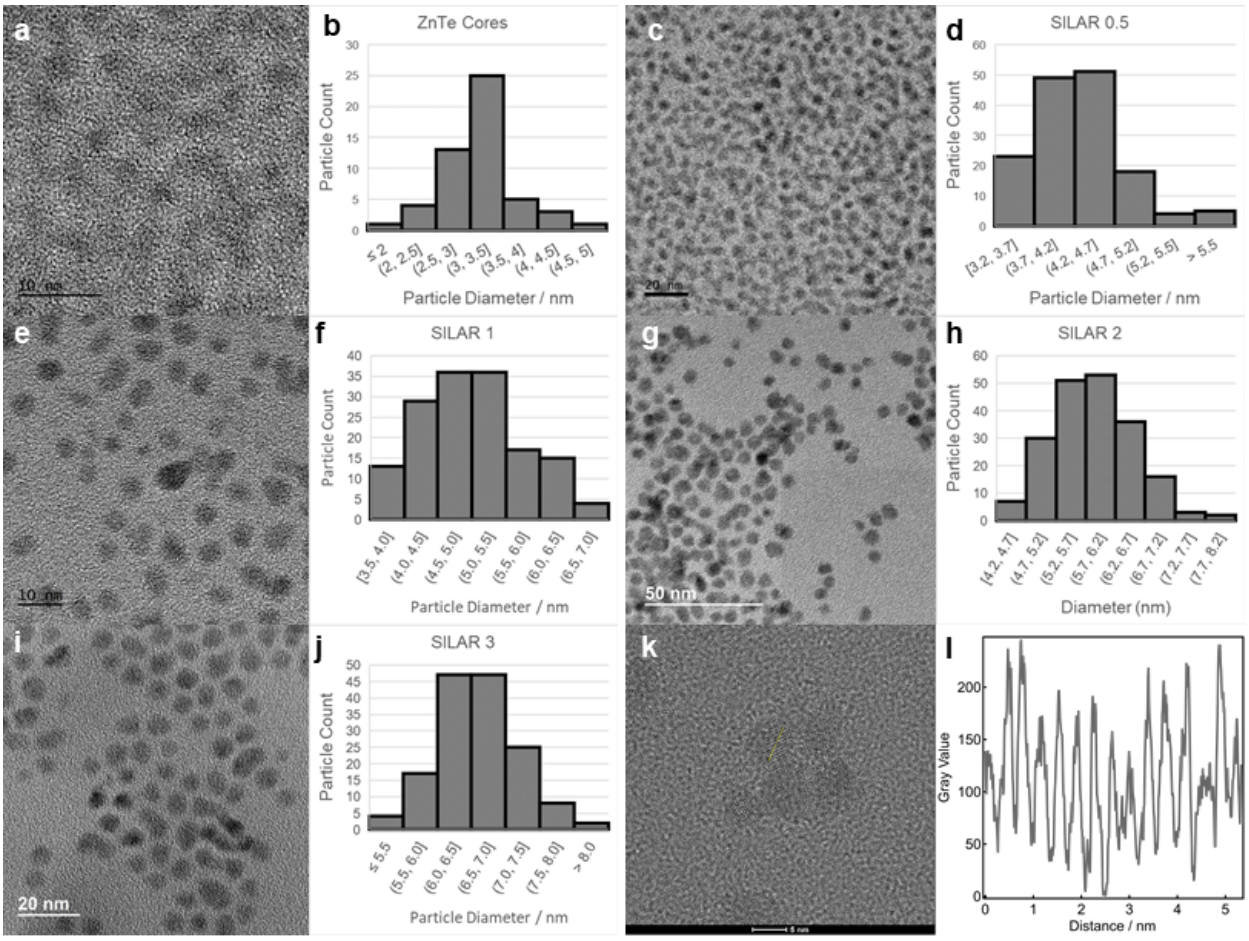

Figure 4.3: Representative TEM images for CSQDs samples. Next to each TEM image, we include the particle diameter histograms for each sample. In the particle diameter histograms, a parenthesis means that end is exclusive and doesn't contain the listed element. For [first, last), the range starts with first (and includes it) but ends just before last. (a-b) Representative image of ZnTe cores. Average particle diameter 3.1 ± 0.5 nm. (c-d) Representative image of ZnTe cores after Cd deposition (SILAR 0.5 sample). Average particle diameter 4.3 ± 0.5 nm. (e-f) Representative image of SILAR 1. Average particle diameter 5.0 ± 0.8 nm. (g-h) Representative image of SILAR 2. Average particle diameter 5.7 ± 0.7 nm. (i-j) Representative image of SILAR 3. Average particle diameter 6.6 ± 0.6 nm. (k) Representative high resolution TEM image of a SILAR 2 (5.8 ± 0.7 nm) with (l) a line profile across the length of a representative quantum dot. The line profile reveals a d_{111}=0.37 nm lattice spacing.

of heterostructured nanomaterials,[46,50–53] but its use for core/shell QDs is limited due to their spherical symmetry. Often in the literature the shell thickness is determined by the difference between the radius of the CSQDs and radius of the bare cores. This approach is too simplistic as it does not account for the possibility of alloying of the core and shell materials and/or oxidation of the core material in the course of the TEM grid preparation

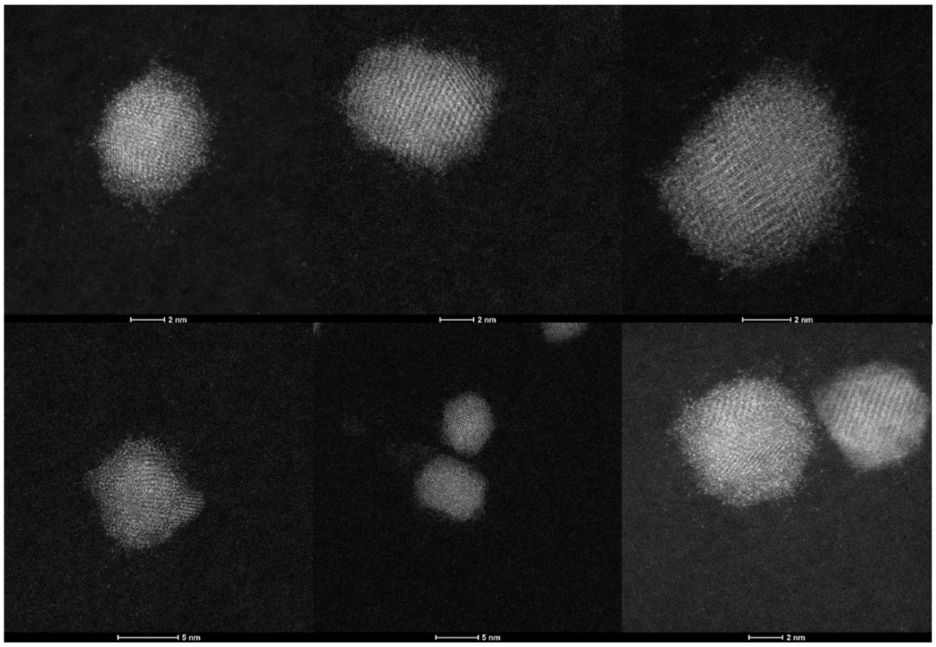

Figure 4.4: Representative high-resolution STEM images of CSQD sample SILAR 2. Average particle diameter 5.7 ± 0.7 nm.

that can alter particle sizes. The characterization of a core/shell structure by way of TEM analysis alone is especially challenging in our case where the semiconducting materials have both similar lattice spacing and similar atomic Z numbers.

4.1.4 ICP-OES

We present the elemental composition of all the samples determined by ICP-OES in Table 4.1. Characterization of the ZnTe cores by ICP-OES indicates that the ZnTe core are zinc-rich with a zinc to tellurium ratio of 1:0.56. ICP-OES evaluation of the SILAR 2 sample indicates a Zn:Cd:Te:Se ratio of 1.0:5.2:6.0:1.4., which is in good agreement with the ratios reported by Enright *et al.*: 1.0:8.6:7.4:1.7. The zinc to tellurium ratio increases dramatically to 1.0:2.7 after exposure to the cadmium precursor in SILAR 0.5. In SILAR 1-3, there is selenium present in the CSQDs. The ratio of elements present in these reported nanostructures suggests that the structure is predominately of Cd and Te, with the ratio of Cd and Te increasing with the number of SILAR cycles. Of course, the limitation of ICP-OES is that

Table 4.1: Summarized results from ICP-OES and TEM. n denotes the number of samples that was used to determine the elemental fraction averages and standard deviations. The Zn fraction was set to 1.0 and all other fractions are relative to Zn. The particle diameters were determined using TEM.

Sample	Zn Fraction	Te Fraction	Cd Fraction	Se Fraction	Particle Diameter (nm)
ZnTe core (n=1)	1.0 ± 0.05	0.56 ± 0.03	-	-	3.1 ± 0.5
SILAR 0.5 (n=2)	1.0 ± 0.2	2.7 ± 0.8	1.9 ± 0.7	-	4.3 ± 0.5
SILAR 1 (n=3)	1.0 ± 0.1	1.8 ± 0.2	1.3 ± 0.2	0.2 ± 0.1	5.0 ± 0.8
SILAR 2 (n=8)	1.0 ± 0.2	5.2 ± 0.6	6.0 ± 1.0	1.4 ± 0.4	5.7 ± 0.7
SILAR 3 (n=3)	1.0 ± 0.1	5.7 ± 0.3	11.1 ± 1.4	5.3 ± 1.0	6.6 ± 0.6

we do not know how the Cd and Te atoms manifest in the sample, that is in the presence of a CdTe inner layer or in alloy.

4.1.5 X-ray photoelectron spectroscopy analysis

For sub 10 nm nanoparticles, XPS is routinely used to identify elements, their chemical states and their local bonding environment. In heterogenous ZnTeCdSe quantum dots of interest, all the cation and anions have the same nominal oxidation state respectively. The local binding environment, however, is also affected by bonding hybridization to nearest-neighbor atoms, and sometimes the bonding hybridization between the absorbing atom and the next-nearest-neighbor atom. We measured the binding energy of nanoparticles after a variety of SILAR cycles, and compared them to pure-phase CdSe and CdTe QDs. Our goal was to determine any shifts in the binding energies due to alloying. We present the XPS data below and describe why the interpretation of the data is unclear.

The peak-fitting process of high-resolution XPS spectra is still a mixture of art, science, knowledge, and experience. Instrument design, instrument components, experimental set-

tings, and sample variables all impact the fitting process. Most instrument parameters are constant, while others depend on the choice of experimental settings. Convention is to use the peak of adventitious carbon to calibrate the peak positions. The carbon peak is fit to a convolution of Gaussian peaks and the lowest binding energy peak is calibrated to 285.0 eV, which is the nominal binding energy of a C 1s electron. Solution processed nanoparticles typically have carbon-based ligands and the density of coverage, types of ligands, and-the-like, can vary from sample to sample. For this reason, it is challenging to calibrate the energy of solution processed nanoparticles. The inherently curved and strained surfaces of nanoparticles also contribute to the variation in work function from sample to sample, which make peak processing challenging. The challenge also extends to the proper fitting of the peaks. It is difficult to determine the peak shape and the correct number of line shapes required to fit a peak, therefore XPS data are prone to over-fitting and over-interpretation.[176] In addition, more complex modeling can be required of heterogeneous systems, such as the material under investigation here.

XPS was measured for all four elements (Cd, Te, Zn, and Se) on all four SILAR samples (0.5-3), CdSe QDs and CdTe QDs (Figures 4.6-4.8). The assignments of the peaks are likely not correct and represent first-pass guesses. They were determined based on reference data,[177] but are not verified. The assignment of the Zn data and the general assignment of chalcogenides versus oxides can be trusted, but the detailed assignment of alloyed structures or the mixture of two chalcogenide peaks are uncertain. Complex modeling would be needed to confirm our assignments. We find EXAFS spectroscopy—described in the following section—to be the most reliable way to determine the local bonding environment of atoms for our colloidal nanoparticle sample.

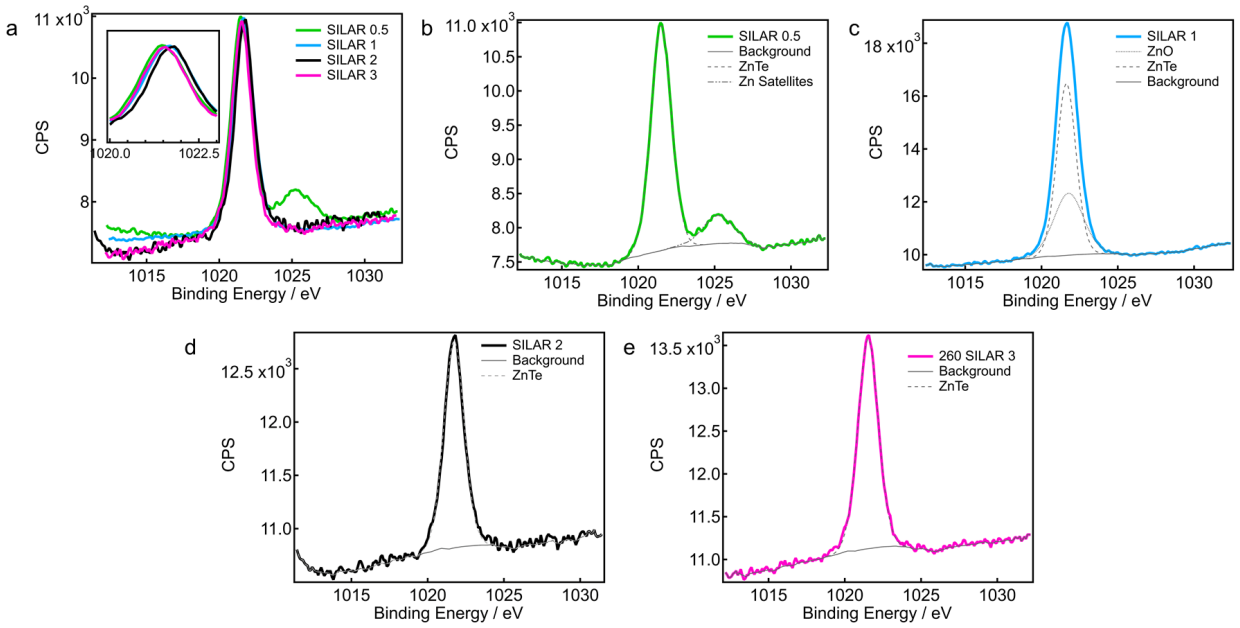

Figure 4.5: Zn XPS data. (a) All samples plotted and scaled in one graph; (b) SILAR 0.5; (c) SILAR 1; (d) SILAR 2; and (e) SILAR 3. The solid gray line is the fit to the background. The long dashed line are the peak fitting assigned to ZnTe. The short dashed lines is the fit to ZnO. Finally, the dot-dashed line is the assigned to Zn satellite or charging peaks. The labeling of the peaks for all these data is likely not correct and have not been verified.

Table 4.2: Zn XPS peak positions (in eV).

Zn $2p_{3/2}$			
	ZnTe	ZnO	Satellite
SILAR 3	1021.5		
SILAR 2	1021.7		
SILAR 1	1021.6	1021.8	
SILAR 0.5	1021.5		1025.2

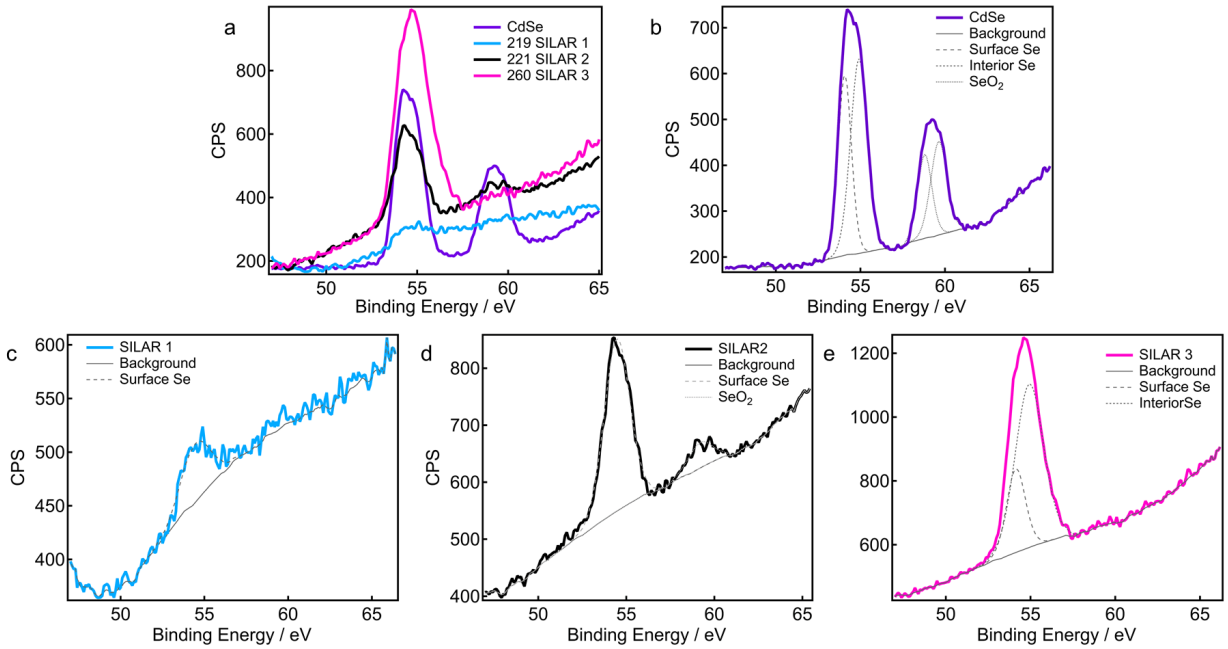

Figure 4.6: Se XPS data. (a) All samples plotted and scaled in one graph; (b) SILAR 1; (c) SILAR 2; and (d) SILAR 3. The solid gray lines are the fit to the background. The long dashed lines are the peak fitting assigned to Surface Se. The medium dashed lines are the fit assigned to interior Se. The short dashed lines are the fit to SeO_2. The assignment of the peaks for all these data is likely not correct and have not been verified

Table 4.3: Se XPS peak positions (in eV). The assignments of the peaks for all these data is likely not correct and have not been verified.

	CdSe		SeO_2	
CdSe	54.1	54.9	58.8	59.6
SILAR 3	54.1	54.9		
SILAR 2	54.5		59.2	
SILAR 1	54.4			
SILAR 0.5	-			

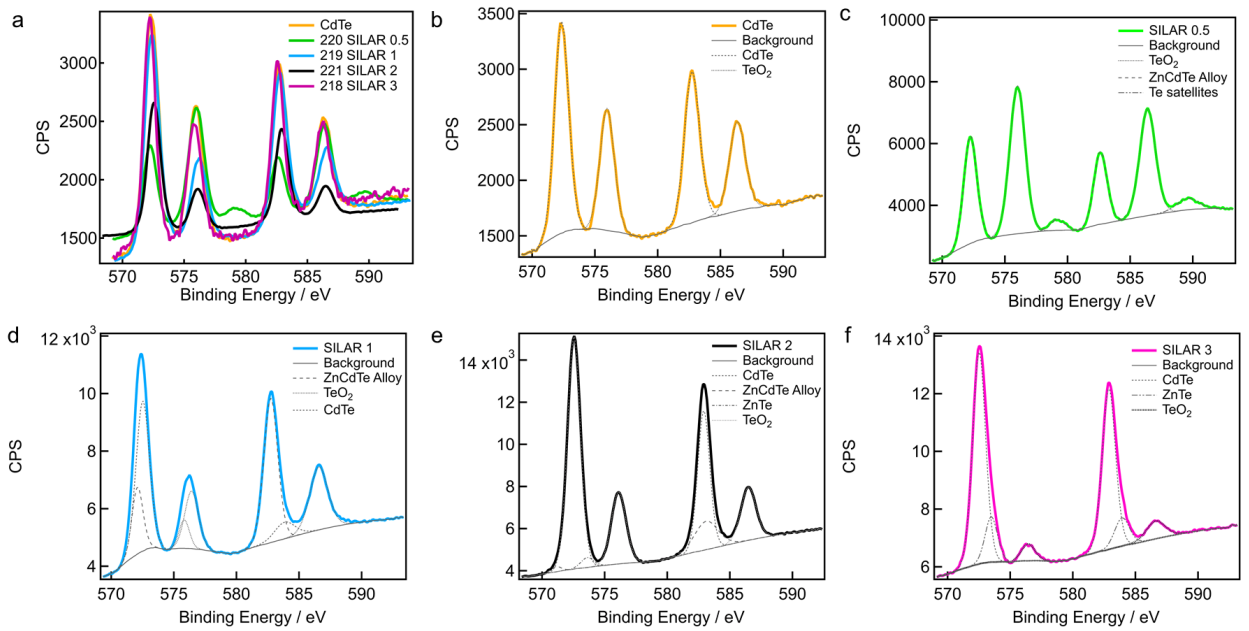

Figure 4.7: Te XPS date. (a) All samples plotted and scaled in one graph; (b) CdTe QDs; (c) SILAR 0.5; (d) SILAR 1; (e) SILAR 2; and (f) SILAR 3. The solid gray line is the fit to the background. The long dashed lines are the fits assigned to a ZnCdTe alloy. The medium dashed gray line is the fit of the peaks to CdTe. The short dashed line is the fit to TeO_2. Finally, the dot-dashed line is assigned either to ZnTe or Te satellite peaks. The assignment of the peaks for all these data is likely not correct and have not been verified.

Table 4.4: Te XPS Assignments. The labeling of the peaks for all these data is likely not correct and have not been not verified.

	$3d_{5/2}$						$3d_{3/2}$			
	Alloy	CdTe	ZnTe	TeO_2		Satellites	CdTe	ZnTe	TeO_2	Satellites
CdTe		572.4		576			582.6		586.3	
SILAR 3		572.5	573.5		576.5		582.9	583.9	586.6	
SILAR 2	571.1	572.5	573.6	576.1			582.9	583.1	586.5	
SILAR 1	572.1	572.5		575.8	576.4		582.7	583.9	586.6	588.4
SILAR 0.5		572.2		576		579.2	582.6		586.4	589.6

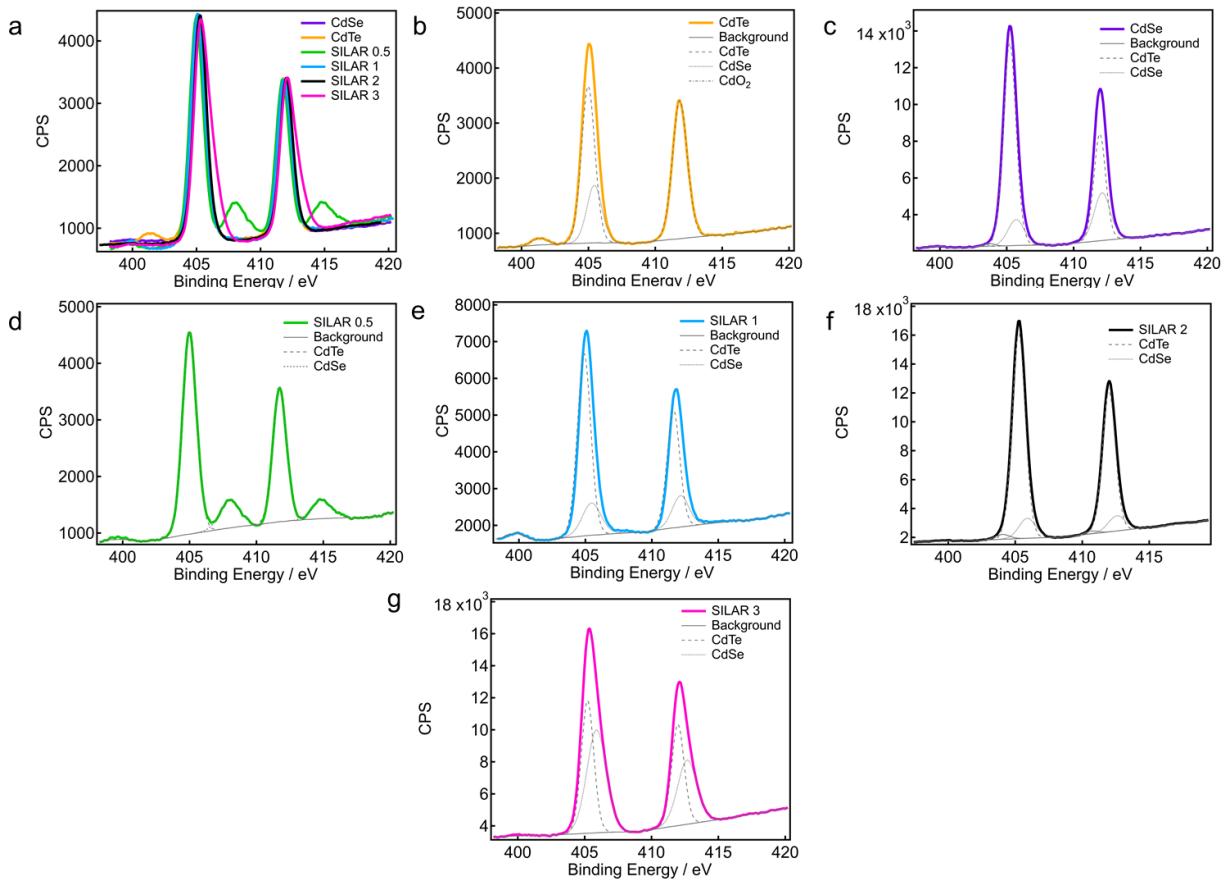

Figure 4.8: Cd XPS Data. (a) All samples plotted and scaled in one graph; (b) CdTe QDs; (c) CdSe QDs; (d) SILAR 0.5; (e) SILAR 1; (f) SILAR 2; and (g) SILAR 3. The solid gray line is the fit to the background. The long dashed gray is the fit of the peaks to CdTe. The short dashed is the fit to CdSe, and the dot-dashed line is the fit to CdO_2. The assignment of the peaks for all these data is likely not correct and have not been verified.

Table 4.5: Cd XPS Assignments. The labeling of the peaks for all these data is likely not correct and have not been not verified.

	$3d_{5/2}$					$3d_{3/2}$			
	CdO_2	CdTe	CdSe	Cd-O	Satellites	CdTe	CdSe	Cd-O	Satellites
CdTe		405.0		405.4		411.8			
CdSe		405.2	405.4				412	412.1	
SILAR 3		405.2	405.9				412	412.7	
SILAR 2	404	405.3	405.9			410.7	412	412.6	
SILAR 1	403.7	405.2	405.7			411.8	412.2	412.1	
SILAR 0.5		405			408	411.7			414.9

4.2 First-shell global fit EXAFS

Based on the short-comings of the characterization techniques outlined in the previous sections, it is clear that conventional materials characterization tools cannot be used to unambiguously determine the internal atomic-scale nanoparticle structure. We therefore used X-ray absorption spectroscopy as an element-specific and structurally sensitive probe. We measured the XAS spectra at the K-edges of all four elements (Zn, Se, Te, Cd) in the CSQD nanoparticles of the SILAR 2 sample. Here, we focus on the EXAFS spectra $\backsim$100-1600 eV above the ionization edges. A detailed analysis of the XANES spectra will be provided in Chapter 5. The absorption cross section modulations in this spectral region can phenomenologically be interpreted as resulting from the interference of outgoing and backscattered photoelectron waves emanating from the X-ray absorbing atom. As such, the EXAFS spectrum is particularly sensitive to the local structure (bond lengths and symmetry) and coordination numbers. We extracted the EXAFS by normalization and background subtraction (see Figures 4.9-4.12 below), after which the fine structure is multiplied by k^n (n=3 in Figures 4.9-4.12). Finally, the k-space data is Fourier transformed to yield the effective RDF. The effective RDFs, shown in Figure 4.13, exhibit only one dominant peak at each absorption edge, which indicates that in these materials EXAFS is only sensitive to the nearest-neighbor cation-anion distances. While there are several examples in the literature of EXAFS fitting of higher coordination shells in nanoparticles,[55,59,178–180] many of those measurements were done at cryogenic temperatures. There could be several reasons that higher shells are not seen in the EAXFS data: (1) The measurements taken in solution at room temperature, which means that the thermal contribution to the Debye-Waller factor is relatively large; (2) The nanoparticles have a high amount of disorder[181] and/or strain[175] and a high surface to volume ratio. The whole set of EXAFS data was therefore analyzed with a first-shell Fourier approach with the bond length change, ΔR, mean-square disorder parameter, σ^2 (describing thermal and static disorder), coordination number, N, and ionization energy, E_0, as fitting

parameters (see Section 4.6.1 for details on the fit).

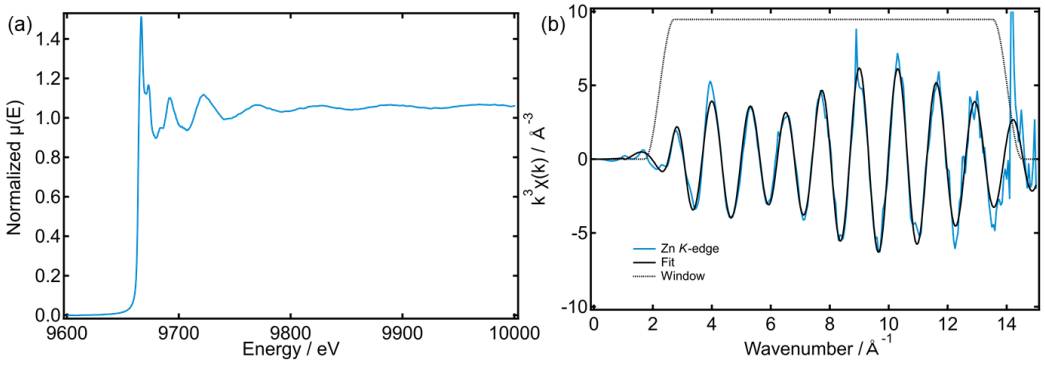

Figure 4.9: (a) Normalized Zn K-edge X-ray absorption spectrum of $Cd_xZn_{1-x}Te$/CdSe core/shell nanoparticles (SILAR 2, $x = 0.8$). (b) Blue spectrum is the processed k-space data (weighted by k^3) and the black spectrum is the fit of the data to the zinc blende ZnTe crystal structure.

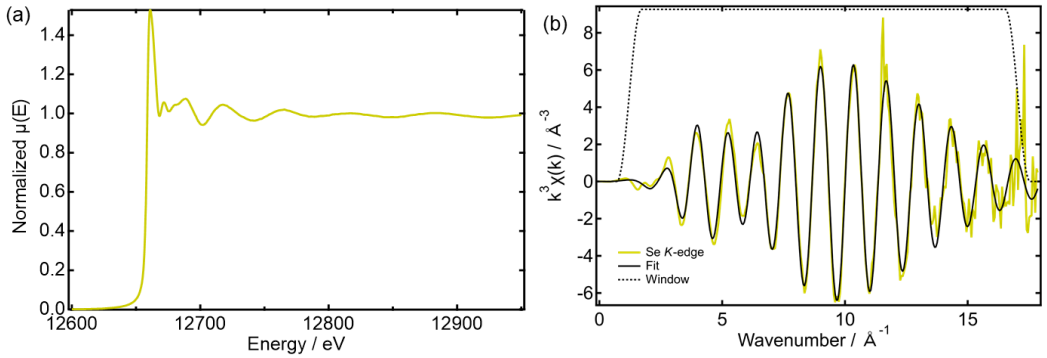

Figure 4.10: (a) Normalized Se K-edge X-ray absorption spectrum of $Cd_xZn_{1-x}Te$/CdSe core/shell nanoparticles (SILAR 2, $x = 0.8$). (b) Yellow spectrum is the processed k-space data (weighted by k^3) and the black spectrum is the fit of the data to the zinc blende CdSe crystal structure.

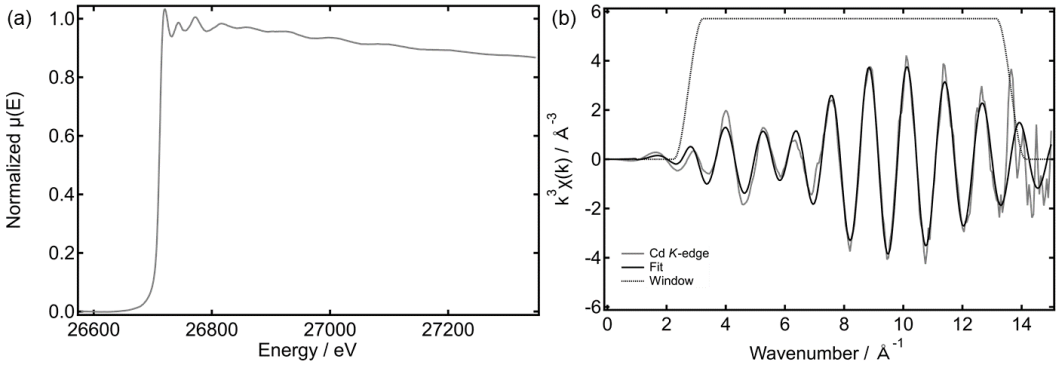

Figure 4.11: (a) Normalized Cd K-edge X-ray absorption spectrum of $Cd_xZn_{1-x}Te$/CdSe core/shell nanoparticles (SILAR 2, $x = 0.8$). (b) Gray spectrum is the processed k-space data (weighted by k^3) and the black spectrum is the fit of the data to the zinc blende CdSe and CdTe crystal structures.

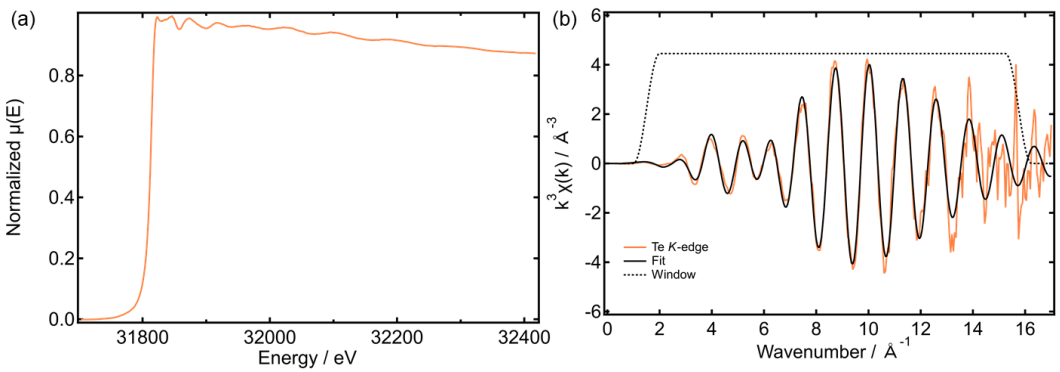

Figure 4.12: (a) Normalized Te K-edge X-ray absorption spectrum of $Cd_xZn_{1-x}Te$/CdSe core/shell nanoparticles (SILAR 2, $x = 0.8$). (b) Dark orange spectrum is the processed k-space data (weighted by k^3) and the black spectrum is the fit of the data to the zinc blende CdTe and ZnTe crystal structures.

We tested two models by globally fitting the four data sets in Figure 4.13. In the first model, each RDF is fit to a pure-phase zinc blende structure, that is, ZnTe at the Zn and Te edges, and CdSe at the Cd and Se edges. This case applies for ZnTe/CdSe core/shell QDs with a relatively sharp interface (negligible alloying). As shown in the Supplementary material, this model did not yield satisfactory fit results. The second model includes the CdTe zinc blende structure in the fit at the Cd and Te edges, the relative stoichiometric contribution of which is fit using weight parameters x (Cd edge) and y (Te edge) ($0 \leq x$,y ≤ 1) as global fitting parameters. The resulting fits were significantly improved and show excellent agreement with the data as shown in Figure 4.13 (see Supplementary material for the comparison of the fit statistics). We note that the Zn and Se edge data can be perfectly fit with pure-phase ZnTe and CdSe structures, respectively.

Table 4.6 summarizes the EXAFS fitting results for the SILAR 2 CSQD sample, as well as for pure-phase CdTe and CdSe QDs. The fitted changes in first-shell bond lengths, ΔR, indicate a slight expansion of the Zn-Te bonds and a contraction of the Cd-Te bonds compared to the bulk and nanophase bond lengths. This finding indicates alloying of, and/or epitaxial strain between, the ZnTe and CdTe zinc blende structures, which have very different lattice parameters.[146] The Cd-Se bonds in the CSQDs are contracted with respect to the bulk but expanded compared to CdSe QDs. Since we expect CdSe to cover the surface of the

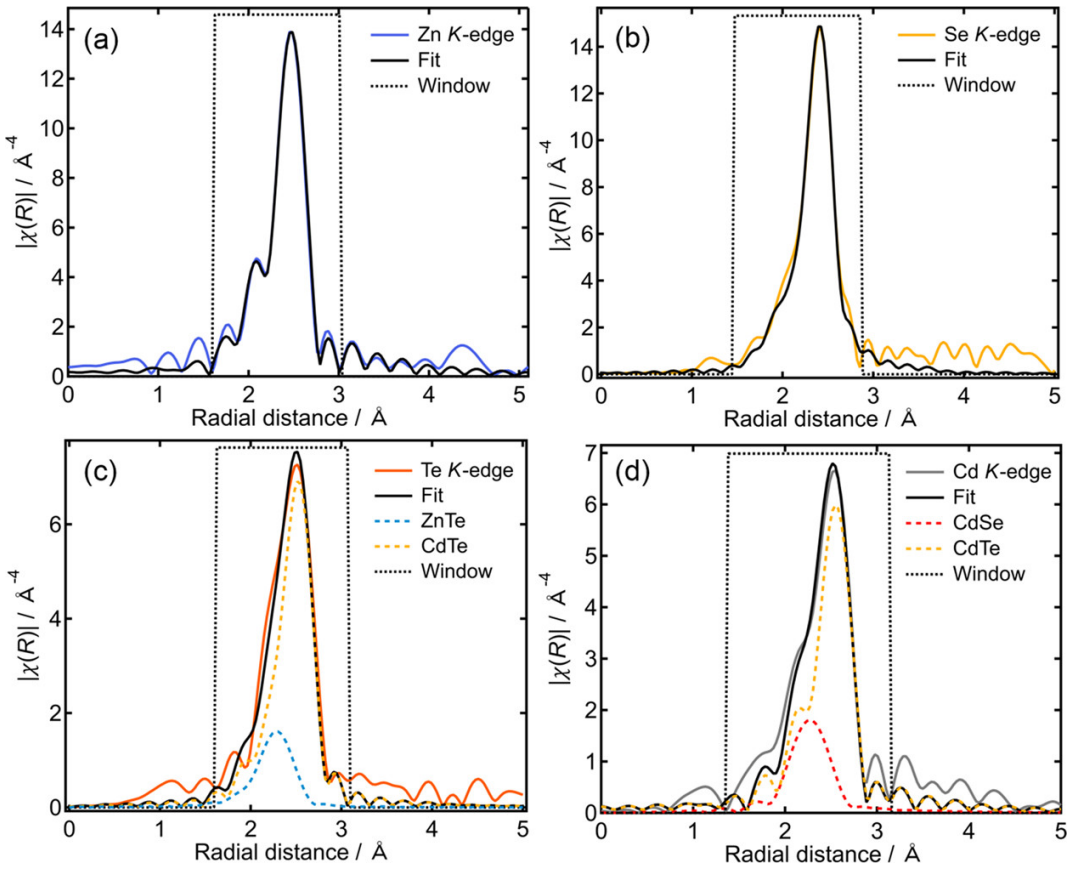

Figure 4.13: Fourier transformed EXAFS data of SILAR 2 CSQDs. (a) Zn K-edge data (blue) and fit to the ZnTe zinc blende structure (black). (b) Se K-edge data (yellow) and fit to the CdSe zinc blende structure (black). (c) Te K-edge data (dark orange), fit to the ZnTe and CdTe zinc blende structures (black), and individual first-shell contributions of ZnTe (20%, blue) and CdTe (80%, yellow). (d) Cd K-edge data (gray), fit to the CdSe and CdTe zinc blende structures (black), and individual first-shell contributions of CdSe (22%, red) and CdTe (78%, yellow). The k-space EXAFS data χ(k) were weighted by k^3 before Fourier transformation and the R-space axes are not phase-corrected. The fitting ranges in R-space are shown as dashed black window functions in each graph.

CSQDs, the effects of strain and ligands on the Cd-Se bonds are hard to predict. Due to the uncertainty of surface effects, no conclusions can be drawn. The fact that the mean-square disorder parameters, σ^2, are all similar, regardless of the sample, evidences that the static disorder in the CSQDs is not larger than in pure-phase QDs. The weight parameters x and y are globally fit to $x = 0.78 \pm 0.04$ (Cd-Te contribution at the Cd edge) and $y = 0.80 \pm 0.07$ (Cd-Te contribution at the Te edge), which are in excellent agreement with results from ICP-OES (see Table 4.1).

Table 4.6: EXAFS fitting results at the Zn, Se, Te, and Cd K-edges. ΔR is the bond length change relative to the bulk (R_{Bulk}, σ^2 is the mean-square disorder of neighboring distances (Debye-Waller parameter), x is the fraction of Cd-Te bonds at the Cd edge, and y is the fraction of Cd-Te bonds at the Te-edge. All four data sets for the CSQDs were fit simultaneously and the ΔR and σ^2 parameters for the same bonds were set equal. The X-ray absorbing atom is denoted in bold typeface and written first.

Bond	ΔR	R_{Bulk}(Å)[146]	σ^2	**Weight**
CSQDs (SILAR 2)				
Zn-Te	0.009 ± 0.006	2.643	0.0065 ± 0.0007	–
Se-Cd	-0.011 ± 0.005	2.631	0.0057 ± 0.0006	–
Te-Zn	0.009 ± 0.006	2.643	0.0065 ± 0.0007	0.20 ± 0.07 (1-y)
Te-Cd	-0.019 ± 0.005	2.806	0.0064 ± 0.0006	0.80 ± 0.07 (y)
Se-Cd	-0.011 ± 0.005	2.631	0.0057 ± 0.0006	0.22 ± 0.04 (1-x)
Cd-Te	-0.019 ± 0.005	2.806	0.0064 ± 0.0006	0.78 ± 0.04 (x)
CdTe QDs (6.3 ± 0.5 nm)				
Te-Cd	-0.012 ± 0.003	2.806	0.0069 ± 0.0003	–
Cd-Te	-0.012 ± 0.003	2.806	0.0069 ± 0.0003	–
CdSe QDs (3.4 ± 0.3 nm)				
Se-Cd	-0.020 ± 0.005	2.631	0.0058 ± 0.0005	–
Cd-Se	-0.020 ± 0.005	2.631	0.0058 ± 0.0005	–

The EXAFS global fit analysis clearly shows that the CSQD particles do not exhibit a simple ZnTe/CdSe core/shell structure. Instead, they contain a significant fraction of Cd-Te bonds. The exact nature of the Cd-Te bonds, whether they are contained in a pure-phase CdTe intermediate shell or as a $Cd_xZn_{1-x}Te$ alloy, cannot be ascertained from the data, since our Fourier analysis is restricted to the first-shell only. In fact, it is well known that bond distances in substitutional ternary alloys derived from EXAFS are much closer to pure-phase bond lengths than those that could be derived using Vegard's law and XRD data.[147] On the other hand, the fact that the Zn and Se edge data can be perfectly described with pure-phase ZnTe and CdSe zinc blende structures, respectively, without the need to include much shorter Zn-Se bonds (2.42 Å in the bulk[146]), evidently shows that no anion alloying of the ZnTe core or cation alloying of the CdSe shell take place. Therefore, within our experimental uncertainties, we can exclude the presence of $ZnTe_xSe_{1-x}$, $Cd_xZn_{1-x}Se$, or a homogeneous alloy $Cd_xZn_yTe_zSe_{x+y-z}$.

Comparison with EXAFS results: To compare the bond weights obtained from EXAFS (x for the Cd-Te bond weight at the Cd edge and y for the Cd-Te bond weight at the Te edge) with the elemental fractions from ICP (Table 4.1), we distribute the fractions as follows (SILAR 2 sample): Zn:Te=1.0:0.9 for the Zn-Te bonds, Cd:Te=4.5:4.3 for the Cd-Te bonds, and Cd:Se=1.5:1.4 for the Cd-Se bonds. The reason for choosing Zn:Te=1.0:0.9 is based on the relative low Te content in the ZnTe cores and SILAR 0.5 sample. The bond fractions at the respective edges can then be estimated as follows: the fraction of Zn-Te bonds at the Te edge is (0.9±0.2)/(5.2±0.4)=0.17±0.04, and the fraction of Cd-Se bonds at the Cd edge is (1.4±0.4)/(6.0±1.0)=0.23±0.08. These fractions are in good agreement with the weighting parameters obtained from the EXAFS fit, as shown in Table 4.7 below. If the cation to anion ratio is assumed to be 1:1, the elemental fractions from ICP bond are still within the error of bond weights obtained from EXAFS.

Table 4.7: Comparison between weighting parameters obtained from EXAFS fitting and ICP analysis. y denotes the fraction of Cd-Te bonds at the Te edge, and x denotes the fraction of Cd-Te bonds at the Cd edge.

Bond	EXAFS Wt.	ICP Wt.
Te K-edge		
Te-Zn	1-y = 0.20 ± 0.07	0.17 ± 0.04
Te-Cd	y = 0.80 ± 0.07	0.83 ± 0.01
Cd K-edge		
Cd-Se	1-x = 0.22 ± 0.04	0.23 ± 0.08
Cd-Te	F = 0.78 ± 0.04	0.77 ± 0.08

,

4.3 Particle models and control experiments

Based on the EXAFS analysis, we propose two candidate particle heterostructure models: (I) core/shell/shell ZnTe/CdTe/CdSe; and (II) alloyed core/shell $Cd_xZn_{1-x}Te$/CdSe. For simplicity, we assume that the nanoparticles are perfectly spherical and that the interfaces between core and shells are sharp. For each SILAR sample we determined the particle

diameters and elemental ratios, as summarized in Figure 4.14 and Table 4.1. The number of atoms in the particle core or shell(s) can then be expressed as a function of the radii and the lattice constants (see Chapter 3 Section 3.3 for equations). Since the particle outer radius is determined by TEM sizing (Section 4.1.3), and the Te:Zn and Cd:Se elemental ratios are obtained from elemental analysis (Section 4.1.4), we can determine the nanoparticle inner radii, in other words, the core radius and interlayer thickness for Model I and the alloyed core radius for Model II, that best fit the data. The results are schematically shown in Figure 4.15a and b for the SILAR 2 sample. A third model (Model III) is included to demonstrate the effect of gradient alloying. For this model, particle model equations (see Chapter 3 Section 3.3.3) become increasingly complex. Later, when we calculate the band alignment for the different models (Table 4.8), we find that alloying does not have a strong effect on the overlap of the $1S_h$ and $1S_e$ states. Due to the lack of influence of alloying we will emphasize the difference between Model I and Model II.

We first note that the SILAR 0.5 sample, which is synthesized by exposing ZnTe cores to

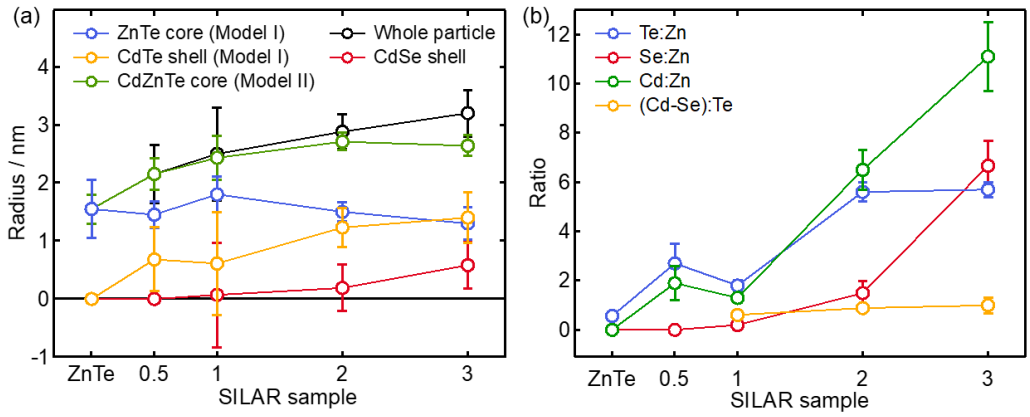

Figure 4.14: Results from TEM and elemental analysis. (a) Nanoparticle radii ratios for the ZnTe seeds, SILAR 0.5, 1, 2, and 3 samples. In the case of Model I, the radii of the pure-phase ZnTe core and CdTe intermediate shell are plotted. In the case of Model II, the radius of the alloyed CdZnTe core is plotted. The CdSe shell radius applies to both models. Error bars on the black data originate from TEM sizing, error bars on the red and blue data are propagated errors using a Monte Carlo procedure described in Chapter 3 Section 3.3.4. (b) Elemental ratios for the ZnTe seeds, SILAR 0.5, 1, 2, and 3 samples. The abscissae are proportional to time (from 0 for ZnTe to 60 min for SILAR 3). All error bars represent ± std. dev.

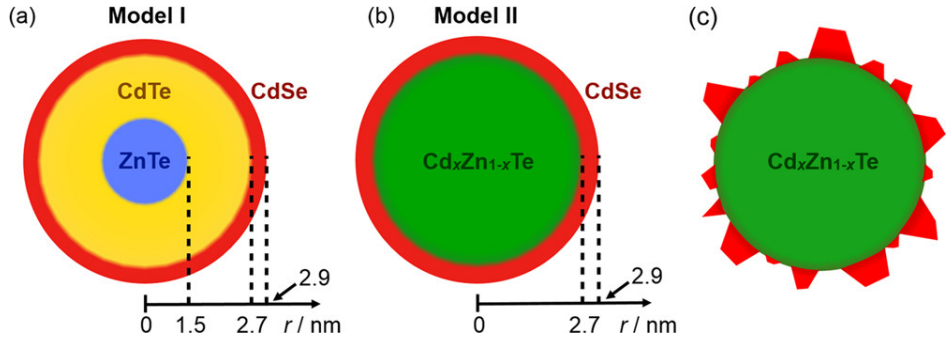

Figure 4.15: Nanoparticle models obtained from EXAFS, TEM, and elemental analysis. (a) Core/shell/shell ZnTe/CdTe/CdSe Model I for the SILAR 2 sample. (b) Alloyed core/shell $Cd_xZn_{1-x}Te$/CdSe Model II for the SILAR 2 sample ($x = 0.8 \pm 0.1$). The CdSe shell thickness is exaggerated and not to scale. In addition, the CdSe shell is shown to be uniform, which is not in agreement with TEM and EXAFS data. Instead, the CdSe shell is patchy, as schematically shown in (c).

the Cd precursor only (see Chapter 3 Section 3.1.2), already contains a significant amount of Cd-Te bonds, either in the form of a pure-phase shell (Model I), or incorporated in a $Cd_xZn_{1-x}Te$ alloy (Model II). In fact, the nanoparticle diameter increases from 3.1 ± 0.5 nm for the ZnTe seeds, to 4.3 ± 0.5 nm for the SILAR 0.5 sample, which indicates that the Cd not just adsorbs onto, or diffuses into, the ZnTe cores, but rather new bonds are formed due to the unintended reaction of Cd and Te precursors. The latter are still in the solution since the ZnTe core synthesis is not quantitative, as is confirmed by a control experiment showing that ZnTe seeds continue to grow until 20 min after precursor injection at 240 °C (Figure 4.16). It is noted, however, that previously reported synthesis procedures, that are similar to ours, do assume that the ZnTe seed formation is quantitative.[36,38–40,43] Interestingly, the UV/vis absorption also significantly shifts to longer wavelengths upon addition of Cd precursor only (Figure 4.17), an effect that could either be interpreted as the formation of a (quasi-)type-II heterostructure (e.g. ZnTe/CdTe), or the formation of a $Cd_xZn_{1-x}Te$ alloy.

Zn^{2+} for Cd^{2+} cation exchange is expected to play a major role under the present reaction conditions (240 °C, 3-60 min), as demonstrated in a recent study on ZnTe nanorods by Enright *et al.*[42] The core/shell/shell Model I with sharp interfaces is therefore highly unlikely. In fact, this model predicts a slight decrease in the ZnTe core size as a function

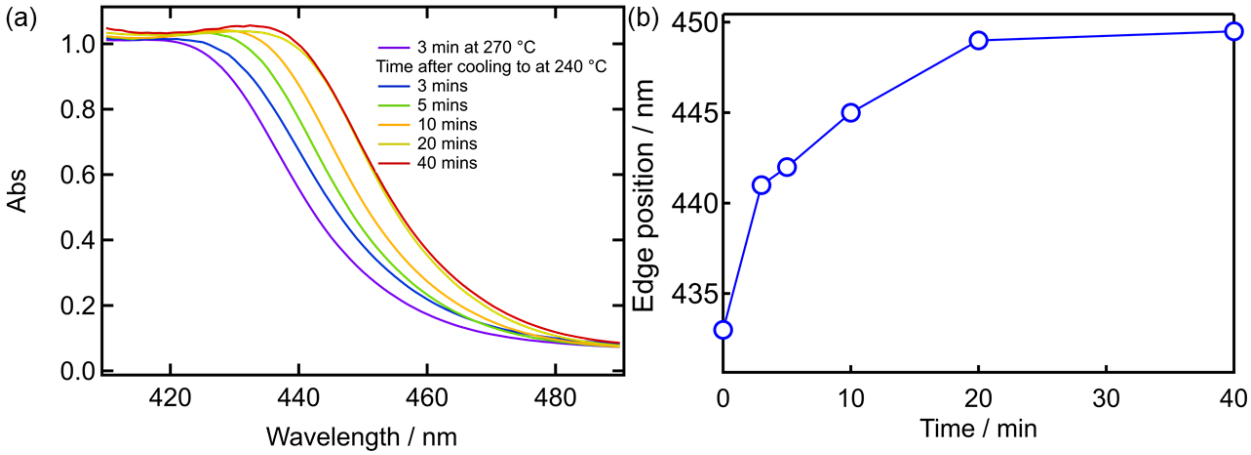

Figure 4.16: (a) UV/vis absorption spectra of ZnTe cores after 3 min at 270 °C, and after 3, 5, 10, 20, and 40 min at 240 °C. (b) Plot of the position of the first-derivative minimum of the data in A as a function of time. ZnTe core growth subsides after ∽20 min.

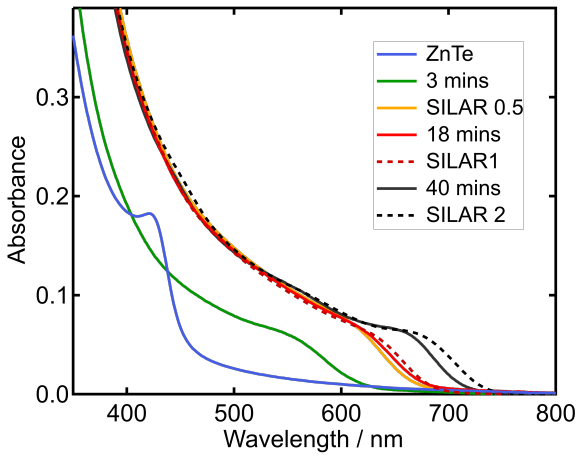

Figure 4.17: UV/vis spectra of pure-phase ZnTe cores (270 °C) and ZnTe cores that were cooled down to 240 °C and then exposed to 2.3 mL of a 0.1 M Cd-oleate solution. Aliquots were taken at 3, 10 (SILAR 0.5), and 18 min after the first Cd-oleate injection. An additional 2.9 mL of Cd precursor solution was added after 20 min and an aliquot was taken after a total of 40 min in order to simulate the conditions of the SILAR 2 synthesis (but without Se addition). SILAR 1 and SILAR 2 data are also shown for comparison.

of SILAR cycle (Figure 4.14a), which is unrealistic given that the pure-phase CdTe shell would inhibit Zn^{2+} ion diffusion out of the core without the concomitant formation of an alloy across the ZnTe/CdTe interface. We therefore propose Model II to be the most realistic for heterostructures synthesized according to the SILAR procedures reported in the

literature.[36,38–40,43]

The cation exchange reaction is expected to occur via a kick-out mechanism with a relatively small activation barrier of 24 kJ/mol,[27,42] where Cd^{2+} ions, or [Cd-Te] monomers, first saturate the ZnTe surface before they diffuse into the lattice through unoccupied tetrahedral interstitial sites.[143] Zn^{2+} ions can diffuse through interstitial sites outwards before they readily combine with either HDA or oleate ions in solution.[41] In the present case, however, cation exchange coincides with the formation of new Cd-Te bonds through the reaction of Cd and Te precursors. The relatively small loss of Zn atoms inside the QDs over the course of the SILAR 0.5-3 reactions, as shown by the only slight decrease of ZnTe core size in Model I (Figure 4.14a), and the rather constant (Cd-Se):Te ratio (Figure 4.14b), indicate that the rate of CdTe formation is higher than, or at least comparable to, the rate of Zn^{2+} ion diffusion out of the lattice. The particles during the early SILAR cycles (0.5-1) may therefore be better described as a gradient alloy, with a Zn-rich core and a Cd-rich shell – their growth can be entirely attributed to the formation of new Cd-Te bonds. Indeed, hardly any CdSe is present for the SILAR 1 sample, which agrees with the lack of Se incorporation in the studies on ZnTe nanorods by Enright *et al.*[42] and the higher reactivity of elemental Te than elemental Se toward Cd.[182] During later SILAR cycles (2, 3), particle growth is largely due to the formation of a CdSe shell (Figure 4.14a).

4.3.1 Cation diffusion simulations

Cation diffusion calculations were done using the theory described in Jiang, *et al.*[38] where the authors experimentally measured the cation diffusion rate to be $1.3\text{x}10^2$ nm^2/min. These cation diffusion simulations show that a nearly homogeneous $Cd_xZn_{1-x}Te$ core is formed on the time scales of SILAR cycles 2 and 3 (see Figure 4.18 c and d). In contrast, the formation of a homogeneous alloy is less definitive for SILAR 0.5 and SILAR 1 (Figure 4.18 a and b) and it could be possible that the core is more of a graded $Cd_xZn_{1-x}Te$ alloy. These studies are not meant to be quantitative and do not take in account all the complexity of

the mechanisms of particle growth happening concurrently with cation diffusion. However, these studies help to paint a qualitative picture and corroborate the experimental analysis presented so far. A similar ion diffusion study based on the annealing of ZnTe/CdSe QDs at 250 °C[38] proposed the concomitant formation of a $Cd_xZn_{1-x}Se$ alloy, which can be clearly discarded on the basis of our EXAFS results (*vide supra*).

To investigate the role of TOP-Se, a synthesis was performed in the absence of Se precursors (see Chapter 3), while keeping the Cd addition rates and other reaction conditions

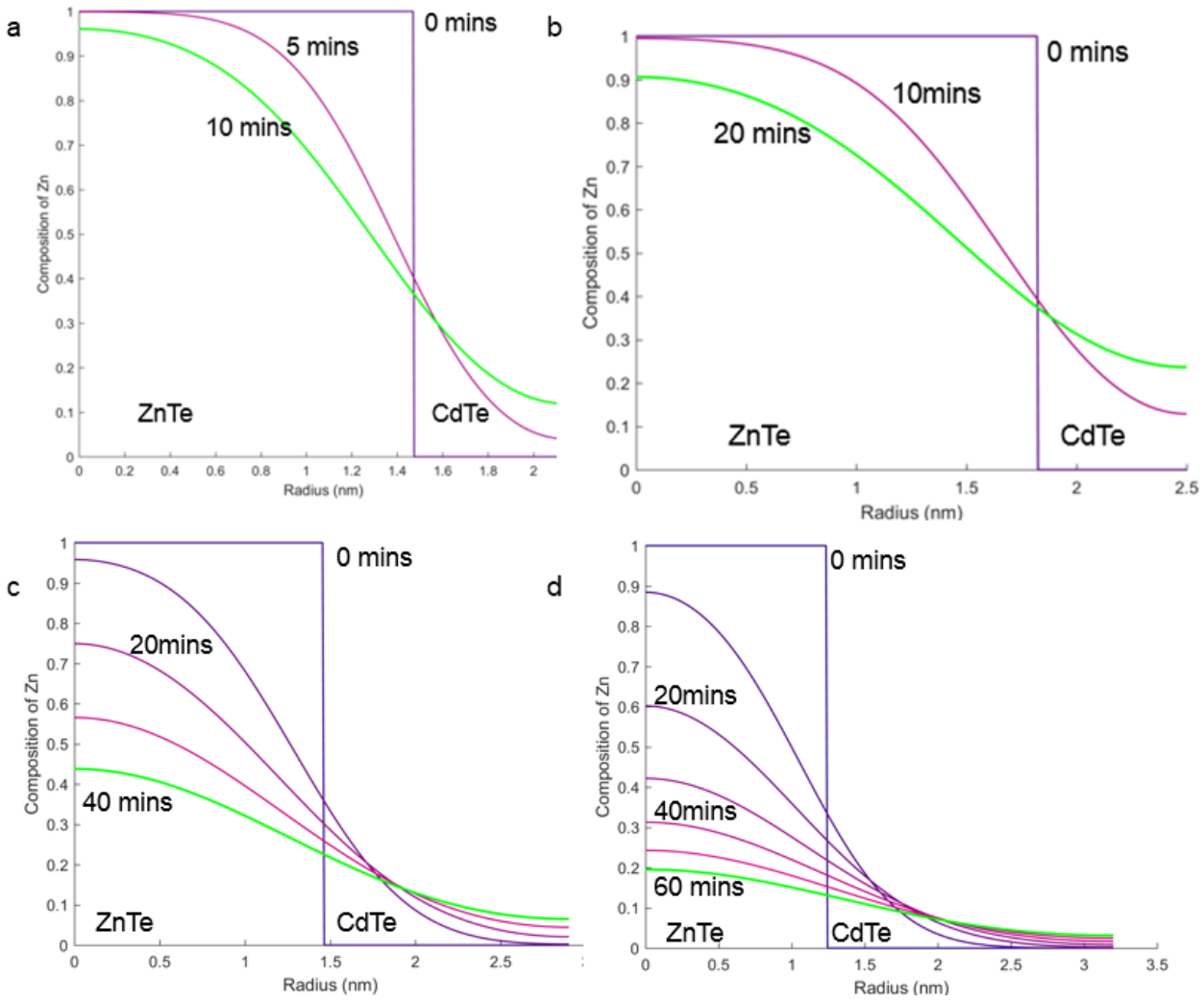

Figure 4.18: Cation diffusion profiles for each sample over the respective reaction times: (a) The SILAR 0.5 particle over the 10 min reaction time. Each line represents a 5 min time point. The SILAR 1 (b), SILAR 2 (c) and SILAR 3 (d) particles over the 20, 40 and 60 min reaction time, respectively. Each line represents a 10 min time point.

unchanged. Aliquots were taken at 3, 5, 10 (SILAR 0.5), 18, and 40 min to record UV/vis spectra, shown in Figure 4.17 together with the spectra of the SILAR 1 and 2 samples. The absorption onset continuously shifts to longer wavelengths which is attributed to CdTe addition and alloying during SILAR cycles 0.5 and 1, and due to alloying and CdSe shell growth during SILAR cycles 2 and 3. By comparing the spectra at 18 and 40 min for the Cd-only reaction with the SILAR 1 and 2 spectra, it is seen that the CdSe shell influences the spectrum only minimally and that the absorption onsets remain relatively abrupt. As we will show below, this behavior indicates a direct band-gap transition (as opposed to a spatially indirect type-II transition).

The particle models based on TEM sizing and elemental analysis assume that CdSe is added uniformly to the $Cd_xZn_{1-x}Te$ core. Under this assumption, the CdSe shell is only half a monolayer (ML) for the SILAR 2 sample and 2 ML for the SILAR 3 sample (1 ML $\backsim$ 0.3 nm). Such extremely thin epitaxial shells would be subject to a significant degree of strain due to the relatively large lattice mismatch of 5-6%[146] between CdTe (or alloyed $Cd_{0.8}Zn_{0.2}Te$) and CdSe. Such effects are not seen in the EXAFS data at the Se K-edge, that is to say, the latter can be perfectly fit with the CdSe zinc blende structure with only minor (0.4%) deviations from the bulk structure (Table 4.6). Based on these results, we propose the presence of pure-phase CdSe islands on the alloyed CdZnTe core, which would minimize the interfacial strain (Figure 4.15c). In fact, Jiang *et al.* have indirectly derived that the CdSe shell must be rough by measuring the inhomogeneity in interfacial hole transfer rates to an adsorbed hole acceptor.[38,43] They concluded that CdSe shell formation proceeds via a Stranski-Krastanov growth mechanism at moderate temperatures with the formation of a uniformly strained film (the wetting layer) up to the critical thickness of several MLs, followed by the growth of three-dimensional islands on top of the uniform film. Our EXAFS results clearly disagree with the presence of a uniform, strained CdSe layer, especially since the amount of deposited CdSe is only minimal (Figure 4.15b). We therefore conclude that under the present SILAR synthesis conditions CdSe island growth occurs via the Volmer-

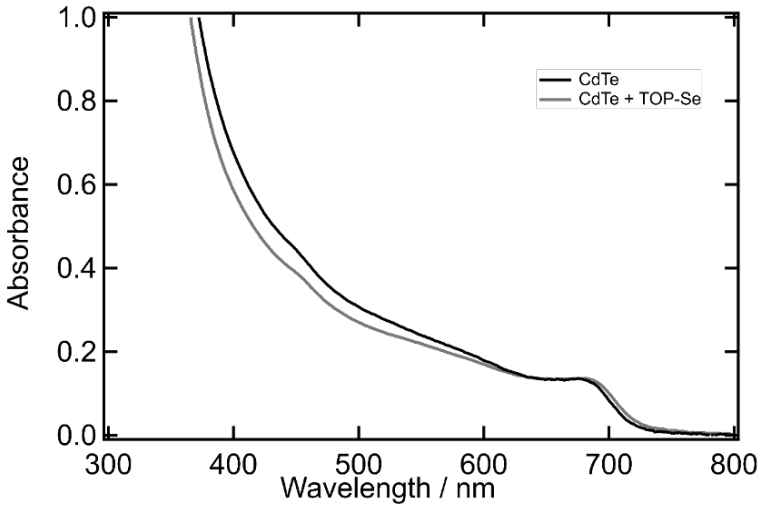

Figure 4.19: UV/vis of a CdTe (6.3 ± 0.5 nm) before (black) and after (gray) anion exchange control experiment.

Weber mechanism, which is dominant for interfaces with large lattice mismatch where the energetic cost of lattice strain exceeds that of the increased surface area associated with the islands.[36,183] The roughness of the CdSe shell is corroborated by the "patchiness" of the HAADF-STEM images of the SILAR 2 sample (Figure 4.4). We also note that we can exclude the occurrence of an anion alloy $CdTe_xSe_{1-x}$ on the basis of a control experiment (see Chapter 3 Section 3.1.5) in which purified CdTe QDs are exposed to TOP-Se precursor at 240 °C for 40 min. No changes in the UV/vis spectrum and ICP-OES were observed (see Figure 4.19), which is in agreement with the high activation barrier for anion exchange in similar systems.[50,143]

4.4 Wave function engineering approach for band alignment and wave function overlap

With the internal structure of the CSQDs determined as $Cd_xZn_{1-x}Te/CdSe$ using EXAFS, TEM, and elemental analysis, we then applied a simple wave function engineering approach[150] (see Chapter 3 Section 3.5) to determine the band alignment regime and electron-

hole wave function overlap for the lowest-energy $1S_{hh}$ (heavy hole) and $1S_e$ (electron) states. In this method, an effective mass approximation was made to simplify the atomic-scale variation of potentials. The hole and electron were assumed to move freely in averaged valence-band and conduction-band potentials respectively, with certain effective masses (see Chapter 3 Section 3.5). As a result, both charge carriers can be treated by a simple particle-in-a-sphere model. The Schrödinger equations of both particles were solved using the finite difference method. A mean-field approximation was applied to account for the Coulomb interaction between electron and hole (exciton binding energy), meaning that the electron moves in a mean potential induced by the hole Φ_h and the hole moves in a mean potential of the electron Φ_e. These potentials cannot be determined beforehand but can be calculated by Poisson equations if the electron and hole wavefunctions were known. As a result, a self-consistent computation of wavefunctions and band energies was applied.

To understand the influence of alloying on the band alignment, we performed calculations

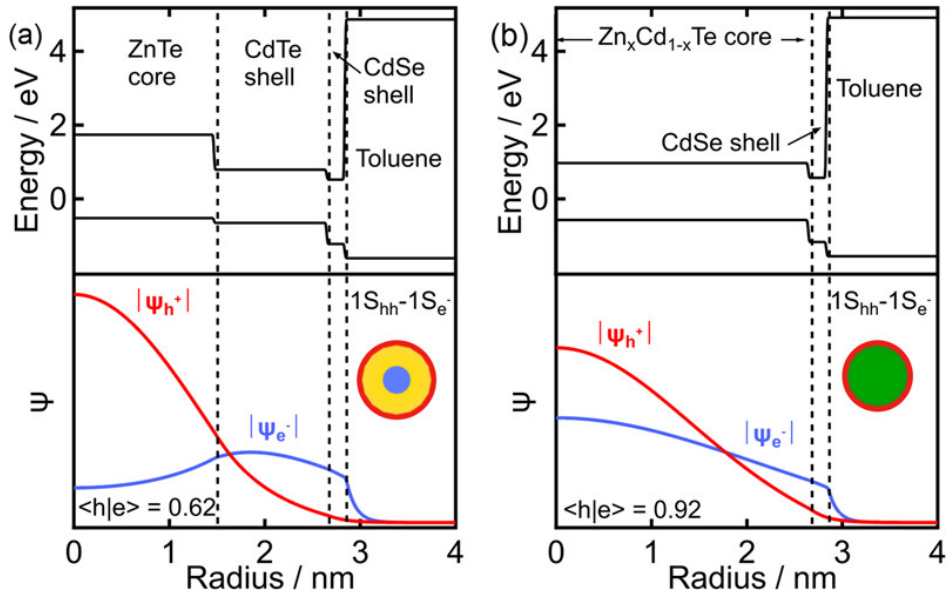

Figure 4.20: Band alignment calculations and wave function overlap. **Top:** The stair-shaped black lines show the confinement potentials of the valence and conduction bands (bulk values[146]). Bottom: The electron (blue) and hole (red) wave functions (Ψ) in the $1S_{hh}$ and $1S_e$ states for (a) the ZnTe/CdTe/CdSe core/shell/shell Model I, and (b) the alloyed $Cd_xZn_{1-x}Te$ core/CdSe shell Model II. The radii for the cores and shells are those obtained from combining the TEM and elemental analysis results for the SILAR 2 sample ($x = 0.8 \pm 0.1$). The surrounding solvent is toluene. <h|e> denotes electron-hole wave function overlap.

Table 4.8: The wavefunction overlap between $1S_h$ and $1S_e$ states and the simulated transition wavelength between them, for SILAR 2 QD calculated using different models.

	$1S_h$-$1S_e$ overlap	$1S_h$-$1S_e$transition wavelength (nm)
Model 1: ZnTe/CdTe/CdSe	0.62	746
Model 2: $Zn_{0.17}Cd_{0.83}Te$ /CdSe	0.91	742
Model 3: linear ZnTe+CdTe/CdSe	0.85	737
Model 3: linear ZnTe+CdTe/$CdSe_{0.50}Te_{0.50}$	0.82	749

for both the core/shell/shell Model I and the alloyed core/shell Model II, using the particle radii for the SILAR 2 sample (Figure 4.20). For simplicity, we neglect the fact that CdSe is present in the form of islands instead of a uniform layer, which does not significantly affect the conclusions drawn herein. While Model I nanoparticles retain a quasi-type-II band alignment for which the hole wave function spreads over the ZnTe/CdTe core/shell portion and the electron localizes inside the CdTe shell, resulting in a $1S_e$-$1S_{hh}$ electron-hole overlap of $\backsim$0.6, the alloyed core Model II nanoparticles act as a single-composition material with a much larger 1Se-1Shh electron-hole overlap of $\backsim$0.9, similar to type-I CSQDs.[12] The electron-hole wave function overlap is related to the oscillator strength in the UV/vis absorption spectrum. Since we see a rather pronounced $1S_e$-$1S_h$ exciton transition for all samples, except maybe SILAR 3 for which there is a weak low-energy tail, this finding indicates a direct band-gap transition, as opposed to a spatially indirect lowest-energy band gap transition for a type-II alignment. The thin CdSe shell of 0.2 nm has expectedly only a minimal influence on the wave function overlap, which is confirmed by the relatively small red shift of the first-exciton absorption onset in the UV/vis spectra upon CdSe incorporation (Figure 4.17). Our simulations (Table 4.8) indicate that a CdSe shell thickness of 1.36 nm is necessary to achieve a type-II alignment and a $1S_e$-$1S_h$ electron-hole overlap of $\backsim$0.5 for the $Cd_xZn_{1-x}Te$/CdSe CSQDs ($x = 0.8 \pm 0.1$, SILAR 2). In Table 4.8, we show that gradient alloying of the core instead of homogeneously alloying only marginally changes the band alignment, wave function overlap, and calculated transition energies.

The large electron-hole wave function overlap for the $Cd_xZn_{1-x}Te$/CdSe CSQDs raises the question about their emission properties. We measured the PL yield and decay time and obtained <0.1% and ∽10 ± 0.1 ns (mean decay time, see Figure 4.1) for the SILAR 2 sample, respectively. These values show that the electron-hole recombination is dominated by non-radiative decay channels such as surface trap states. For the SILAR 2 sample the latter could be dominant since the CdSe coverage is only small and the $Cd_xZn_{1-x}Te$ alloyed core, and therefore hole density, is expected to be largely exposed to the solvent. The SILAR 3 sample has a mean decay time of ∽76 ± 0.8 ns, which might be prolonged relative to the SILAR 2 sample due to a more complete coverage of the surface with CdSe, shielding the hole density away from the surface/solvent, as well as due to a slightly reduced electron-hole wave function overlap in this sample (type-II behavior).

4.5 Conclusions

We have determined the internal structure of II-VI CSQDs using a multimodal characterization approach based on UV/vis, TEM, elemental analysis, and XAS. We show that the intended ZnTe/CdSe CSQDs, that are synthesized using a common one-pot SILAR procedure, are in actuality nanoparticles with an alloyed $Cd_xZn_{1-x}Te$ core and a patchy CdSe shell that essentially behave as one-component QDs with a direct band gap. Cation exchange and the unintended reaction of molecular precursors prevent the formation of a sharp type-II ZnTe/CdSe interface with small lattice mismatch. Instead, the large interfacial strain between CdxZn1-xTe ($x \backsim 0.8$) and pure-phase CdSe leads to the growth of islands on the QD surface. Our results corroborate the challenges associated with the synthesis of Zn/Cd chalcogenide type-II heterostructures due to facile ion exchange, as pointed out previously by Enright *et al.*[42] and Groeneveld *et al.*[41] We note that the assessment of CSQDs on the basis of UV/vis and TEM analysis alone is not sufficient, since alloy formation and particle growth due to unintended precursor reactions can cause similar trends as expected for the formation

of type-II heterostructures. Here, we employ EXAFS spectroscopy as an element-specific technique for the internal structure determination of heterostructured nanomaterials. By simultaneously fitting the local atomic structures at the ionization edges of all four elements in the sample, we were able to propose models for the internal nanoparticle structure that were further scrutinized by TEM and elemental analysis. While our XAS data were obtained at a large-scale synchrotron X-ray facility with specialized infrastructure and limited access, the advent of tunable high-brightness table-top X-ray sources will enable similar studies on heterostructured photovoltaic and photocatalytic nanomaterials with much higher throughput and more experimental flexibility.[184]

4.6 Supplementary material

4.6.1 XAS data fitting details

The following are the output details from the ARTEMIS software for fitting EXAFS data.[124] The number of independent data points is calculated by the methods presented by Stern.[185]

Details of EXAFS fit with ZnTe, CdTe, and CdSe

Independent points : 47

Number of variables : 16

Chi-square : 10689.6897216

Reduced chi-square : 343.7026587

R-factor : 0.0196333

Number of data sets : 4

Zn K-edge: k-range = 2.226 - 14.032; R-range = 1.626 - 3.015

Se K-edge: k-range = 1.214 - 17.036; R-range = 1.462 - 2.871

Te K-edge: k-range = 1.5 - 15.749; R-range = 1.623 - 3.082

Cd K-edge: k-range = 2.738 - 13.640; R-range = 1.362 - 2.871

Guess parameters:

$\Delta E_{Cd} = 3.64046581 \pm 0.66769339$

$\Delta r_{CdSe} = -0.01074910 \pm 0.00508090$

$\sigma^2_{CdSe} = 0.00577355 \pm 0.00060830$

$\Delta r_{CdTe} = -0.01866578 \pm 0.00553170$

$\sigma^2_{CdTe} = 0.00642966 \pm 0.00067189$

SePercent $= 0.21552813 \pm 0.04518425$

$\Delta E_{Te} = 1.20624541 \pm 0.89686063$

$\Delta r_{ZnTe} = 0.00862717 \pm 0.00585983$

$\sigma^2_{ZnTe} = 0.00645992 \pm 0.00069436$

ZnPercent $= 0.19590091 \pm 0.07364011$

$\Delta E_{Se} = 0.87629133 \pm 0.51104674$

$\Delta E_{Zn} = 3.90395096 \pm 0.45565884$

Elemental Coordination Numbers:

$N_{Zn} = 3.65423689 \pm 0.27727127$

$N_{Te} = 4.73560476 \pm 0.62314135$

$N_{Se} = 4.17195498 \pm 0.34681303$

$N_{Cd} = 3.87236315 \pm 0.37439458$

Defined parameters:

$S^2_{0,Cd} = 0.72000000$

TePercent $= 0.78447187$

$S^2_{0,Te} = 0.75000000$

CdPercent $= 0.80409909$ [1-ZnPercent]

$S^2_{0,Se} = 0.73000000$

$S^2_{0,Zn} = 0.92000000$

Details of EXAFS fit with only ZnTe and CdSe

For a ZnTe/CdSe core/shell nanostructure, it is expected that the data could be fit to the ZnTe and CdSe zinc blende crystal structures only. However, while the Zn and Se edge data could indeed be fitted very well with ZnTe and CdSe structures, respectively, the Te and Cd edge data did not yield satisfactory fits for the pure phases. The details of such fit are found below. The reduced chi-square and R-factor (red text) are considerably larger than for the fit including the CdTe structure. In addition, the error on the coordination numbers (red text) of Te and Cd becomes concerningly high.

Independent points : 47

Number of variables : 12

Chi-square : 128094.0381973

Reduced chi-square : 3649.2403493

R-factor : 0.3589968

Number of data sets : 4

Zn K-edge: k-range = 2.226 - 14.032; R-range = 1.626 - 3.015

Se K-edge: k-range = 1.214 - 17.036; R-range = 1.462 - 2.871

Te K-edge: k-range = 1.5 - 15.749; R-range = 1.623 - 3.082

Cd K-edge: k-range = 2.738 - 13.640; R-range = 1.362 - 2.871

Guess parameters:

$\Delta E_{Cd} = 16.77891154 \pm 4.62561007$

$\Delta r_{CdSe} = 0.01644630 \pm 0.01602724$

$\sigma^2_{CdSe} = 0.00558847 \pm 0.00185946$

$\Delta E_{Te} = -0.93380525 \pm 8.06273200$

$\Delta r_{ZnTe} = 0.00400599 \pm 0.01750406$

$\Delta r_{ZnTe} = 0.00573751 \pm 0.00203375$

$\Delta E_{Se} = 2.70006004 \pm 1.69484742$

$\Delta E_{Zn} = 3.68904013 \pm 1.48844645$

Elemental Coordination Numbers: $N_{Zn} = 3.42508855 \pm 0.84933014$

$N_{Te} = 1.77238426 \pm 1.23013420$

$N_{Se} = 3.97319827 \pm 1.08478048$

$N_{Cd} = 1.74232581 \pm 0.69041057$

Defined parameters: $S^2_{0,Cd} = 0.82000000$

$S^2_{0,Te} = 0.75000000$

$S^2_{0,Se} = 0.73000000$

$S^2_{0,Zn} = 0.92000000$

Chapter 5

Ground-state XANES analysis

In Chapter 4, we showed that, using a global EXAFS fitting analysis at the Zn, Te, Cd, and Se X-ray absorption K-edges, ZnTe/CdSe core/shell quantum dots synthesized by a standard literature procedure[36] in actuality have an alloyed $Cd_xZn_{1-x}Te$ core.[171] The Zn K-edge EXAFS data could be satisfactorily fitted using a pure-phase ZnTe zinc blende input structure (Figure 4.13). The XANES spectrum probes a larger volume surrounding the absorbing atom due to the longer inelastic mean free path and multiple scattering of the photoelectron in this energy region. This renders XANES sensitive to structural distortions beyond the first coordination shell, and therefore alloying. The subject of this Chapter is the modeling and simulation of XANES spectra at all four K absorption edges using the *ab initio* FDMNES code (see Chapter 2). After presenting the experimental and simulated spectra for the pure-phase CdTe and CdSe materials (Section 5.1), we will proceed with the simulation of the Zn K-edge XANES spectrum of the alloyed material $Cd_xZn_{1-x}Te$ in Section 5.2. We employ DFT with hybrid functionals to structurally relax supercells of $Cd_xZn_{1-x}Te$ (x = 0.1-0.9) alloys, which are used as input structures in FDMNES. We show that for Cd fractions of $x \sim$ 0.7-0.9 the simulated XANES spectrum exhibits the best semi-quantitative agreement with the experimental spectrum of the SILAR 2 sample, in good agreement with the results from EXAFS analysis (x = 0.8, Chapter 4). Our results demonstrate the power of DFT in conjunction with XAS codes to assign specific XANES features to long-range structural distortions in alloyed nanomaterials.

Acknowledgements DFT calculations were performed by Erick Hernandez Alvarez in collaboration with Prof. Andre Schleife at UIUC. Details of these calculations are described

in Chapter 3, Section 3.6. We thank Dr. Thomas Rossi and Dr. Ives Joly for fruitful discussion.

5.1 XANES spectra of pure-phase nanomaterials

We measured the static XAS of pure-phase CdTe and CdSe QDs (see Chapter 4 for synthetic details). Due to facile oxidation of Te, we were not able to measure a spectrum of pure-phase ZnTe QDs for comparison. In Figure 5.1a we show the normalized experimental CdTe, CdSe and $Cd_xZn_{1-x}Te/CdSe$ ($x = 0.8$) spectra. Based on the internal structure of the $Cd_xZn_{1-x}Te/CdSe$ QDs, we expect the Cd K-edge spectrum to be similar to a linear combination of Cd K-edge spectra of CdTe and CdSe QDs. Indeed, by using the relative fractions of Cd-Te (0.78) and Cd-Se (0.22) bonds obtained from EXAFS (see Section 4.2) as weighting factors for the pure-phase CdTe and CdSe spectra, respectively, we are able to largely reproduce the spectrum of the alloy (see Figure 5.1a). Here, we neglect the

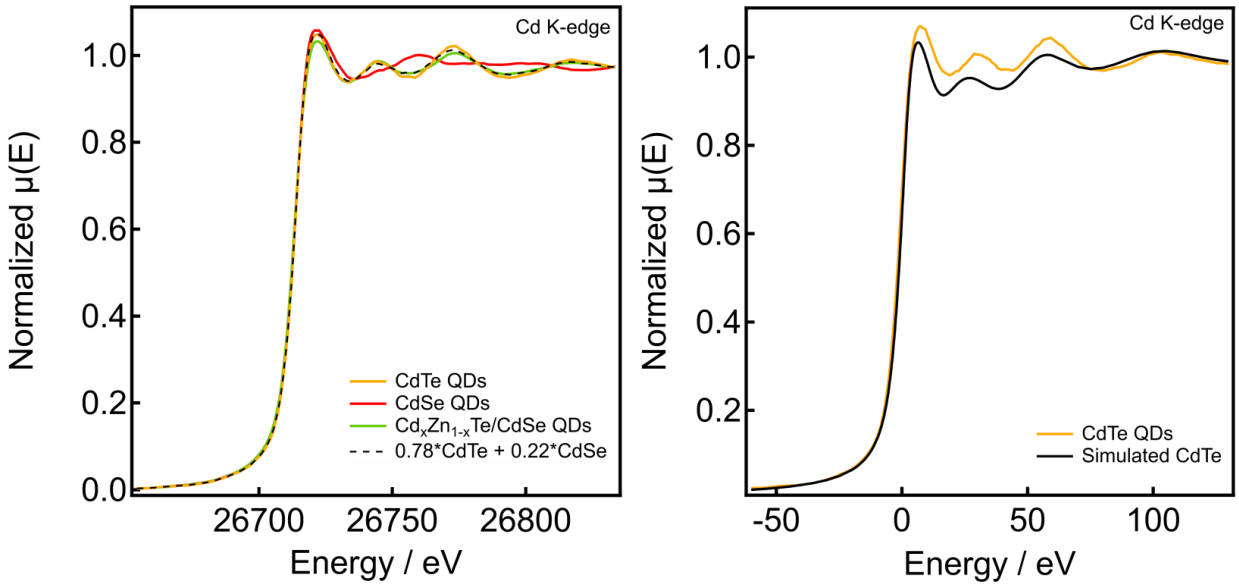

Figure 5.1: (a) Cd K-edge spectra of CdTe Qds, CdSe QDs, and $Cd_xZn_{1-x}Te/CdSe$ ($x = 0.8$). The dashed curve shows a linear combination of experimental CdTe and CdSe spectra using the fractions obtained EXAFS analysis as weighting factors (see text). (b) Experimental and simulated Cd K-edge spectra of CdTe. The energy axis is relative to the Fermi energy.

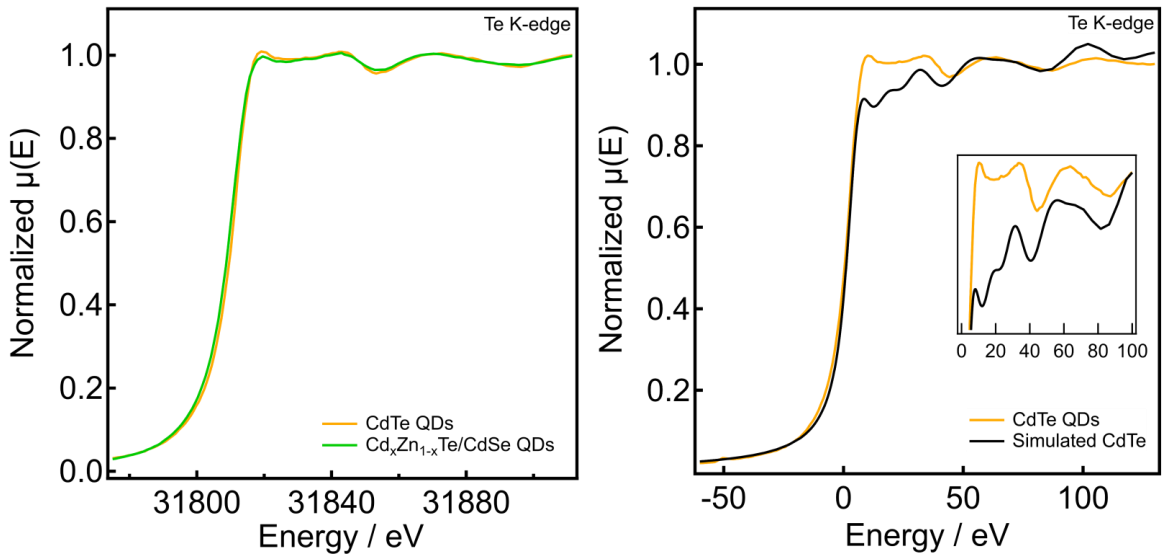

Figure 5.2: (a) Te K-edge spectra of CdTe QDs and $Cd_xZn_{1-x}Te/CdSe$ ($x = 0.8$). (b) Experimental and simulated Te K-edge spectra of CdTe. The energy axis is relative to the Fermi energy.

effect of alloying beyond the first coordination shell, which will be discussed for the Zn K-edge data presented in Section 5.2, and possible size and surface effects. Figure 5.1b shows the experimental Cd K-edge CdTe spectrum together with a simulated spectrum after optimizing all theoretical parameters (see Table 5.3 in Supplementary material for details). The agreement between the two spectra is satisfactory; all major features are reproduced in the simulations. Slight discrepancies in amplitude and peak position are quite typical for the XANES region, and may be related to deficiencies of modeling many-body effects such as the photoelectron self-energy and/or core-hole screening.[186–190]

The experimental Te K-edge spectra of CdTe and $Cd_xZn_{1-x}Te/CdSe$ ($x = 0.8$) are shown in Figure 5.2a. Due to the large core-hole life time broadening at the Te K-edge ($\backsim$10 eV, heavier element having larger attractive potential and therefore shorter life time and larger lifetime broadening[191]), the features are rather broad. The spectra exhibit only slight differences, which is consistent with the fact that the majority of bonds comprises Cd-Te (as opposed to Zn-Te). The simulated Te K-edge spectrum in Figure 5.3b reproduces all main features, but similarly as for the Cd K-edge spectrum, discrepancies between experimental and simulated XANES spectra may be attributed to deficiencies of modeling many-body

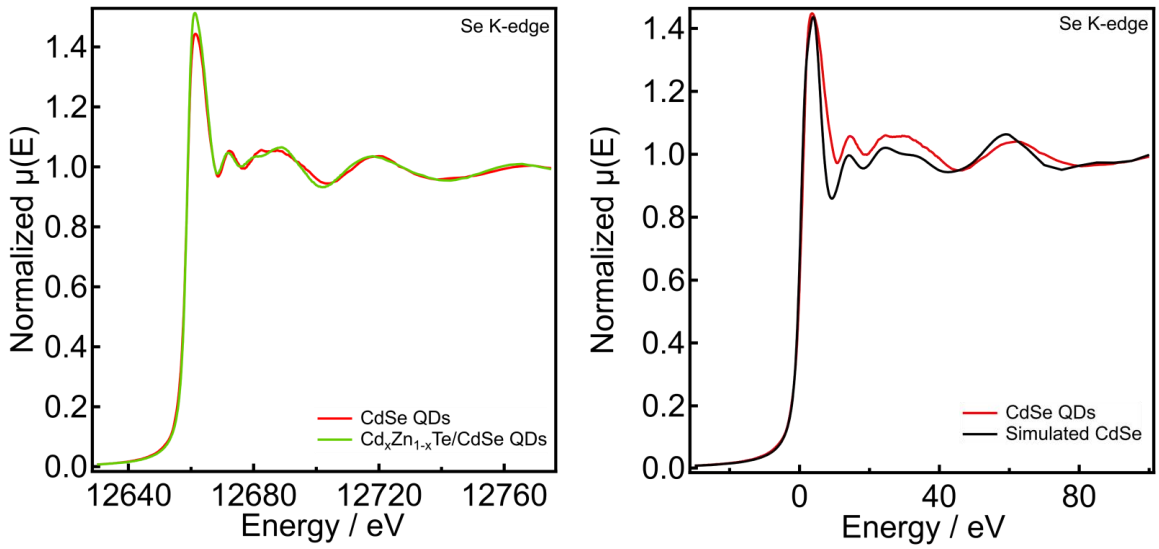

Figure 5.3: (a) Se K-edge spectra of CdSe QDs and $Cd_xZn_{1-x}Te$/CdSe ($x = 0.8$). (b) Experimental and simulated Se K-edge spectra of CdSe. The energy axis is relative to the Fermi energy.

effects.

The Se K-edge data is presented in Figure 5.3. Interestingly, the differences in the spectra of CdSe and $Cd_xZn_{1-x}Te$/CdSe ($x = 0.8$) are relatively large compared to the Cd and Te K-edge data presented in Figs. 5.1a and 5.2a. This is unexpected since Se is only present in the patchy shell of the nanoparticles and anion alloying and/or the formation of Zn-Se bonds was excluded on the basis of the EXAFS analysis. In addition, EXAFS confirmed only a small difference in Se-Cd bond lengths compared to the bulk or CdSe nanophase (see Table 4.6 in Section 4.2). The reason for the deviations seen in Figure 5.3a may lie in the fact that the XANES and EXAFS spectra have different sensitivities. While EXAFS only probes the first-shell bond lengths, which are almost unchanged in the core/shell nanoparticles compared to CdSe QDs, the XANES spectrum is sensitive to *electronic* differences between the Se atoms in the patchy shell of $Cd_xZn_{1-x}Te$/CdSe compared to CdSe QDs. Such electronic effects may, for example, arise from ligand coordination at the surface (a larger percentage of Se atoms will be at the surface for the core/shell particles, compared to the CdSe quantum dots).[173,181,192,193] The simulated Se K-edge spectrum of CdSe is presented in 5.3b, which shows reasonable agreement.

5.2 DFT simulations of alloyed heterostructures

The results presented in Section 5.1 show that the Cd, Te, and Se K-edge XANES spectra of the pure-phase CdSe and CdTe QD materials match the $Cd_xZn_{1-x}Te$/CdSe spectrum quite well, but small differences are apparent. These differences could be due to surface/size effects or alloying in the core of the nanoparticle. Of all absorption edges, the Zn K-edge is expected to be mostly affected by alloying. Since about 20% of the cations in the nanoparticle core are Zn atoms, the second coordination shell (12 atoms) around Zn is mainly composed of Cd atoms, which have a different ionic radius (88 pm for Zn^{2+} *vs* 108 pm for Cd^{2+}).[194] This leads to a considerable amount of strain in the local vicinity of the Zn atoms that may not be reflected in a first-shell EXAFS analysis, but could be probed using XANES due to long-range multiple scattering effects (up to $\sim$ 10Å from the absorbing atom) that dominate in this region.[70] XANES also is less affected by structural disorder relative to EXAFS, the interpretation of which becomes more complicated with highly disordered materials, like nanomaterials.[70–74] We therefore conducted a systematic XANES study of the alloyed $Cd_xZn_{1-x}Te$ material and used DFT to relax the structure in order to take into account local distortions. The alloyed materials simulated in this study were bulk (not nanomaterials). The supercell structures generated by the external DFT calculations (outside of FDMNES) are then used as an input into the FDMNES program to simulate the Zn K-edge XANES spectra. By varying the fraction of Zn atoms in the supercells, we identify a unique feature that is sensitive to alloying. From a semi-quantitative comparison with the experimental spectrum we conclude that the alloy contains a fraction of 10-30% Zn, in good agreement with the EXAFS results. The use of DFT to optimize structures of alloyed materials has been shown previously.[62] Here we combine such analysis with *ab initio* XANES simulations as a way to corroborate the structural characterization using EXAFS, TEM and elemental analysis (Chapter 4). We note that the application of the well-known Vegard's law is not warranted here. Vegard's law is an empirical finding that predicts that the lattice param-

eter of a solid solution of two constituents is approximately a weighted mean of the two constituents' lattice parameters at the same temperature.[195] The law has been verified extensively by XRD that probes the average of all bond lengths in the material,[147] although deviations from linear dependence have been reported.[63–69] XAS, on the other hand, is sensitive to the element-specific structure in the vicinity of the absorbing atom which is subject to local distortions that intricately depend on the ionic radii, lattice symmetry, and electronic structure.[70–74] This has lead to profound deviations between the first-shell bond lengths determined by EXAFS and average bond lengths predicted by Vegard's law and measured by XRD.[62–69]

5.2.1 Generating the supercells for DFT calculation

The first step to prepare for the DFT calculations is to generate supercells of the alloyed $Cd_xZn_{1-x}Te$ structure that represent specific fractions of Cd *vs* Zn atoms. A supercell is a real-space volume that encompasses an integer multiple of crystallographic unit cells. Supercells are often used in cases where the crystal symmetry is broken, such as for crystal defects/vacancies, crystal/vacuum interfaces, or alloying,[196] and periodic boundary conditions are needed for reciprocal space calculations. In our case, we generate supercells based

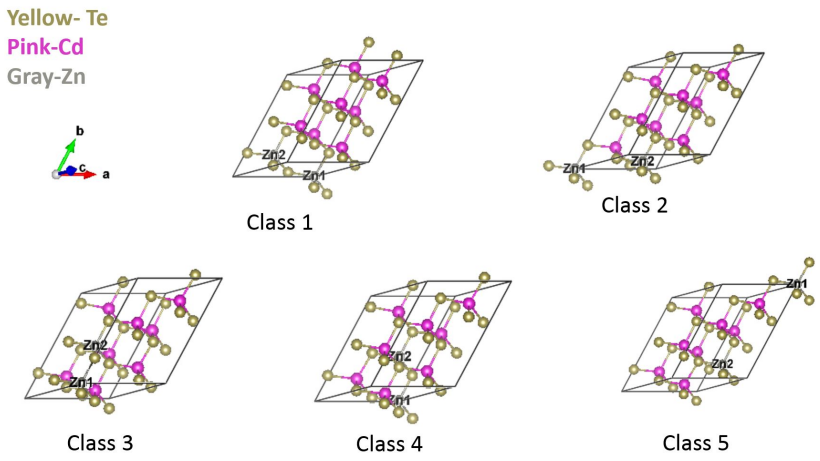

Figure 5.4: Five supercell classes (symmetry-equivalent cells) for a 20-atom supercell of $Cd_xZn_{1-x}Te/CdSe$ ($x = 0.8$).

on 10 zinc blende CdTe primitive unit cells for a total of 20 atoms. We then replace between one and nine Cd atoms by Zn in order to obtain Zn fractions of 10-90%, respectively. For each Zn fraction, several different configurations exist, which vary in the relative separation between the substituted Zn atoms. For the case of 20% Zn (*i.e.* $x = 0.8$), a total of 45 possible configurations is obtained by replacing two Cd atoms by two Zn atoms inside the supercell. Several configurations are equivalent by symmetry, which reduces the total number of unique supercell classes to five, shown in Figure 5.4 for 20% Zn fraction. The supercells were then used as input structures of the DFT program and the lattice was relaxed in order to find the absolute minimum in ground-state energy for each class (see Chapter 3 for details). The numbers of equivalent configurations per class and the DFT ground-state energies (relative to the vacuum) for a 20% Zn fraction as an example are listed in Table 5.1.

Table 5.1: 45 configurations categorized into 5 different classes for a 20-atom unit cell of $Cd_xZn_{1-x}Te$ ($x = 0.8$). The total ground-state (GS) energy as calculated by DFT is given in the right column.

Class id.	**Equiv. configs.**	**GS energy (eV)**
1	10	-50.087303
2	5	-50.079206
3	10	-50.101211
4	10	-50.087758
5	10	-50.093205
total	45	–

,

5.2.2 XANES simulations of $Cd_xZn_{1-x}Te$ alloys

To test our supercell approach to calculate XANES spectra, we generate a 20-atom supercell of pure-phase ZnTe and compare the corresponding simulated Zn K-edge spectrum with the one obtained using a two-atom primitive zinc blende unit cell as an input structure in FDMNES. The results are given in Figure 5.5, which shows that the spectra are virtually identical, as expected.

Next, we use the structurally relaxed supercells from DFT (using PBE-GGA, see Section 3.6) to simulate the Zn K-edge spectra of the ternary $Cd_xZn_{1-x}Te$ alloy. For each supercell class, each unique Zn atom was chosen as the absorber and the resulting spectra from different Zn atoms were averaged. Figure 5.5 shows the simulated spectra for the five supercell classes with a Zn fraction of 20%. Overall, the spectra look very similar, but there are slight differences in the intensity of the shoulder feature around 30 eV; while the spectra of Class 1 and 2 have a reduced shoulder intensity, the spectra of Class 3, 4, and 5 have an increased intensity and they match very well. Indeed, we can correlate the intensity of this feature with the number of Zn atoms in the second coordination shell surrounding a central Zn atom. Class 1 and 2 both have two Zn atoms in the second coordination shell, while Class 3, 4, and 5 only have one Zn atom in the second coordination shell. We will show below (Figure 5.6) that the inverse correlation between number of second-shell Zn atoms and shoulder intensity ~30 eV is corroborated by a systematic variation of the Zn fraction inside the supercell. Since the differences between the spectra of different classes are very small, however, we

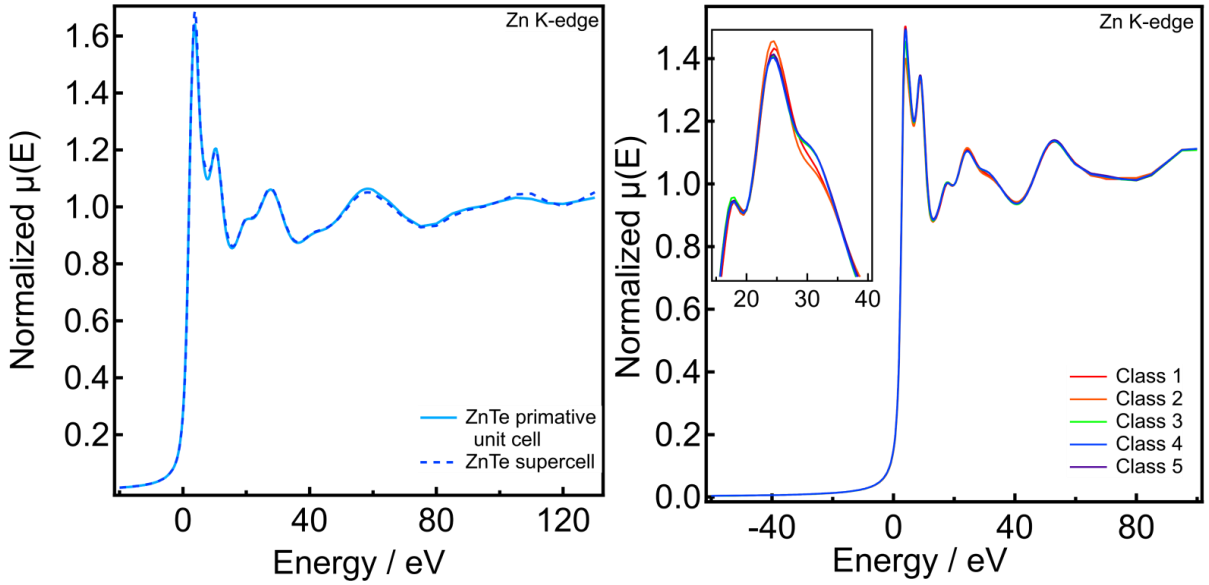

Figure 5.5: (a) Comparison between the simulated Zn K-edge spectrum using the two-atom primitive zinc blende unit cell and a 20-atom supercell; (b) Comparison between simulated Zn K-edge spectra using the five different supercell classes of Figure 5.4. The energy axis is relative to the Fermi energy.

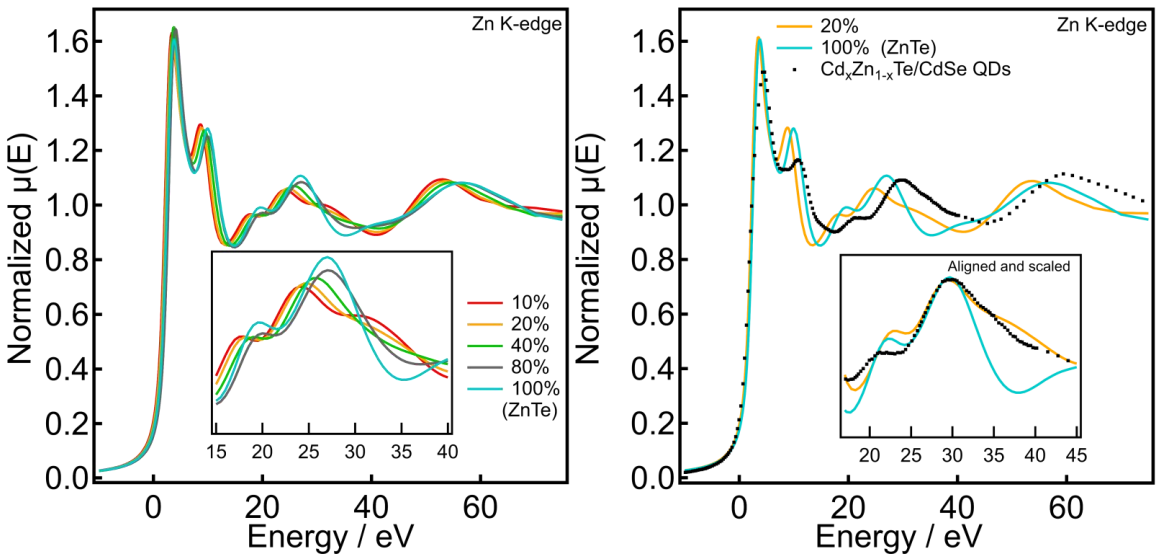

Figure 5.6: (a) Simulated Zn K-edge spectra for ternary $Cd_xZn_{1-x}Te$ alloys with Zn fractions ranging from 10% to 100%; (b) Comparison between the simulated $Cd_xZn_{1-x}Te$ spectrum with 20% Zn, the pure-phase ZnTe spectrum, and the experimental $Cd_xZn_{1-x}Te$ ($x = 0.8$) data. The inset shows a zoom into the XANES feature that is mostly sensitive to the relative Cd and Zn fractions. The simulated spectra in the inset have been shifted and scaled such that the maxima of the peaks are aligned. The energy axis is relative to the Fermi energy.

can take the simulation of one class to be representative of all classes without the need to calculate and average together the spectra for all classes and for each Zn fraction (Class 1 is taken for all spectra shown below). While we explicitly only show the validity of this assumption for the 20% Zn case, we assume this to be valid for other relative Zn fractions as well.

In Figure 5.6a we show the simulated XANES spectra for Zn fractions ranging from 10% to 100% (pure ZnTe). First, we notice a systematic blue shift of all features as the fraction of Zn is increased. As described semiempirically by Natoli's rule,[197] the position of XAS features scales inversely with the bond lengths in the local vicinity of the absorber (here Zn). The blue shift therefore indicates a contraction of the lattice for increased Zn fraction in the alloy, which is in qualitative agreement with predictions for the lattice parameters using Vegard's law applied to a mixture of ZnTe and CdTe.[195] Indeed, the lattice constant of ZnTe (a =6.11 Å) is ∼6% smaller than that of CdTe (a =6.48 Å).[146] Interestingly, however, besides

the blue shift, the spectra develop a shoulder on the high-energy side of the absorption feature around 27 eV as the Zn fraction *decreases*. This distinct feature appears rather abruptly for Zn fractions smaller than ∼30%. The experimental data, while red shifted with respect to the simulation, also shows a weak shoulder for this feature. Figure 5.6b compares the simulation for 20% Zn and 100% Zn (*i.e.* pure ZnTe) with the experimental data, which clearly shows that the high-energy slope of the peak around 27 eV can only be matched for relatively low Zn fractions. Semi-quantitatively, the best match between the simulation and the experimental data is obtained for Zn fractions of 10-30%, which is in good agreement with the value of 20% obtained from EXAFS (Chapter 4). Due to contributions of multiple scattering paths and complex many-body effects in the XANES region,[189] the actual assignment of the high-energy shoulder feature around 32 eV (Figure 5.6b) to a specific structural distortion, multiple scattering path, or other process is challenging. However, since this feature appears for Zn fractions <30%, that is, when the second coordination shell with twelve atoms contains less than three Zn atoms, the shoulder feature could be related to multiple scattering involving multiple Cd atoms in the second (and higher) coordination shell(s).

Resolving discrepancies between simulation and experiment

From Figure 5.6b it is clear that the salient features in the XANES spectrum are systematically red shifted in the simulation compared to the experimental spectrum. We identify two reasons for this: (1) the overestimation of the unit cell volume by the DFT PBE-GGA method used to optimize the structure of the alloyed supercells;[198] (2) the underestimation of the electronic band gap as calculated by LDA DFT, which is implemented in FDMNES.[198,199] Both are well-known problems in DFT calculations and they ultimately relate back to the underlying approximation of the unknown exchange-correlation functional.[198]

To approximately correct for the first issue of the overestimated unit cell volume, we uniformly contract the alloyed supercells from the DFT PBE-GGA calculation in such a way that the average Zn-Te and Cd-Te bond lengths in the supercell match those determined

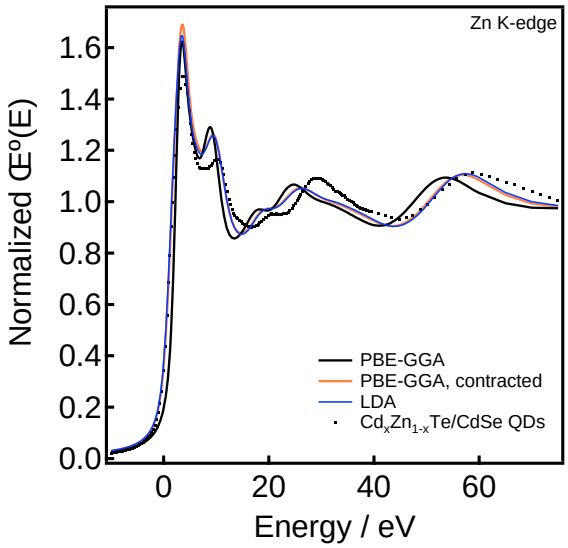

Figure 5.7: Comparison between the Zn K-edge XANES spectra for the supercell structure with 20% Zn relaxed using PBE-GGA (black) and LDA (blue) levels of DFT theory. The PBE-GGA-relaxed supercell contracted by 2.6% is shown in orange. The experimental data for $Cd_xZn_{1-x}Te/CdSe$ ($x = 0.8$) core/shell QDs corresponds to the dotted curve. The energy axis is relative to the Fermi energy.

by EXAFS (see Table 5.2). For a Zn fraction of 20% the necessary compression is 2.6%. Figure 5.7 shows the original simulation using the uncompressed supercell from the PBE-GGA calculation, the same supercell contracted by 2.6% along the a, b and c unit cell axes, as well as a supercell structurally relaxed using a LDA DFT calculation (see Section 3.6 for

Table 5.2: Average Zn-Te and Cd-Te bond lengths (in Å) obtained from the DFT-relaxed $Cd_xZn_{1-x}Te$ supercell calculations (PBE-GGA and LDA) as a function of Zn fraction (in percent, top row). The bottom row shows the bond lengths obtained from EXAFS fitting (Chapter 6).

		Zn %:									
	Bond	**10**	**20**	**30**	**40**	**50**	**60**	**70**	**80**	**90**	**100** (ZnTe)
PBE-GGA	Zn-Te	2.702	2.703	2.703	2.698	2.695	2.693	2.689	2.685	2.681	2.680
PBE-GGA	Cd-Te	2.865	2.863	2.858	2.856	2.853	2.847	2.844	2.838	2.833	-
LDA	Zn-Te	-	2.62	-	-	-	-	-	-	-	-
LDA	Cd-Te	-	2.77	-	-	-	-	-	-	-	-
EXAFS	Zn-Te	-	2.634	-	-	-	-	-	-	-	-
EXAFS	Cd-Te	-	2.787	-	-	-	-	-	-	-	-

details). Interestingly, the latter two spectra overlap almost perfectly, which implies that the average bond lengths derived from the LDA calculation yields a very good agreement with the EXAFS data. Clearly, all XANES features blue shift upon contraction of the lattice, as expected from Natoli's rule.[197] The resulting, optimized simulated spectrum, however, is still systematically red shifted compared to the experiment.

In order to investigate the remaining discrepancies between simulated and experimental spectra, we compare the local p-projected DOS at the absorbing Zn atom. We focus on the p-projected DOS, because the optical selection rules dictate that transitions from s-core levels into states with p-symmetry are dipole-allowed and therefore dominate the spectral features in a K-edge XAS spectrum. Figure 5.8a shows the p-DOS as calculated using the standalone DFT code VASP with the LDA and HSE exchange-correlation functionals, as well as the p-DOS calculated by FDMNES, the corresponding simulated spectrum, and the experimental

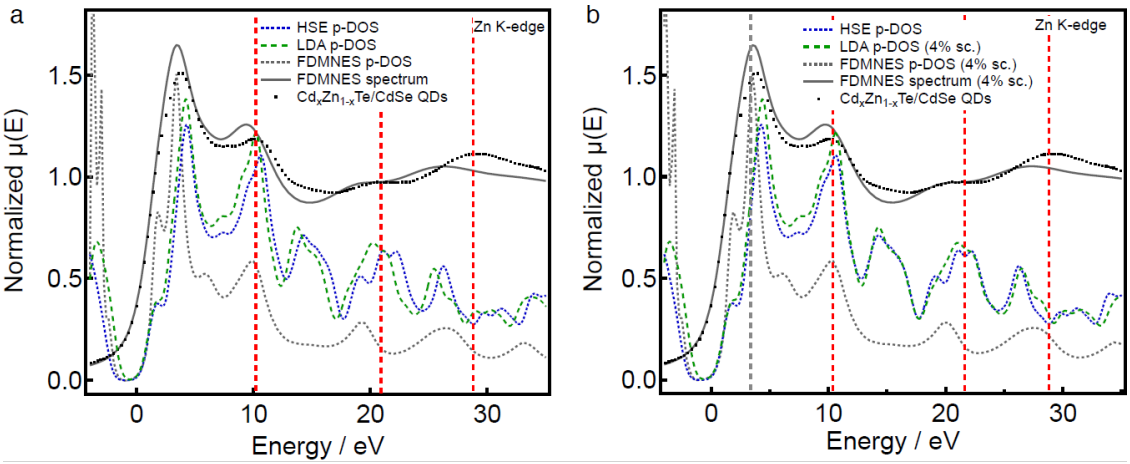

Figure 5.8: (a) Comparison between the pDOS calculated using a standalone DFT code (HSE and LDA) and FDMNES, together with the FDMNES spectrum and experimental $Cd_xZn_{1-x}Te/CdSe$ ($x = 0.8$) data. The input structure for the DOS calculations was the one that was relaxed at the LDA level of DFT theory (see text). The HSE and LDA DOS have been aligned horizontally such that the maxima in density match the FDMNES pDOS maximum ~3.5 eV (grey dashed vertical line). (b) Same data as in (a) but the energy scale of the LDA and FDMNES pDOS, and FDMNES spectrum have been scaled by 4%. The latter value was determined by matching the LDA and HSE pDOS. In both (a) and (b), the LDA, HSE, and FDMNES DOS curves have been arbitrarily scaled vertically (no vertical axis assigned). The red vertical dashed lines indicate prominent features in the experimental XANES spectrum. The energy axis is relative to the Fermi energy of the FDMNES calculation.

data. First, we note that the p-DOS from FDMNES, which uses the LDA functional, is less structured and lacks some features compared to the LDA p-DOS calculated with VASP. There can be two reasons for this: (1) FDMNES calculates the densities and potential in real space,[132] as opposed to reciprocal space for common DFT codes such as VASP. Real-space or cluster DFT can be employed when the symmetry of the unit cell is broken,[132] which is the case here due to the core-hole; (2) there may be changes in the way that the local l-projected DOS is derived. The l-projection is not well-described in the FDMNES manual, which prevented us from adopting the exact same procedure. Furthermore, the peaks in the LDA p-DOS (from VASP) are systematically red-shifted compared to the HSE p-DOS, with the energy shift becoming larger as the energy increases. This effect is related to the underestimation of the band gap for LDA- or GGA-based calculations.[198,199] The HSE functional has been specifically developed to improve the estimation of band gap values from DFT.[156] Here, we do not compare the band gap values, but rather focus on the higher-energy features.[200] The origin of the mismatch lies in the deficiencies in the treatment of exchange-correlation in the LDA calculation.[196,201] As plotted in Figure 5.9, the region between the Fermi energy and 20 eV is fairly linear and has a slope of approximately 4% as fitted to a straight line (shown by the red curve). To correct for these deficiencies in an *ad hoc* way, we apply the linear scaling of 4% to the energy axis of the LDA p-DOS, where the energy origin is chosen to be the Fermi energy (the VASP DOS data has been aligned to the rising edge of the conduction band). In Figure 5.8b we overlap the scaled LDA p-DOS with the HSE p-DOS, showing reasonable agreement.

We apply the same scaling to the LDA DOS from FDMNES and the simulated spectrum under the assumption that they suffer from the same deficiencies. However, as is seen Figure 5.8b, 4% scaling is not sufficient to optimally match the simulation with experiment. Another 5% scaling of the energy axis would be necessary to obtain satisfactorily agreement, as shown in Figure 5.10. We assign the remaining energy shift to the lack of an adequate description of the electron-core-hole interactions in the final state, as suggested in Reference

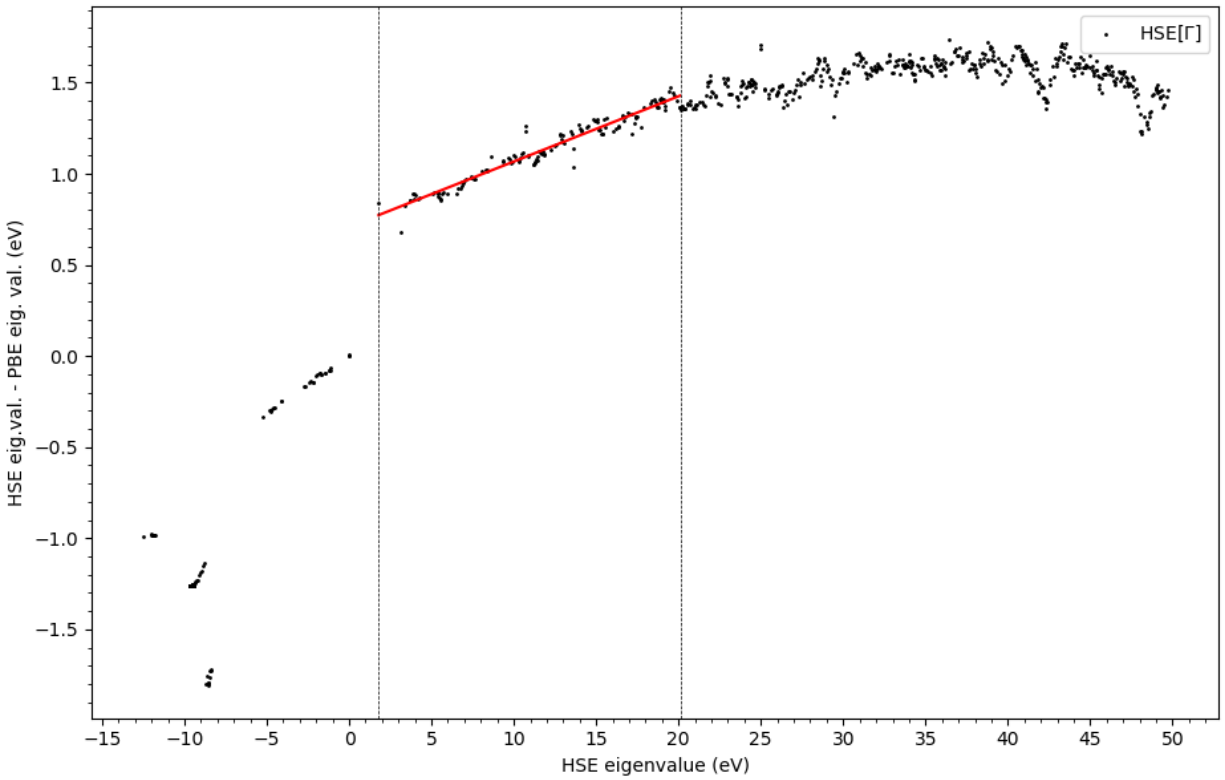

Figure 5.9: Quasiparticle shift for DFT-PBE eigenvalues, plotted as a function of the corresponding HSE eigenvalue. This data was computed using a 2×2×2 and a 6x6x6 Gamma centered Monkhorst–Pack k-point grid for HSE and PBE, respectively.

186. We would like to point out that the scaling we apply scales linearly with energy. This linear dependence is determined phenomenologically; it does not necessarily imply a linear dependence of the correction in the mathematical sense. In fact, the actual energy dependence of the correction terms may depend on energy in a complex, unknown way. For example, in the case of the well-known Hedin-Lundqvist exchange correlation, which is often used in XAS, the energy shift will scale with $1/\sqrt{E}$. Clearly, such dependence is not seen in our data. Both the *ab initio* treatment of the exchange-correlation (or self-energy) and electron-core-hole interactions in XAS are active topics of current research.[202–206] Future work could include the exploration of more sophisticated models for many-body effects in XANES spectra of ternary alloys, such as the material studied here.

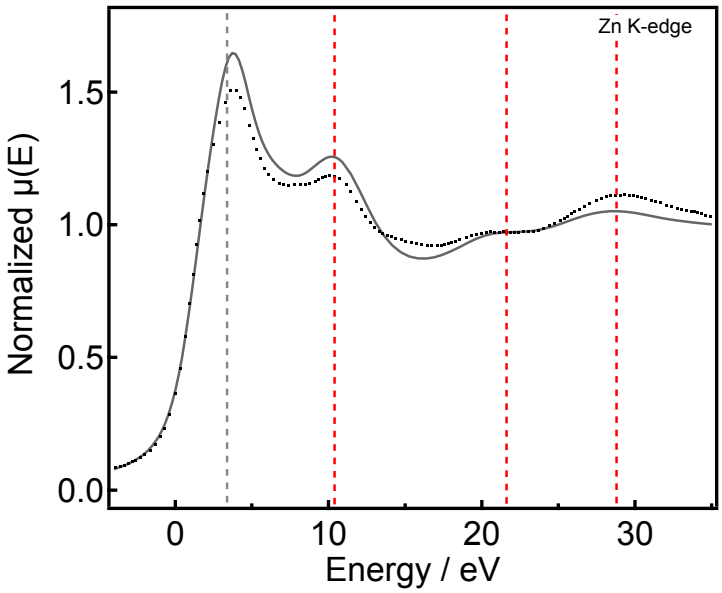

Figure 5.10: Experimental Zn K-edge spectrum of $Cd_xZn_{1-x}Te/CdSe$ ($x = 0.8$) QDs and the best-match simulated FDMNES spectrum after applying an energy scaling of 5% compared to the simulated spectrum in Figure 5.8b. The total energy scaling compared to the raw spectrum amounts to 9%. The input structure for the XAS simulation was the one that was relaxed at the LDA level of DFT theory.

5.3 Conclusion and outlook

In summary, we sought to gain qualitative understanding of the effect of alloying in the XANES. To do so, we employed DFT to relax supercells of a representative $Cd_xZn_{1-x}Te$ alloys. We input these supercells in FDMNES, a X-ray spectroscopy simulation code. Because Zn is most sensitive to alloying, we focused on modeling of the Zn K-edge XANES. The simulated XANES spectrum of a $Cd_xZn_{1-x}Te$ (x=0.8) alloy is in excellent agreement with the experimental XANES spectrum (Figure 5.10). In addition, we demonstrated that even though EXAFS is not sensitive beyond the first coordination shell, XANES is very sensitive to scattering from several coordination shells. By simulating the XANES spectra of several alloy compositions, we identified the features which are sensitive to alloying. In section 5.2.2, we demonstrated some of the current limitations of the FDMNES code. However, by comparing the DOS from FDMNES to the DOS from a higher level of DFT, we can justify

applying a scaling factor to the energy axis to improve the agreement with the experimental spectrum. In the future, the developers of the FDMNES may consider expanding the code such that input files from the VASP program package may be used. Currently, users who wish to import the results from higher level DFT must run their DFT calculation through the Wien2k program package.

5.4 Supplementary material

5.4.1 Simulation parameters

The simulated spectra presented in the above sections were calculated using the SCF/FDM procedures in FDMNES. The common energy axis for simulated and experimental spectra was obtained by aligning the maxima of the first derivative of the spectra. We also simulated the spectra using the MT approximation and MST formalism using FDMNES. These calculations consistently resulted in worse agreement with the experimental data, which demonstrates the importance of full potentials in XANES calculations.[132] Similarly, XANES simulations without employing the SCF loop did not yield satisfactorily agreement with the data. We have tested the convergence of the spectra with respect to the SCF cluster size, which was set to be the same as the cluster size used in the calculation of the absorption cross sections (or MST cluster size). The series for the Zn K-edge spectra of pure-phase ZnTe is shown in Figure 5.11, which shows that convergence is achieved for a cluster size of $\sim$7 Å. The optimum parameters used in the calculations of the various compounds at the respective edges are provided in Table 5.3.

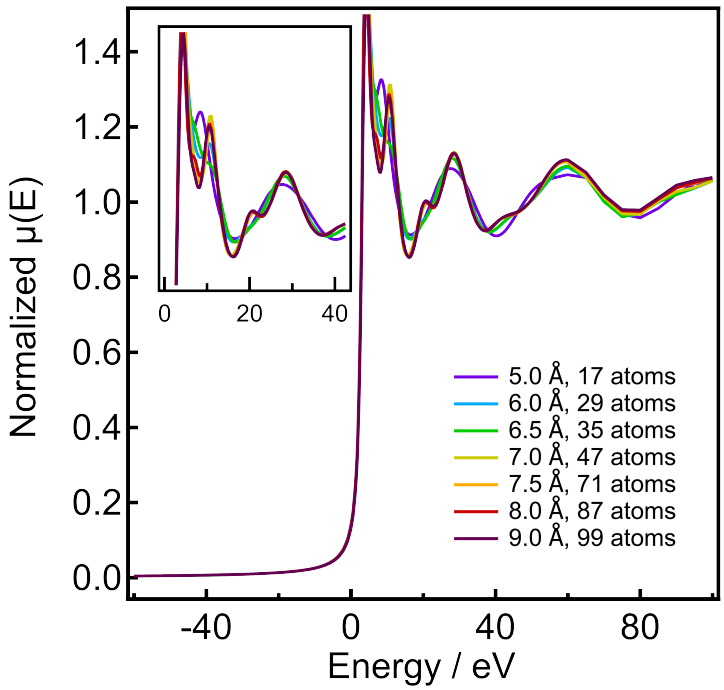

Figure 5.11: Dependence of the simulated Zn K-edge pure-phase ZnTe XANES spectrum on the cluster radius (in Å) and number of atoms in the cluster. Convergence is achieved for a cluster size of ∼7 Å.

Table 5.3: Optimized FDMNES parameters.

Element	Material	Energy Range (eV)	Cluster Size (Å)	Relativistic Effects?
Zn	ZnTe	-200 to 190	7.0	No
Cd	CdTe	-60 to 130	5.0	Yes
Te	CdTe	-200 to 130	5.0	Yes
Se	CdSe	-60 to 130	6.0	Yes
Zn	$Cd_xZn_{1-x}Te$	-200 to 190	7.5	No

5.4.2 FDMNES input files

Zn Edge: ZnTe

```
Range

-200.0 5.0 -20.0 1.0 -10.0 0.2 10.0 0.5 60.0 5.0 190.0

Relativism

Z_absorber

30

SCF

N_self

200

R_self

5.0

Radius

5.0

Crystal

6.10 6.10 6.10 90.0 90.0 90.0

30 0.0 0.0 0.0

52 0.25 0.25 0.25

Spgroup

F-43m

Convolution

Gaussian

End
```

Cd Edge: CdTe

```
Range
-200.0 5.0 -20.0 1.0 -10.0 0.2 10.0 0.5 60.0 5.0 190.0
Relativism
Z_absorber
48
SCF
N_self
200
R_self
5.0
Radius
5.0
Crystal
6.48 6.48 6.48 90.0 90.0 90.0
48 0.0 0.0 0.0
52 0.25 0.25 0.25
Spgroup
F-43m
Convolution
Gaussian
End
```

Te Edge: CdTe

```
Range
-200.0 5.0 -20.0 1.0 -10.0 0.2 10.0 0.5 60.0 5.0 190.0
Relativism
Z_absorber
52
SCF
N_self
200
R_self
5.0
Radius
5.0
Crystal
6.48 6.48 6.48 90.0 90.0 90.0
48 0.0 0.0 0.0
52 0.25 0.25 0.25
Spgroup
F-43m
Convolution
Gaussian
End
```

Se Edge: CdSe

```
Range
-60.0 5.0 -20.0 1.0 -10.0 0.2 10.0 0.5 60.0 5.0 130.00
Relativism
Radius
6.0
Density
Z_Absorber
34
SCF
R_self
6.0
N_self
2000
P_self
0.025
P_self_max
0.025
Crystal
6.08000 6.08000 6.08000 90.0 90.0 90.0
48 0.0 0.0 0.0
34 0.25 0.25 0.25
Spgroup
F-43m
Convolution
Gaussian
End
```

Zn Edge: $Cd_xZn_{1-x}Te$

```
Range
-200.0 5.0 -20.0 1.0 -10.0 0.2 10.0 0.5 60.0 5.0 190.0
Relativism
Radius
7.5
Atom
30
48
52
Density
Absorber
1
SCF
R_self 7.5
N_self
2000
P_self
0.025
P_self_max
0.025
Crystal
7.73900 10.96630 10.01530 68.6 58.9 62.0
1 0.99736 0.00364 0.00141
1 0.30554 0.19504 0.09883
2 0.49960 0.99806 0.49797
2 0.09885 0.39853 0.70763
2 0.61032 0.38928 0.19592
2 0.90730 0.59757 0.29424
2 0.80306 0.20040 0.60413
2 0.19977 0.80230 0.39380
2 0.39109 0.60334 0.80503
2 0.68877 0.81111 0.90246
3 0.02196 0.23283 0.00425
3 0.20226 0.05685 0.38682
3 0.30469 0.43346 0.09854
3 0.50113 0.24821 0.50337
3 0.60158 0.64468 0.19704
3 0.69902 0.05741 0.91354
3 0.79758 0.45550 0.60175
3 0.09026 0.65667 0.69985
3 0.90335 0.85517 0.28433
3 0.37650 0.85996 0.80908
Convolution
Gaussian
Ecut
0.0
End
```

Chapter 6

X-ray transient absorption spectroscopy

This Chapter presents the results of the time-resolved XAS experiments performed at the 7ID-D beam line at the APS (see Section 3.7.3 for experimental details). In Section 6.1, we describe the X-ray transient absorption (XTA) signals at the Zn and Se K-edges that are used for further analysis. By comparing the XTA kinetics to heat diffusion simulations in Section 6.2, we assign the short-lived decay component to heat diffusion from the nanoparticles into the solvent and we derive the corresponding interfacial thermal conductance (G) under two laser fluence conditions. In Section 6.3 we present an overview of the various XTA effects that can be expected based on the electronic and photothermal excitation processes. Finally in Section 6.4, we present the detailed transient EXAFS and XANES analyses. It will be shown that, while the EXAFS spectrum delivers precise structural information for the excited state, the changes in the XANES spectrum are due to a combination of electronic and structural changes in the excited QDs.

Acknowledgements The heat equation calculations were performed by Yuanheng Wang, and the DFT calculations were done by Erick Hernandez Alvarez. We thank Dr. Gilles Doumy, Dr. Anne Marie March, Dr. Don Walko, Dr. Andre Al Haddad, and Dr. Ming-Feng Tu, Dr. George Sterbinsky, Dr. Tianpin Wu, and Dr. Steve Heald for assistance during measurements at the APS. We also thank the members of the van der Veen lab for their assistance during the XTA beam times: Dr. Renske van der Veen, Conner Dysktra, Tyler Haddock, Ryan Cornelius, Allan Sykes, and Thomas Dixon. We thank Dr. Thomas Rossi for development of the Fermi alignment correction described in this chapter and we thank Conner Dykstra for his help in developing data processing scripts. We thank Dr. Ives Joly

for helpful discussions.

6.1 X-ray transient absorption spectra and kinetics

Figure 6.1 shows the Zn K-edge ground state absorption spectrum recorded in total fluorescence yield (TFY) mode, along with the XTA (excited minus unexcited) spectra of the SILAR 2 $Cd_xZn_{1-x}Te$/CdSe CSQDs dispersed in toluene. At the Zn edge, we measured the XTA spectra 90 ps after excitation with a ps-laser tuned to 532 nm at two fluences: 80 mJ/cm^2 (approximately 600 photons absorbed per QD) and 30 mJ/cm^2 (approximately 230 absorbed photons per QD). Photoexcitation at 532 nm leads to above-band gap excitation of the $Cd_xZn_{1-x}Te$, with an approximate excess energy of 0.58 eV. For the higher fluence, we also measured a transient XAS spectra at 2.5 ns delay after excitation. The signal-to-noise ratio was too low to measure an XTA spectrum at 2.5 ns delay and low laser fluence. Zooms into the Zn edge XANES and EXAFS regions are shown in Figures 6.2a and 6.2b, respectively. The XTA features directly reflect the electronic and structural changes of the absorbing atoms in the excited state. For the high power signal measured at 90 ps delay, the maximum of the transient spectrum amounts to $\backsim$2% of the edge jump, while changes in the EXAFS spectrum are $\backsim$0.2 to 0.5% of the edge jump. For the lower fluence and the long time delay (2.5 ns), the maximum of the transient amounts to even less, $\backsim$0.5% of the edge jump, while changes in the EXAFS spectrum are $\backsim$0.1 to 0.2% of the edge jump. Figure 6.3, shows the Se K-edge ground state absorption and XTA spectrum recorded in total fluorescence yield (TFY) mode $\backsim$90 ps after excitation with a ps-laser tuned to 532 nm, at the lower laser fluence (30 mJ/cm^2).

6.1.1 Excited state decay monitored by transient XANES

In Figure 6.4a, we show the temporal evolution of the maximum XTA signal at the Zn edge (9663 eV) and the Se edge (12658 eV). In Figure 6.4b, we normalized the kinetic traces

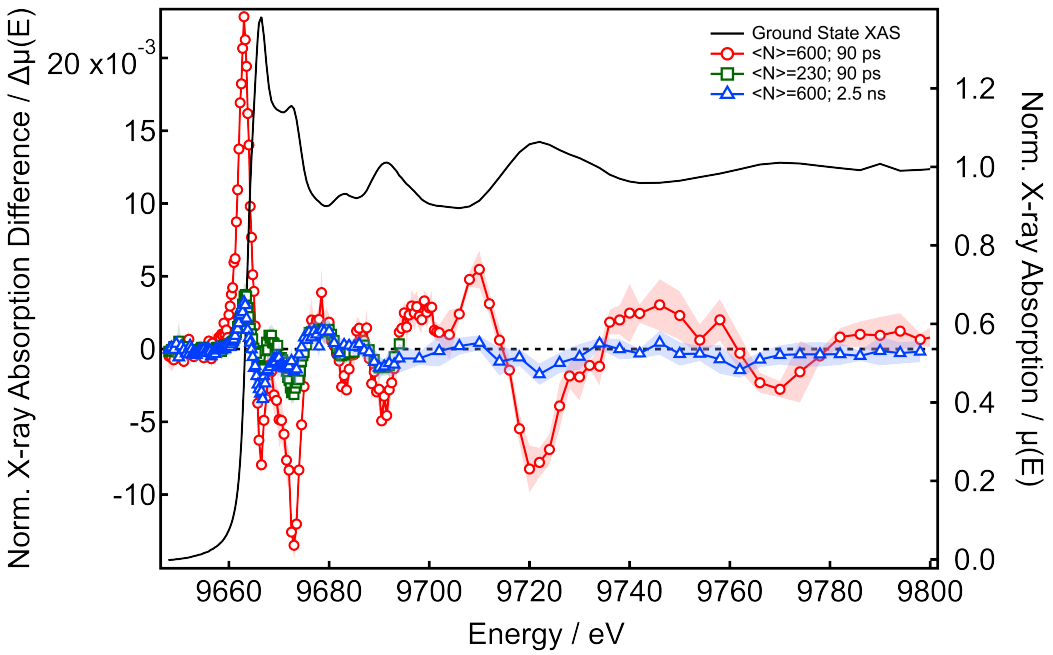

Figure 6.1: Experimental ground-state XAS (black, right axis) and XTA (left axis) after photoexcitation with 532 nm pulse. Three experimental conditions are shown: The XTA spectrum for an average of ∽600 absorbed photons per QD at ∽90 ps after excitation (red), for an average of ∽230 absorbed photons per QD at ∽90 ps after excitation (green), and for an average of ∽600 absorbed photons per QD at ∽2.5 ps after excitation (blue). The shaded area around the data represents the standard error of the experimental measurement.

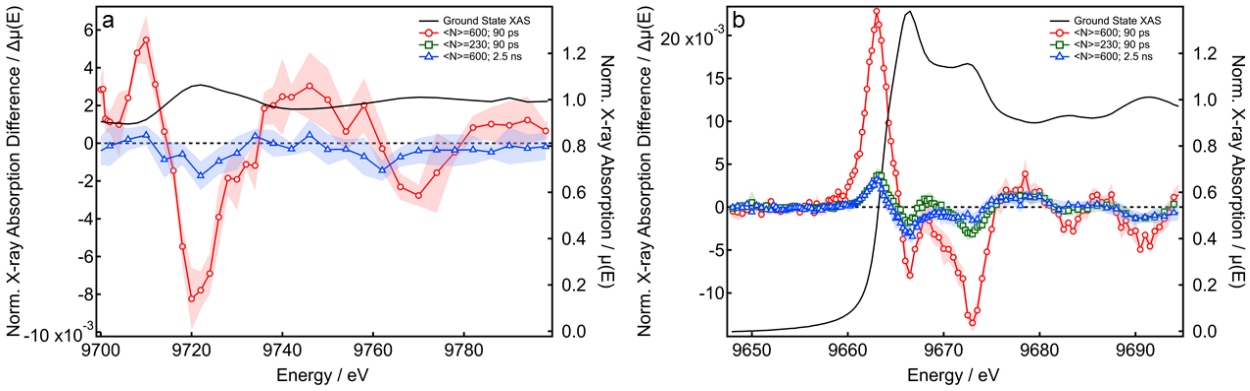

Figure 6.2: Experimental ground-state XAS (black, right axis) and transient XANES (a) and EXAFS (b) (left axis) after photoexcitation with 532 nm pulse. Three experimental conditions are shown: The XTA spectrum for an average of ∽600 absorbed photons per QD at ∽90 ps after excitation (red), for an average of ∽230 absorbed photons per QD at ∽90 ps after excitation (green), and for an average of ∽600 absorbed photons per QD at ∽2.5 ps after excitation (blue). The shaded area around the data represents the standard error of the experimental measurement.

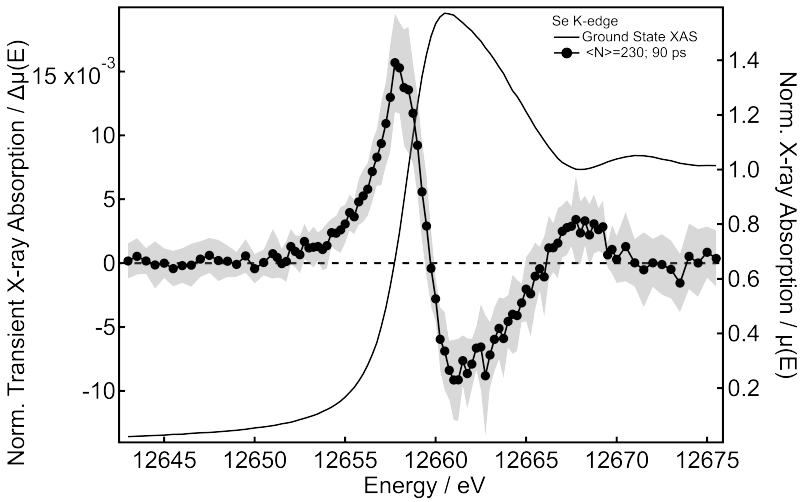

Figure 6.3: Experimental ground-state XAS (black solid line) and XTA ∽90 ps after photoexcitation with 532 nm pulses with a fluence of 30 mJ/cm^2 (approximately 230 photons/QD; solid black circles). The shaded area around the data represents the standard error of the experimental measurement.

to 1 and compare them to the TRPL decay at 535 nm excitation, which was presented in Section 4.1.1. The decay curves are each overlapped in Figure 6.4a with a biexponential fit curve. The summary of the parameters of the biexponential fits are presented in Table 6.1. For all X-ray kinetic fits, the first component is in the ∽100-200 ps range, and the second component is in the ∽1-6 ns range. In contrast, the biexponential fit to the TRPL data has decay times of ∽750 ps and ∽10 ns.

Table 6.1: Parameters of the biexponential fits of the kinetic traces of Figure 6.4a and the TRPL data in 4.1c. A1/A2 is the ratio of the amplitudes of each component. C1 and C2 are the decay parameters of the fits. The first three rows represent the fits to the X-ray kinetics. <N> represents the approximate number of absorbed photons per QD. The last two rows are the fit results for the TRPL data from Section 4.1.1.

	A1/A2	C1 (ps)	C2 (ps)
Zn <N> = 600	4.13 ± 0.25	222 ± 14.2	6283 ± 738
,Zn <N> = 230	8.7 ± 3.5	72.4 ± 25.5	1405 ± 531
Se <N> = 230	6.4 ± 0.7	96.1 ± 9.9	3300 ± 623
TRPL	1.59 ± 0.02	747 ± 14	10,000 ± 130

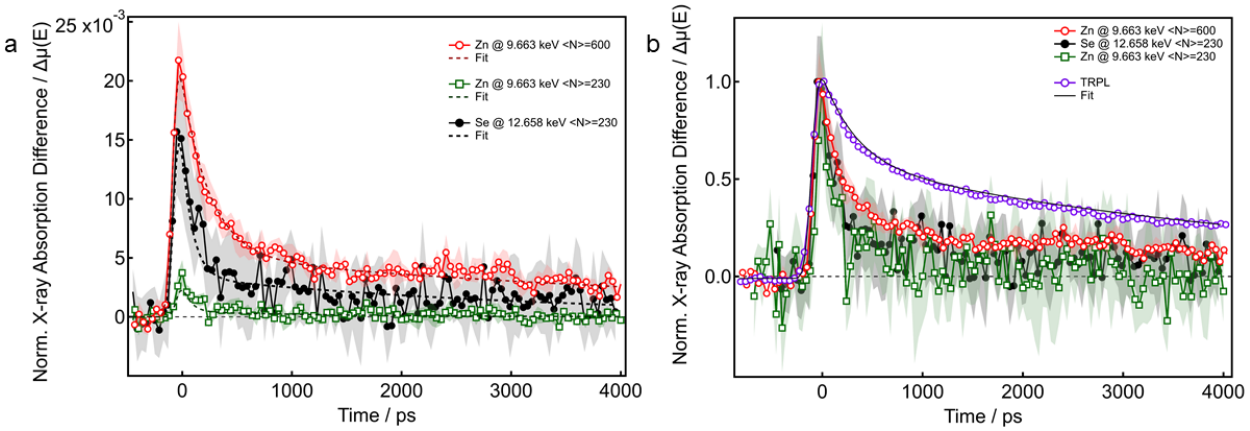

Figure 6.4: Kinetic traces at the first peak of the maximum XTA signal after photoexcitation at 532 nm for ∽230 absorbed photons/QD at the Zn K-edge (green) and the Se K-edge (black) and a∽600 photons/QD at the Zn K-edge (red). The dashed lines represent bi-exponential fits yielding the parameters in Table 6.1. (b) The kinetics normalized to 1 compared to the TRPL decay at 535 nm excitation.

6.2 Heat diffusion simulations

The absorption of photons by a material inevitably leads to an increase in its temperature. There are a number of processes and time scales involved in the thermal energy generation and subsequent dissipation.[83] Above-gap optical excitation generates hot carriers (electrons, holes or both). Exciton screening and electronic band-gap renormalization (BGR), usually on the order of meV, occurs in under a ps after photoexciation (see Section 6.3 for more details).[207] The hot carriers can also scatter to yield lattice vibrations within the nanomaterial via intraband relaxation by single- or multiphonon interactions.[208,209] Typically within 100 fs, electron-electron scattering results in electrons that energetically obey Fermi-Dirac statistics, and as such they can be described by an electron temperature. At higher fluences, production of multiple excitons leads to Auger recombination, where an electron-hole pair recombines by exciting another charge that subsequently undergoes intraband relaxation. Heating can occur as a result of Auger recombination due to transfer of potential energy to the remaining charge, which subsequently cools generating phonons.[83] In a few picoseconds after photoexictation, hot carriers also undergo intraband cooling;[210,211] though in some

CSQDs, slow intraband relaxation (>1 nanosecond) has been reported.[212] Intraband cooling occurs through electron-phonon coupling, in which the scattering of electrons from lattice sites dissipates energy in the form of one- or multiple-lattice phonons. This coupling thereby raises the effective vibrational temperature until both lattice and charge carriers achieve quasiequilibrium, resulting in a temperature above that of the thermal bath.[213] The energy bandgap of semiconductors tends to decrease as the temperature is increased due to increase in interatomic spacing as a result of increased atomic vibrations increases due to the increased thermal energy.[214–216] Disordering or melting of the nanoparticles can result from phonons exchanging energy between modes at high enough lattice temperatures.[110] The mechanism of heat diffusion in nanoparticles with large surface-to-volume ratios are typically diffusive or interfacially limited via phonon-phonon coupling with the surrounding environment. When nanoparticles are coated with an electrically insulating ligand shell, significant contributions from charge-carriers in heat transport are not expected.

The maximum temperature of QDs after laser absorption is mainly determined by the laser fluence, the excess energy above the band gap, and the heat capacity of the material. To establish a rough estimate of the temperature profile of our CSQDs after laser

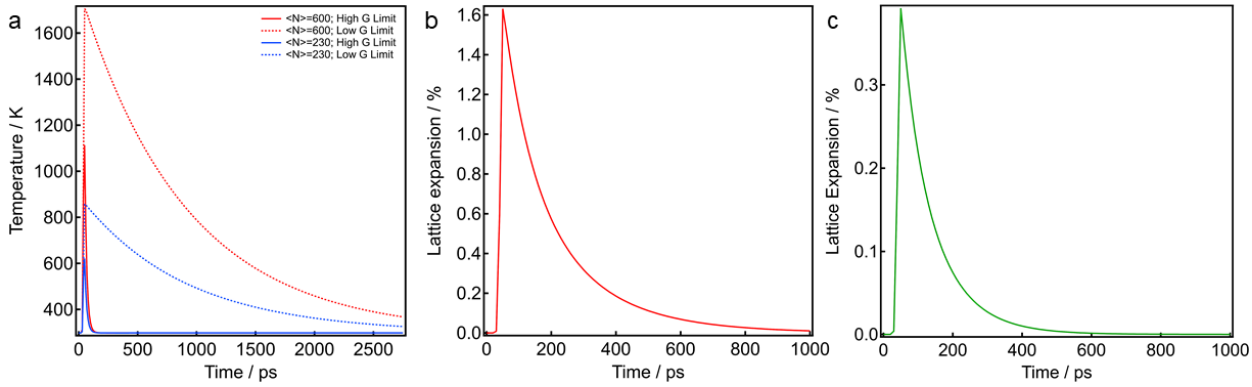

Figure 6.5: (a) The temperature profiles of the QD solution after laser excitation. The red curves represent the higher fluence (∽600 absorbed photons/QD) and the blue curves represent the lower fluence (∽230 absorbed photons/QD). The solid curves are associated with the high G value for a hexane/hexylamine/CdSe interface and the dashed lines are associated with the low G value of a bare hexane/CdSe interface.[170] The decay times range from 20 ps to 1.4 ns. (b) Predicted lattice expansion profile for the QDs under the high (a) and low (b) fluence conditions.

excitation, the heat equation[169] is solved as described in Section 3.8. Here we consider a pure CdTe QD, since the thermal properties of CdSe, CdTe and ZnTe are all similar.[146] For simplicity, we do not include any non-linear photon absorption effects, and we expect heat diffusion between the $Cd_xZn_{1-x}Te$ core and CdSe shell to be fast compared to heat diffusion between the nanoparticles and the surrounding. The boundary condition of the heat equation is determined by the interfacial thermal conductance, G. The interfacial thermal conductance is a measure of how efficiently heat carriers flow from one material to another. This nanoparticle/ligand/solvent interface, however, is difficult to access experimentally. Currently, estimates of interfacial thermal conductance for QDs and their surroundings are based on effective medium theory calculations[217,218] or characterization of thermal transport rates via optical spectroscopy.[209] Due to the complex nature of quantum dot surfaces and limited studies in the literature, we used a range of G values in the literature to estimate a possible range in temperature profiles for the QDs in our system. We use two G values from the literature as extremes: 90×10^6 W/m^{2}K which describes a hexane/hexylamine/CdSe interface (*i.e.* a CdSe with complete ligand coverage in a nonpolar solvent) and 3.6×10^6 W/m^{2}K, which is a bare hexane/CdSe interface.[170] The time scale of heat diffusion depends mainly on the interfacial thermal conductance as shown in Figure 6.5a. The absolute magnitude of the temperature jump is overestimated in the thermal profiles presented in Figure 6.5a and they are not in agreement with the data, as shown later in Section 6.4, which may be due to non-linear absorption effects or photochemical energy decay processes.[112] This difference between is also compounded likely due to having only a very rough estimate of the absorption cross section and nanoparticle concentration. Based on the two extremes, however, we can infer that heat dissipation occurs in tens to hundreds of ps timescale. The short decay time of the XTA signals, C1 in Table 6.1, falls in this range for all data sets. Furthermore, the similar C1 decay constants at both the Se and Zn edges also indicate that we are observing the same process, so we assign the C1 decay to the interfacial heat dissipation in the colloidal nanoparticle solutions. The long decay constant, C2 in Table 6.1,

is assigned to the electron-hole recombination, as the ns timescale is in agreement with the short decay time of the TRPL data. The long decay of the TRPL is not measurable in the XTA data given the small amplitude and limited time window in XTA experiments. We also note that a pure multiexponential decay is not expected, but rather a distribution of decays, or stretched exponential decay.[219]

With the established range of possible temperature profiles and the short decay constant assigned to heating, we can estimate for lattice expansion profiles for the QDs under the laser fluence conditions. To do this, we use the short decay time from the XTA signal to estimate the G values for the nanoparticle solutions, yielding $\backsim$7 MW/m^2/K and $\backsim$15 MW/m^2/K at the high and low laser fluences, respectively. Using the temperature profile for the Gvalues, we roughly estimate the lattice expansion profiles using the thermal expansion coefficient for bulk CdTe,[220] , shown in Figure 6.5 b and c. We will show later in Section 6.4 that the lattice expansion derived from the simulated XTA spectra is about a factor of 5-8 smaller than predicted by these simple heat diffusion simulations. This discrepancy may be due to non-linear absorption effects or photochemical energy decay processes that do not lead to heating.[112]

6.3 Electronic and thermal effects in XTA spectra

This section serves to provide the necessary background of the main effects in XTA spectra of semiconducting materials resulting from both electronic and thermal photoexcitation.

Changes in pre-edge absorption intensity Pre-edge features are a result of bound-bound transitions, which can be formally forbidden by selection rules in XAS. Orbital mixing and quadrupolar coupling, however, allows for weak spectroscopic signatures to appear before the ionization edge. The emergence or disappearance of pre-edge transitions gives information about the change in hybridization and bonding in the vicinity of the absorbing atom. While no pre-edge features are present in the Zn and Se K-edge spectra presented

here, they are observed for every first row transition metal whose 3d orbital is not fully occupied. Several examples of transient pre-edge features exist in the literature.[90,96,221–225]

Ionization edge shifts An edge shift typically appears as a derivative-like feature in the transient XANES spectrum; either as a red shift (decrease in ionization edge energy) or a blue shift (increase in ionization edge energy). There are four possible origins for edge shifts or edge-shift like effects in XTA spectra: **(1)** Oxidation state changes are most commonly responsible for edge shifts.[92–94,96,97,99,100,221–225] An oxidation state change means that the ionization potential for the atomic core orbital increases or decreases in energy due to (partial) oxidization or reduction, respectively. As the oxidation-state increases, the energy of the ionization edge also increases as more energy is required to excite a core electron because the nucleus is less shielded and has a higher effective charge. Therefore, a red-shift is expected for an absorbing atom gaining electronic density after photoexcitation, whereas a blue shift can mean a loss of electronic density. Photoinduced electron transfer has been inferred from XTA data for molecular systems[92,96,97,226–232] as well as solids.[90,93,233,234] **(2)** Changes in bond length between an absorbing atom and its neighbors can cause edge shifts.[98,197,235–237] Structural changes can result from the population of excited states that lead to bond dilation or contraction,[87–89,97,226–228,230,238–244] or carrier trapping leading to local lattice distortions called polarons[100,245] In addition, bond length changes (expansion, contraction) can also be the result of the population of vibrational/phonon modes at elevated temperature. In fact, in semiconductors, so-called thermal band gap shrinkage has three contributions: (a) thermal lattice expansion; (b) thermal disorder (called the "Debye-Waller" term); and (c) a polaronic self-energy term, which is almost negligible.[246,247] The decrease in the band gap results in a shift of the conduction band to lower energy and thus a lower ionization edge energy and red shift of the XANES spectrum. **(3)** In metal or semiconductor materials, band filling or emptying of states can cause apparent edge shifts.[85,100,236] A reduction of intensity right above the edge can reflect the filling of unoccupied states, similar to the Burstein-Moss

shift (BMS) found in optical studies of semiconductors.[207,248,249] An increase in absorption just below the edge can be due to the induced absorption into photocreated holes in the valence band.[85] A simple shift of the entire edge is only an approximate phenomenological way to incorporate these induced absorption and bleach effects in XTA spectra. A more elaborate theory incorporating the excited carrier densities and temperatures is needed to determine the energy dependence of these effects. Finally **(4)**, the excited electrons can screen the electron-electron interaction which leads to a band gap narrowing that counteracts the widening due to the BMS. This effect is called band gap renormalization (BGR).[207,248,249]

Shifts and dampening of above-edge oscillation features Above-edge transitions probe the unoccupied density of states above the Fermi level. The higher the energy, the more delocalized the states become, and eventually once can interpret the features in the framework of (multiple) scattering of quasi-free electrons in the local vicinity of the absorbing atom. In general, therefore, higher-energy features $>\backsim$ 30 eV above the edge are assigned to multiple-scattering resonances with a structural origin. Indeed, it has been commonly observed that such features shift proportionally to expanding and contracting the local bond distances surrounding the absorbing atom, which is known as Natoli's rule.[197,235] Similar as in the case of EXAFS spectroscopy, we therefore expect thermal disorder in the lattice to appear as a dampening of the multiple-scattering features. An approximate way to incorporate such dampening is by multiplying the XANES spectrum by an exponential decay function, a "Debye-Waller (DW) factor," in analogy to EXAFS spectroscopy.[118] More elaborate theories for calculating DW factors for XANES spectroscopy have emerged in recent years.[250–253]

6.4 XTA spectra simulations

Large changes are observed in both the XANES and EXAFS regions at the Zn edge upon photoexcitation. On the other hand, we observed a simpler derivative like shape in the XTA spectrum at the Se edge (Figure 6.3). Due to its richer structure and interesting spectral

evolution as a function of time delay, we focus on the Zn K-edge data in this analysis. In Figure 6.6 we show the same data as in Figure 6.2a, but the spectra are scaled to the peak at 9663.0 eV. The difference in the relative amplitude at the two bleach features at 9666 and 9673 eV are highlighted with arrows. The relative ratio of the amplitudes at these bleach features changes when we compare the spectra measured at ∼90 ps versus ∼2.5 ns delay, and we are particularly interested in understanding the origin of these spectral changes.

In this section, we simulate the excited state spectra and compare the simulated difference spectra to the experimental difference spectra. We used the spectrum from Chapter 5 as the ground state spectrum, and the XAS simulations are performed using the alloyed supercells presented in Chapter 5. Out-of-equilibrium spectra were generated by varying three parameters: (1) isotropic expansion and contraction of the supercell used as an input structure for the FDMNES program, (2) the extent of thermal dampening incorporated as an exponential DW $e^{-2k^2\sigma^2}$, where k is the wavevector and σ^2 is the atomic mean-free displacement, (3) a rigid shift of the whole XAS spectrum to lower or higher energies, after applying the changes in (1) and (2). While applying the lattice expansion/contraction we encountered an instability of the convergence of the SCF cycle implemented in FDMNES,

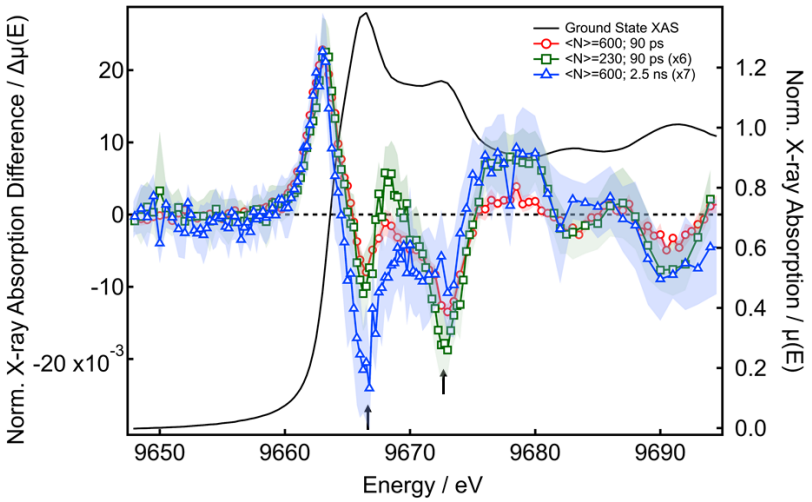

Figure 6.6: Experimental ground-state XAS (black, right axis) and transient XANES after photoexcitation with 532 nm pulse. Same data as in Figure 6.2a, but the spectra are scaled to the peak at 9663.0 eV. The difference in the relative amplitude at the two bleach features at 9666.2 and 9673 eV are highlighted with arrows.

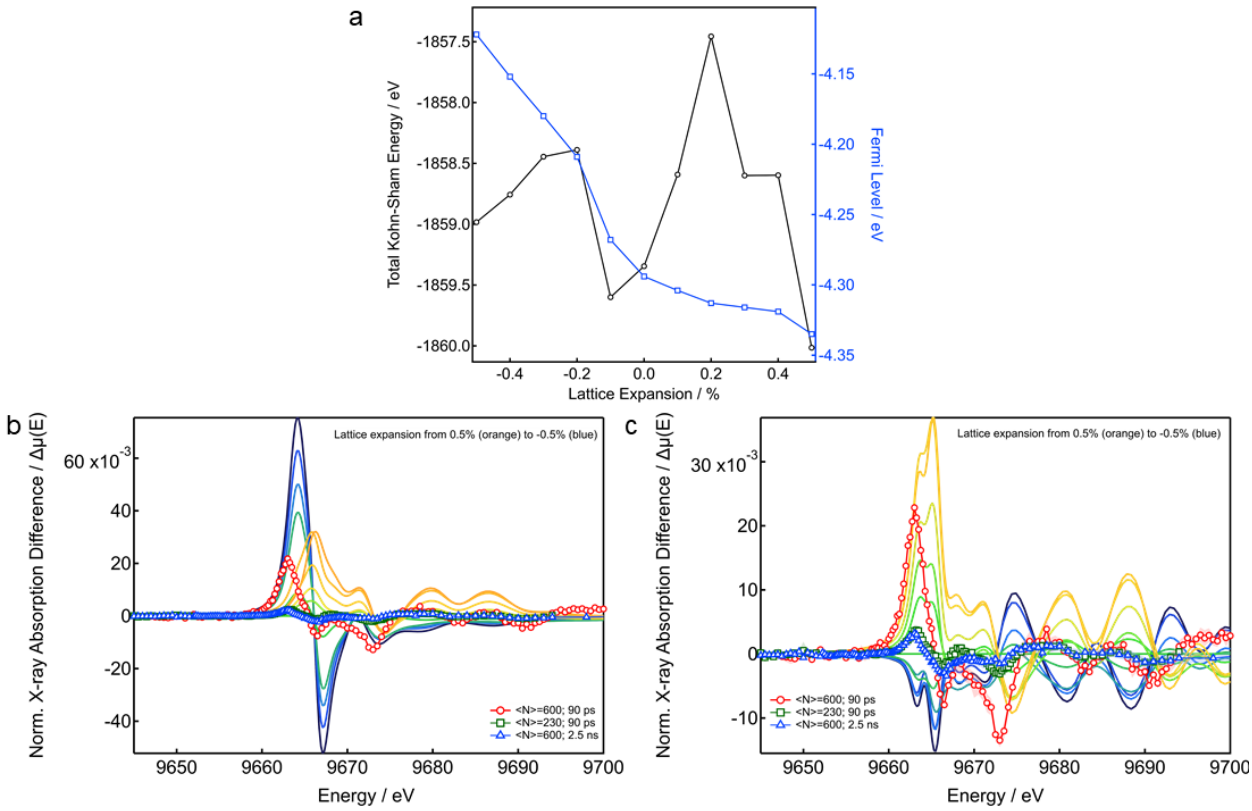

Figure 6.7: (a) SCF converged Kohn-Sham energy (black circles) and Fermi level (blue squares) from the SCF cycle as implemented in FDMNES with respect to the lattice contraction/expansion. (b) and (c) Comparison between the Zn K-edge experimental XTA spectra and the simulated difference spectra of the $Cd_xZn_{1-x}Te$ supercell with a lattice expansion from +0.5% to -0.5%.(b) Before Fermi level alignment procedure. (c) After Fermi level alignment procedure.

shown in Figure 6.7a. As in the case of standalone DFT codes, we expect a parabola-shaped dependence of the total energy as a function of lattice expansion/contraction with the minimized energy at the ground state (0% lattice expansion) lattice parameter.[254] The exact origin of these convergence issues is not known at present, but they may be related to the fact that FDMNES is based on a real-space, cluster DFT implementation, while standalone codes are mostly using reciprocal-space calculations. Similar issues were observed at the Zn K-edge calculations for ZnO (data not shown), while for other materials such as PbSe (Se K-edge) such problems were not encountered.

In order to correct for the convergence instabilities in an *ad hoc* manner, we perform a post-processing alignment of the Fermi energies prior to convolution of the spectra. The

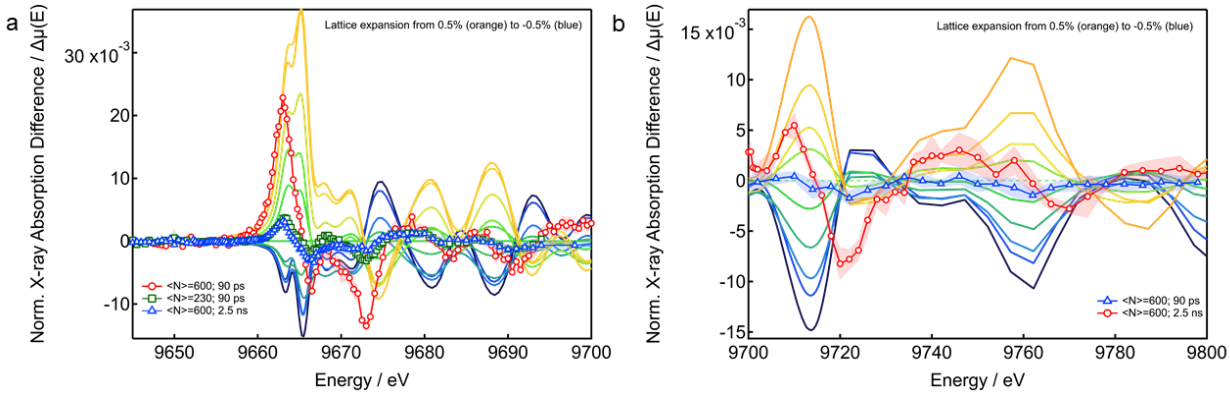

Figure 6.8: Comparison between the Zn K-edge experimental transient XANES (a) and EXAFS (b) spectra and the simulated difference spectra of the $Cd_xZn_{1-x}Te$ supercell with a lattice expansion from +0.5% to -0.5%. The energy axis of simulated XANES spectra in (a) is scaled by 8.3% (see Chapter 5 for details).

alignment of the Fermi levels is performed such that all the Fermi levels become equal to the ground state Fermi level (without lattice deformation). We observe a substantial improvement in the curve-to-curve evolution for consecutive lattice distortions, as shown in the comparison between Figure 6.7a, before the alignment, and Figure 6.7b, after the alignment. After alignment, the post-edge region (Figure 6.8b) shows clear isosbestic points around zero and the magnitude of the transient is about a factor of two smaller than before alignment of the Fermi energy. This procedure is only an approximate way of correcting for

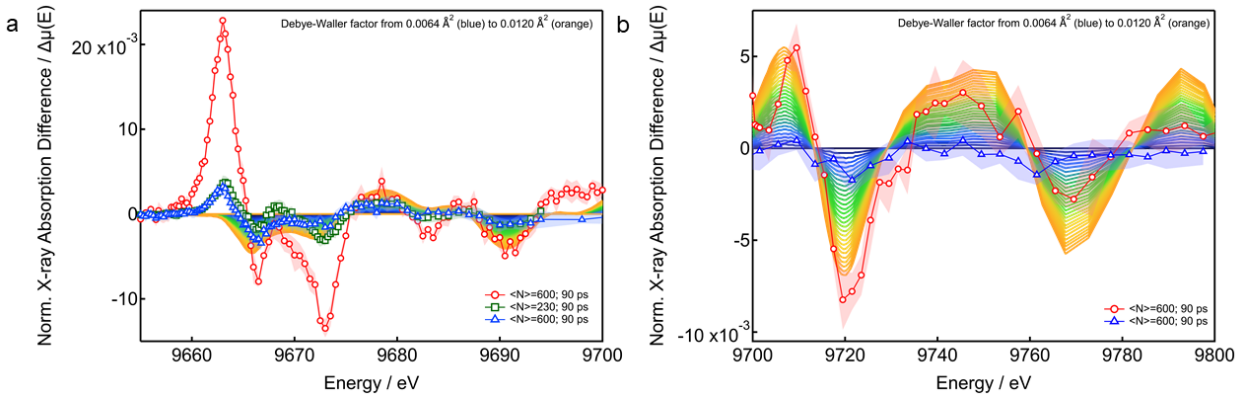

Figure 6.9: Comparison between the Zn K-edge experimental transient XANES (a) and EXAFS (b) spectra and the simulated difference spectra of the $Cd_xZn_{1-x}Te$ supercell with a DW factor from $\sigma^2 = 0.0064$ Å^2 to 0.0120 Å^2. The energy axis of simulated XANES spectra in (a) is scaled by 8.3% (see Chapter 5 for details).

the instability in the convergence. A suggestion to avoid this problem could be to import the potentials from a stand-alone DFT code. Currently, FDMNES is not equipped to import potentials from VASP, the DFT code used in this work, but FDMNES is configured to import potentials from Wien2k, another stand-alone DFT code. While some features are qualitatively reproduced for an expansion of the lattice, several spectral variations, such as the bleach features around 9665-9675 eV, are not reproduced by the simulations. Clearly, lattice distortions alone cannot account for the spectral changes observed.

In addition to lattice expansion, we simulated thermal disorder by changing a dampening DW factor that is applied to the spectra in the convolution step. In Figure 6.9 we show the simulated difference spectra starting with the DW factor of $\sigma^2 = 0.0064$ Å^2, as determined by EXAFS fitting in Section 4.2, and varying it up to $\sigma^2 = 0.0120$ Å^2. In particular in the EXAFS region, the XTA signal can be represented very well by the spectral dampening. Finally, an edge shift was simulated by subtracting a shifted ground state spectrum from an unshifted spectrum, with shifts ranging from -50 to +50 meV, as shown in Figure 6.10. The largest positive XTA feature at ∼9666 eV is represented well by a red shift of the spectrum, while the EXAFS region is not affected much. As discussed in the previous section, an ionization edge shift can have thermal or electronic origins.

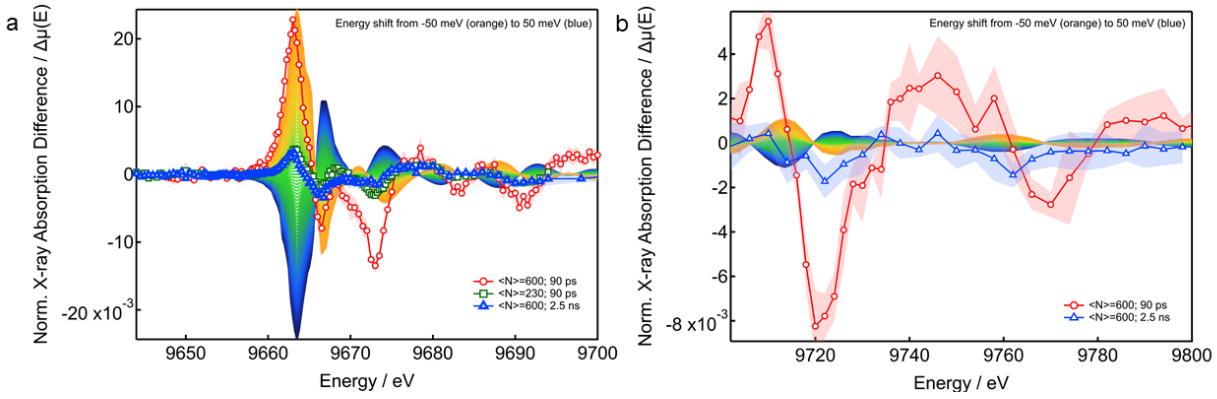

Figure 6.10: Comparison between the Zn K-edge experimental transient XANES (a) and EXAFS (b) spectra and the simulated shifted difference spectra of the $Cd_xZn_{1-x}Te$ supercell for energy shifts ranging from -50 meV to +50 meV.. The energy axis of simulated XANES spectra in (a) is scaled by 8.3% (see Chapter 5 for details).

Table 6.2: Summary of the best combination of the three parameters for each of the three experimental conditions.

Photons/QD (<N>)	Time	Lattice expansion	Edge shift (meV)	DW factor (Å^2)
600	90 ps	0.2%	-10	0.0102
600	2.5 ns	0.0%	-10	0.0076
230	90 ps	0.03%	-4	0.0092

,

6.4.1 Combined models

While the simulated differences of DW factor seem to agree with the experimental XTA spectra in the EXAFS region (Figure 6.9b), the changes near the edge cannot be singly attributed to any one of the three effects (lattice expansion, DW dampening, edge shift). We therefore compute difference spectra by combining all three parameters in a semi-quantitative fashion. First, we apply the range of DW factors (σ^2 = 0.0064 Å^2 to 0.0120 Å^2) to each expanded lattice spectrum (-0.5 to +0.5%). Then, after applying the Fermi level alignment procedure, we simulate a range of spectral shifts. The results of the best combination of the three parameters for each of the three experimental conditions in the XANES region are shown in Figure 6.11. In Figure 6.12, we show results of the best combination of the three parameters for the two experimental conditions in the EXAFS region. The "best-fit" parameters are summarized in Table 6.2.

We note that we are not seeking a quantitative agreement between simulation and experiment due to significant theoretical errors and the approximate way we incorporate complex phenomena such as excited-state band filling and emptying or thermal disorder. Given these approximations, the agreement is satisfactory. In particular for the high-fluence data sets, the changing ratio between the two bleach features around 9665-9675 eV is well reproduced in the simulation.

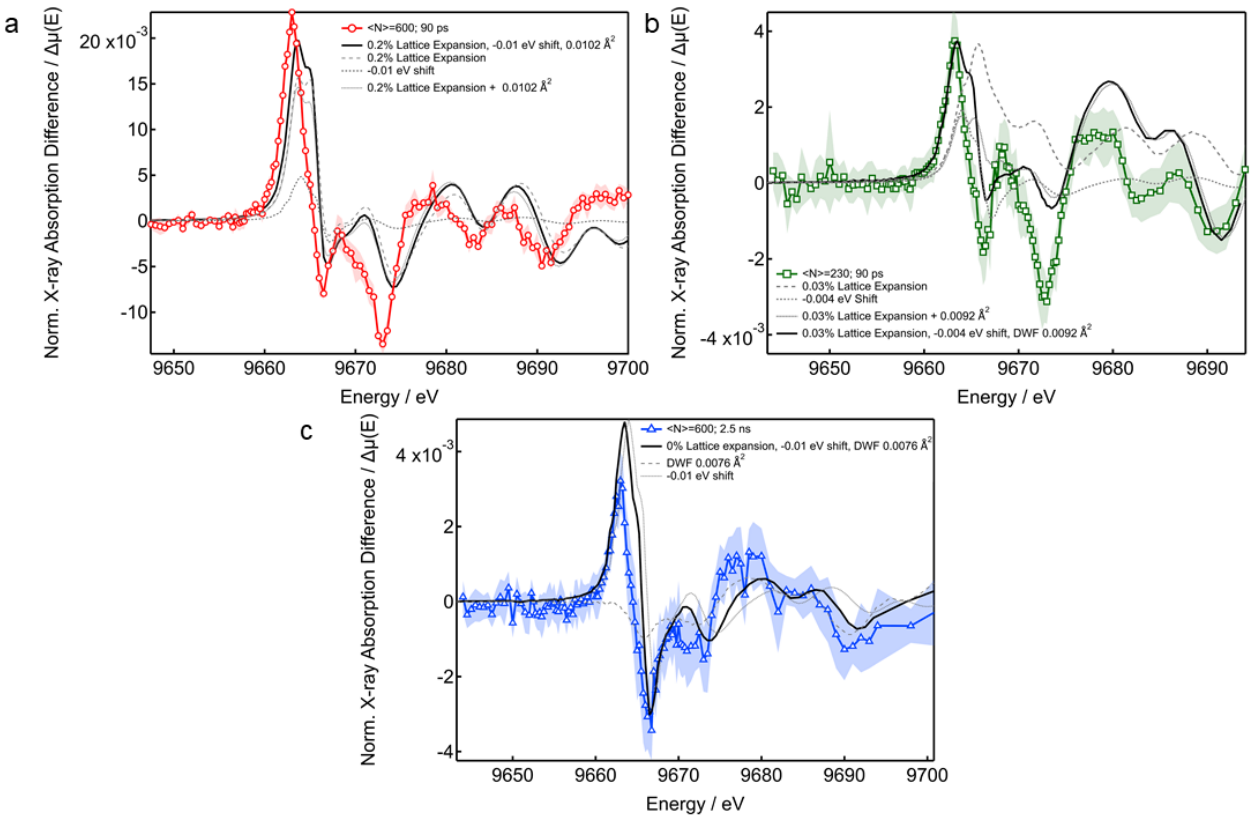

Figure 6.11: XANES difference spectra compared to the simulated difference spectra of the three excited states. Transient XANES spectra after photoexcitation with 532 nm at same three experimental conditions as Figure 6.2a are shown. (a) 0.2% lattice expansion, DW factor increase to 0.0102 Å^2 and a red shift of 10 meV; (b) 0.03% lattice expansion, DW factor increase to 0.0092Å^2 and a red shift of 4 meV; (c) no lattice expansion, an increase of DW factor to 0.0076 Å^2 and a red shift of 10 meV. The energy axis of simulated XANES spectra is scaled by 8.3% (see Chapter 5 for details). The individual effects on the spectra are shown with gray lines.

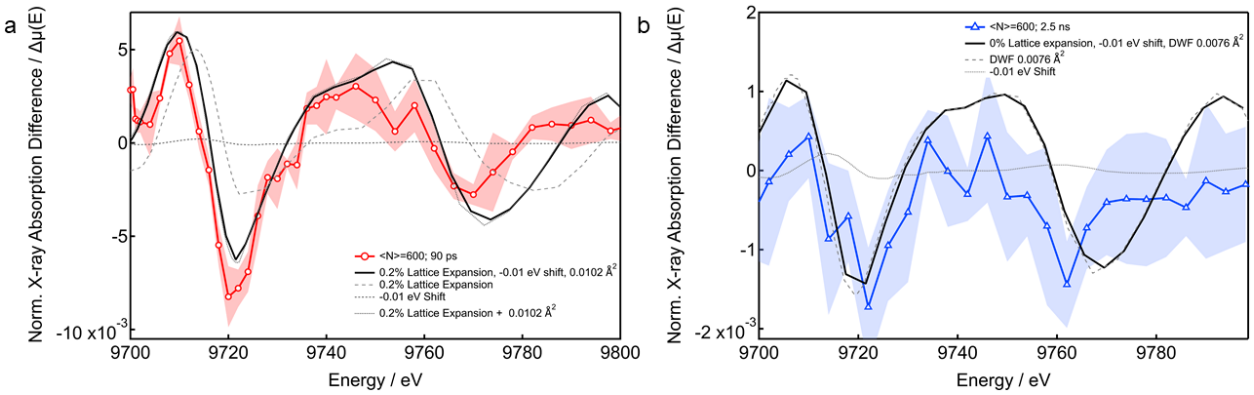

Figure 6.12: EXAFS difference spectra compared to the simulated difference spectra for the two excited states. Transient EXAFS spectra after photoexcitation with 532 nm at same experimental conditions as Figure 6.2b are shown. (a) 0.2% lattice expansion, DWF increase to 0.0102 Å^2 and a red shift of 10 meV; (b) no lattice expansion, an increase of DWF to 0.0076 Å^2 and a red shift of 10 meV.

6.5 Discussion

At ∼90 ps delay at at high laser fluence, we derived a lattice expansion of ∼0.2% and a ∽50% increase in DW factor compared to the ground state spectrum. At 2.5 ns, the lattice is no longer expanded and a 20% increase in DW factor remains. As demonstrated by the simulated difference spectra in Figure 6.12, the EXAFS region is mainly affected by the lattice expansion and DW factor change, with very little effect of the spectral shift. We noticed that lattice expansion values derived from the simulated XTA spectra are about an order of magnitude smaller than the lattice expansion values we predicted in Section 6.2 using simple heat diffusion simulations. This difference is likely due to the approximations and assumptions made in estimating the absorbed laser fluence, such as neglecting non-linear absorption and having only a very rough estimate of the absorption cross section and nanoparticle concentration. Based on the ∼0.2% expansion, the maximum estimated temperature jump in the nanoparticles is ∽300 K.

The XANES region is more complicated as all three parameters influence this region. The lattice expansion and spectral shift mainly contribute to the region around the white line, whereas the DW factor mostly influences the features above the white line and in

the EXAFS region. Interestingly, while large thermal effects such as lattice expansion and DW dampening are clearly dominating the XTA spectrum at ∼90 ps, at ∼2.5 ns no lattice expansion is observed and the DW factor is largely reduced. The edge shift necessary to satisfactorily represent the data is in both cases ∼10 meV. The finding that heat is dissipated within this time window is in agreement with Kirschner *et al.*, where CdSe QDs were pumped with a 100 fs laser at 400 nm under similar fluences and experimental conditions (liquid jet, similar nanoparticle sample, solvent, and concentrations) and where time-resolved XRD showed that the lattice had cooled within ∼1 ns.[110] The ∽ 10 meV edge shift can have thermal or electronic origins. Thermal band gap shrinkage is typically dominated by lattice expansion and thermal disorder effects, which are included separately in our analysis. The third contribution to thermal band gap renormalization, namely polaronic self energy effects, has been claimed to be negligible in the literature.[246,247] We therefore conclude that the ∼10 meV edge shift to lower energies is due to electronic phenomena. The reduced values for the lattice expansion, edge shift, and DW factor for the low-fluence, ∼90 ps data set are in qualitative agreement with this picture.

As discussed in Section 6.3, the apparent edge shift can originate from electronic BGR and/or band filling and emptying. At the Zn K-edge, we primarily probe empty Zn 4p orbitals. The DOS in the valence band of ZnTe is primarily composed of Te 5p orbitals, but Zn 4p orbitals contribute up to ∼10% as well.[255] The conduction band, on the other hand, is largely composed of Zn s-orbitals, with appreciable contributions from Zn and Te p-orbitals. The Zn 4p contributions throughout the DOS of the valence and conduction bands therefore renders the Zn K-edge spectrum sensitive to both excited electrons and holes. We thus we expect band emptying, (*i.e.* the opening of holes in the valence band to appear as an induced absorption on the low-energy side of the edge), and band filling, (*i.e.* the occupation of electrons in the conduction band to appear as a depleted absorption (bleach) on the high-energy side of the edge). The overall result may appear as a red shift of the near-edge XAS spectrum, as observed in our data. The energy dependence of these filling/emptying effects

have been neglected here. Electronic BGR may have very similar effects on the spectra, and is expected to be in the meV range.[85,207] Our data does not allow us to disentangle BGR and band filling/emptying. We note that while thermal and electronic effects are heavily entangled at early time delays (∼90 ps), the transient XANES spectrum at later ∼ns times is dominated by electronic effects. In conjunction with performing heat diffusion simulations, and by means of selecting the appropriate time scales for measuring XTA spectra, one can thus minimize thermal effects in XTA spectroscopy on nanomaterials.

6.6 Conclusions

In this study, we demonstrate that under excitation conditions prevalent in XTA experiments on solids and nanomaterials the thermal response has a large contribution. Through simulation of the effects of lattice expansion and disorder parameters, we can simulate the thermal effects of photoexcited nanomaterials in a semi-quantitative fashion. With the thermal effects determined, we are able to quantify the contribution of long-lived electronic effects in the spectra. Finally, we show that with the right procedures in place, XTA can be used to characterize materials under high-carrier injection conditions and to estimate the heat interface conductance in colloidal nanomaterial samples.

Knowledge of the interplay of the thermal and electronic processes in photoexcited nanomaterials is important for improving the overall performance of next generation optoelectronic devices. Thermal effects in XTA have only recently been considered as a possible contribution to XTA signals[112,113] and current literature lacks methods for disentangling the effects of both electronic and thermal dynamics in nanoparticles. The high fluences necessary for these experiments make it such that thermal effects are necessarily part of XTA spectra on solids and nanomaterials. These thermal phenomena are interesting on their own given that many optoelectronic devices must operate under large thermal loads.[82] While the sensitivity of XTA to study electronic and thermal effect can be advantageous,

the question arises what experimental conditions are needed to study electronic effects in the single exciton excitation region. Several possible experimental approaches exist to answer this question. Future studies may need to be designed to systematically and carefully measured static temperature-dependent XAS,[112] to go to shorter time scales (*e.g.* using X-ray free electron lasers[224,236,237,256] or table-top X-ray sources[85]), to tailor the surface of nanomaterials for improved thermal conductance,[170,173,257] and to separate absorber from acceptor material.[91,92,94,96,258–267] High-repetition rate data acquisition schemes, in conjunction with high-speed liquid jets are required to improve signal-to-noise ratios for low laser fluence conditions.[168]

Chapter 7

Conclusions and future outlook

Quantum dots (QDs) have sparked a revolution in nanoscience, and due to their unique and easily tunable properties, they have a bounty of potential applications in solar energy harvesting, biomedical imaging, photocatalysis, light emitting devices, and quantum computing.[1–3] In order to bring the next generation of devices to fruition, techniques which allow scientists to visualize the journey of charge carriers in semiconductors after photoexcitation are highly sought after. X-ray absorption spectroscopy (XAS) offers many advantages for its element specificity and combined local electronic and structural sensitivity. The excitation process of laser pump/X-ray probe experiments occurs on the timescale of billionths of a second — the "ultrafast" timescale. Within this brief time, charge carriers can get trapped or recombine within the materials of interest. Our experiments at the Advanced Photon Source synchrotron at Argonne National Laboratory allow us to capture "snapshots" with X-rays less than 100 ps after laser excitation. These snapshots help us better understand how our QDs respond to light and how we can address the inefficiencies that arise in QD based optoelectronic devices. In this thesis we applied use a multitude of static and ultrafast characterization tools to determine the internal atomic-scale structure, band alignment, and dynamics of $Cd_xZn_{1-x}Te$/CdSe core/shell quantum dots. This thesis in particular highlights the power of XAS for understanding the internal structure and photothermal dynamics of heterogeneous nanoparticles.

7.1 Internal structure determination of heterogenous nanoparticles

In Chapter 4, we determined the internal structure of II-VI CSQDs using a multimodal characterization. We showed that the intended ZnTe/CdSe CSQDs, that are synthesized using a common one-pot synthesis procedure, are in actuality nanoparticles with an alloyed core and a patchy CdSe shell. Through electronic structure calculations we show that they essentially behave as one-component QDs with a direct band gap. Cation exchange and the unintended reaction of molecular precursors prevent the formation of a sharp type-II ZnTe/CdSe interface with small lattice mismatch. Instead, the large interfacial strain between $Cd_xZn_{1-x}Te$ ($x \backsim 0.8$) and pure-phase CdSe leads to the growth of islands on the QD surface. Our results corroborate the challenges associated with the synthesis of Zn/Cd chalcogenide type-II heterostructures due to facile ion exchange. We emphasize that the assessment of heterogeneous nanomaterials on the basis of spectroscopy or size analysis alone is not always sufficient. We utilized EXAFS spectroscopy as an element-specific technique for the internal structure determination of heterostructured nanomaterials. By simultaneously fitting the local atomic structures at the ionization edges of all four elements in the sample in combination with standard materials characterization, we were able to propose models for the internal nanoparticle structure. While our XAS data were obtained at a large-scale synchrotron X-ray facility with specialized infrastructure and limited access, the advent of tunable high-brightness table-top X-ray sources will enable similar studies on heterostructured photovoltaic and photocatalytic nanomaterials with much higher throughput and more experimental flexibility.[184]

7.2 Ground state XANES analysis

While we demonstrated the power of EXAFS for the structural determination of heterogeneous materials, one limitation in our case was that the EXAFS data in only probed the first-shell bond lengths due to the disorder present in the $Cd_xZn_{1-x}Te$/CdSe CSQDs. XANES, however, is sensitive to local electronic structure and long-range multiple scattering effects (up to ~ 10Å from the absorbing atom).[70] XANES also is less affected by structural disorder relative to EXAFS, the interpretation of which becomes more complicated with highly disordered materials, like nanomaterials.[70–74] XANES is a powerful tool for probing the electronic and geometric structure around an absorbing atom due to the sensitivity of the near-edge region to the surroundings of the absorbing atom. The interpretation of XANES spectra has come a long way from the qualitative fingerprinting approach of comparing the data with the spectra of model compounds[125,126] to a quantitative or semi-quantitative probing tool to determine the structure of molecules in solution,[127–129] bulk solids,[130] or heterogeneous nanomaterials.[131] Analysis and simulation of XANES has made a significant contribution to the identification of the occupation sites of dopants in nanostructured semiconductors.[75–81]

In Chapter 5, we implemented *ab initio* XANES simulations as a way to corroborate the structural characterization of the alloyed $Cd_xZn_{1-x}Te$ core in Chapter 4. We employed density functional theory (DFT) to relax a supercell of a representative $Cd_xZn_{1-x}Te$ (x=0.8) alloy. The supercell is used as an input structure in Finite Difference Method Near Edge Spectroscopy (FDMNES) program, the DFT-based X-ray spectroscopy simulation code used in this work. The simulation of the XANES spectrum of the alloy supercell is in agreement with the experimental spectrum. Due to difficulty in controlling the synthesis of the alloy and limited access to large-scale X-ray facilities, we were not able to experimentally determine which features in the XANES spectrum are a result of alloying. Through simulation, however, we easily varied the composition of the supercell and showed via simulation which XANES features may be due to alloying. Together, Chapters 4 and 5 showcase the power of XAS, in

both experiment and simulation, for understanding the internal structure of heterogeneous nanoparticles.

7.3 X-ray transient absorption spectroscopy

Finally in Chapter 6, we demonstrate that thermal effects have an important contribution to XTA signals conditions typical of XTA experiments on solids and nanomaterials. We were able effectively separate the contributions of thermal and electronic effects through simulation of XAS spectra of the photoexcited $Cd_xZn_{1-x}Te$/CdSe CSQDs. We simulated thermal effects through lattice expansion and disorder parameters in a semi-quantitative fashion. With the thermal effects determined, we are able to quantify the contribution of long-lived electronic effects in the XTA spectra. We also showed that XTA can be used to characterize colloidal nanomaterial samples under high-carrier injection conditions and to estimate the heat interface conductance of such materials.

Thermal phenomena present in the high-carrier injection conditions are important to understand on a fundamental level because many optoelectronic devices must operate under large thermal loads.[82] The contribution of thermal effects in XTA experiments on colloidal nanomaterials and thin films, however, have only been considered recently.[112,113] In this thesis, we present a method for disentangling the effects of both electronic and thermal dynamics in nanoparticles. This method is a pivotal contribution to the field because high fluences are currently necessary for these experiments and as such thermal effects inevitably affect XTA spectra on solids and nanomaterials. Future studies may be designed to circumvent thermal effects all together either by systematically and carefully measuring static temperature-dependent XAS,[112] measuring at shorter time scales before thermal effects emerge (*e.g.* using X-ray free electron lasers[224,236,237,256] or table-top X-ray sources[85]), tailoring the surface of nanomaterials for improved thermal conductance,[170,173,257] and/or separating the absorber from acceptor material.[91,92,94,96,258–267] High-repetition rate data acquisition schemes, in con-

junction with high-speed liquid jets are required to improve signal-to-noise ratios for low laser fluence conditions in colloidal materials.[168]

Bibliography

[1] A. J. Nozik, M. C. Beard, J. M. Luther, M. Law, R. J. Ellingson and J. C. Johnson, Semiconductor Quantum Dots and Quantum Dot Arrays and Applications of Multiple Exciton Generation to Third-Generation Photovoltaic Solar Cells, year = 2010, *Chemical Reviews*.

[2] Y. Shirasaki, G. J. Supran, M. G. Bawendi and V. Bulović, Emergence of colloidal quantum-dot light-emitting technologies, *Nature Photonics*, 2013, **7**, 13–23.

[3] X. Gao, Y. Cui, R. M. Levenson, L. W. K. Chung and S. Nie, In Vivo Cancer Targeting and Imaging with Semiconductor Quantum Dots, *Nature Biotechnology*, 2004, **22**, 969–976.

[4] B. K. H. Yen, A. Günther, M. A. Schmidt, K. F. Jensen and M. G. Bawendi, A Microfabricated Gas-Liquid Segmented Flow Reactor for High-Temperature Synthesis: The Case Of Cdse Quantum Dots, *Angewandte Chemie*, 2005, **117**, 5583–5587.

[5] V. Kumar, H. A. Fustér, N. Oh, Y. Zhai, K. Deshpande, M. Shim and P. J. A. Kenis, Continuous flow synthesis of anisotropic cadmium selenide and zinc selenide nanoparticles, *ChemNanoMat*, 2017, **3**, 204–211.

[6] A. Vikram, V. Kumar, U. Ramesh, K. Balakrishnan, N. Oh, K. Deshpande, T. Ewers, P. Trefonas, M. Shim and P. J. A. Kenis, A Millifluidic Reactor System for Multistep Continuous Synthesis of InP/ZnSeS Nanoparticles, *ChemNanoMat*, 2018, **4**, 943–953.

[7] J. McMurry and R. C. Fay, *Chemistry*, Pearson Prentice Hall, 2008.

[8] *Quantum dots*, `https://www.sigmaaldrich.com/technical-documents/articles/materials-science/nanomaterials/quantum-dots.html`.

[9] P. Reiss, M. Protière and L. Li, Core/Shell Semiconductor Nanocrystals, *Small*, 2009, **5**, 154–168.

[10] M. J. Enright and B. M. Cossairt, Synthesis of Tailor-Made Colloidal Semiconductor Heterostructures, *Chemical Communications*, 2018, **54**, 7109–7122.

[11] Y. Jiang, S.-Y. Cho and M. Shim, Light-emitting diodes of colloidal quantum dots and nanorod heterostructures for future emissive displays, *Journal of Materials Chemistry C*, 2018, **6**, 2618–2634.

[12] A. M. Smith, L. A. Lane and S. Nie, Mapping the Spatial Distribution of Charge Carriers in Quantum-Confined Heterostructures, *Nature Communications*, 2014, **5**, 1–12.

[13] Y. Jang *et al.*, Interface Control of Electronic and Optical Properties in IV–VI and II–VI Core/Shell Colloidal Quantum Dots: A Review, *Chem. Commun.*, 2017, **53**, 1002–1024.

[14] C.-H. M. Chuang, P. R. Brown, V. Bulović and M. G. Bawendi, Improved Performance and Stability in Quantum Dot Solar Cells Through Band Alignment Engineering, *Nature Materials*, 2014, **13**, 796–801.

[15] H. Zhu, Y. Yang, K. Wu and T. Lian, Charge Transfer Dynamics from Photoexcited Semiconductor Quantum Dots, *Annual Review of Physical Chemistry*, 2016, **67**, 259–281.

[16] Y. Nandan and M. S. Mehata, Wavefunction Engineering of Type-I/Type-II Excitons of CdSe/CdS Core-Shell Quantum Dots, *Scientific Reports*, 2019, **9**, 2.

[17] S. Lambright *et al.*, Enhanced Lifetime of Excitons in Nonepitaxial Au/CdS Core/Shell Nanocrystals, *ACS Nano*, 2014, **8**, 352–361.

[18] H. McDaniel, M. Pelton, N. Oh and M. Shim, Effects of Lattice Strain and Band Offset on Electron Transfer Rates in Type-II Nanorod Heterostructures, *The Journal of Physical Chemistry Letters*, 2012, **3**, 1094–1098.

[19] L. R. Bradshaw, K. E. Knowles, S. McDowall and D. R. Gamelin, Nanocrystals for Luminescent Solar Concentrators, *Nano Letters*, 2015, **15**, 1315–1323.

[20] I. Coropceanu and M. G. Bawendi, Core/Shell Quantum Dot Based Luminescent Solar Concentrators with Reduced Reabsorption and Enhanced Efficiency, *Nano Letters*, 2014, **14**, 4097–4101.

[21] I. du Fossé, S. ten Brinck, I. Infante and A. J. Houtepen, Role of Surface Reduction in the Formation of Traps in n-Doped II–VI Semiconductor Nanocrystals: How to Charge without Reducing the Surface, *Chemistry of Materials*, 2019, **31**, 4575–4583.

[22] A. J. Houtepen, Z. Hens, J. S. Owen and I. Infante, On the Origin of Surface Traps in Colloidal II–VI Semiconductor Nanocrystals, *Chemistry of Materials*, 2017, **29**, 752–761.

[23] S. C. Boehme, J. M. Azpiroz, Y. V. Aulin, F. C. Grozema, D. Vanmaekelbergh, L. D. Siebbeles, I. Infante and A. J. Houtepen, Density of Trap States and Auger-mediated Electron Trapping in CdTe Quantum-Dot Solids, *Nano Letters*, 2015, **15**, 3056–3066.

[24] D. A. Wheeler and J. Z. Zhang, Exciton Dynamics in Semiconductor Nanocrystals, *Advanced Materials*, 2013, **25**, 2878–2896.

[25] A. M. Smith, A. M. Mohs and S. Nie, Tuning the optical and electronic properties of colloidal nanocrystals by lattice strain, *Nature Nanotechnology*, 2009, **4**, 56–63.

[26] S. Maiti, T. Debnath, P. Maity and H. N. Ghosh, Tuning the Charge Carrier Dynamics via Interfacial Alloying in Core/Shell CdTe/ZnSe NCs, *The Journal of Physical Chemistry C*, 2016, **120**, 1918–1925.

[27] E. Groeneveld, L. Witteman, M. Lefferts, X. Ke, S. Bals, G. Van Tendeloo and C. De Mello Donega, Tailoring ZnSe-CdSe Colloidal Quantum Dots via Cation Exchange: From Core/Shell to Alloy Nanocrystals, *ACS Nano*, 2013, **7**, 7913–7930.

[28] B. C. Fitzmorris, J. K. Cooper, J. Edberg, S. Gul, J. Guo and J. Z. Zhang, Synthesis and Structural, Optical, and Dynamic Properties of Core/Shell/Shell CdSe/ZnSe/ZnS Quantum Dots, *The Journal of Physical Chemistry C*, 2012, **116**, 25065–25073.

[29] D. V. Talapin, I. Mekis, S. Götzinger, A. Kornowski, O. Benson and H. Weller, CdSe/CdS/ZnS and CdSe/ZnSe/ZnS Core-Shell-Shell Nanocrystals, *The Journal of Physical Chemistry B*, 2004, **108**, 18826–18831.

[30] B. C. Fitzmorris, J. K. Cooper, J. Edberg, S. Gul, J. Guo and J. Z. Zhang, Synthesis and Structural, Optical, and Dynamic Properties of Core/Shell/Shell CdSe/ZnSe/ZnS Quantum Dots, *The Journal of Physical Chemistry C*, 2012, **116**, 25065–25073.

[31] K. Boldt, S. Bartlett, N. Kirkwood and B. Johannessen, Quantification of Material Gradients in Core/Shell Nanocrystals Using EXAFS Spectroscopy, *Nano Letters*, 2020, acs.nanolett.9b04143.

[32] S. Bisschop, P. Geiregat, T. Aubert and Z. Hens, The Impact of Core/Shell Sizes on the Optical Gain Characteristics of CdSe/CdS Quantum Dots, *ACS Nano*, 2018, **12**, 9011–9021.

[33] K. Boldt, Graded Shells in Semiconductor Nanocrystals, *Zeitschrift für Physikalische Chemie*, 2017, **231**, 77–92.

[34] F. García-Santamaría, S. Brovelli, R. Viswanatha, J. A. Hollingsworth, H. Htoon, S. A. Crooker and V. I. Klimov, Breakdown of Volume Scaling in Auger Recombination in Cdse/Cds Heteronanocrystals: The Role of the Core-Shell Interfacee, *Nano Letters*, 2011, **11**, 687–693.

[35] G. E. Cragg and A. L. Efros, Suppression of Auger Processes in Confined Structures, *Nano Letters*, 2010, **10**, 313–317.

[36] R. Xie, X. Zhong and T. Basché, Synthesis, Characterization, and Spectroscopy of Type-II Core/Shell Semiconductor Nanocrystals with ZnTe Cores, *Advanced Materials*, 2005, **17**, 2741–2745.

[37] S. Jin, J. Zhang, R. D. Schaller, T. Rajh and G. P. Wiederrecht, Ultrafast Charge Separation from Highly Reductive ZnTe/CdSe Type II Quantum Dots, *The Journal of Physical Chemistry Letters*, 2012, **3**, 2052–2058.

[38] Z.-J. Jiang and D. F. Kelley, Stranski–Krastanov Shell Growth in ZnTe/CdSe Core/Shell Nanocrystals, *The Journal of Physical Chemistry C*, 2013, **117**, 6826–6834.

[39] S. Jiao, Q. Shen, I. Mora-Seró, J. Wang, Z. Pan, K. Zhao, Y. Kuga, X. Zhong and J. Bisquert, Band Engineering in Core/Shell ZnTe/CdSe for Photovoltage and Efficiency Enhancement in Exciplex Quantum Dot Sensitized Solar Cells, *ACS Nano*, 2015, **9**, 908–915.

[40] T. Long, J. Cao and Z. J. Jiang, Predictable Spectroscopic Properties of Type-II ZnTe/CdSe Nanocrystals and Electron/Hole Quenching, *Physical Chemistry Chemical Physics*, 2019, **21**, 5824–5833.

[41] E. Groeneveld, S. van Berkum, M. M. van Schooneveld, A. Gloter, J. D. Meeldijk, D. J. van den Heuvel, H. C. Gerritsen and C. de Mello Donega, Highly Luminescent (Zn,Cd)Te/CdSe Colloidal Heteronanowires with Tunable Electron–Hole Overlap, *Nano Letters*, 2012, **12**, 749–757.

[42] M. J. Enright, H. Sarsito and B. M. Cossairt, Quantifying Cation Exchange of Cd^{2+} in ZnTe: A Challenge for Accessing Type II Heterostructures, *Chemistry of Materials*, 2017, **29**, 666–672.

[43] Z.-J. Jiang and D. F. Kelley, Effects of Inhomogeneous Shell Thickness in the Charge Transfer Dynamics of ZnTe/CdSe Nanocrystals, *The Journal of Physical Chemistry C*, 2012, **116**, 12958–12968.

[44] C. Y. Chen, C. T. Cheng, C. W. Lai, Y. H. Hu, P. T. Chou, Y. H. Chou and H. T. Chiu, Type-II CdSe/CdTe/ZnTe (Core-Shell-Shell) Quantum Dots with Cascade Band Edges: The Separation of Electron (at CdSe) and Hole (at ZnTe) by the CdTe Layer, *Small*, 2005, **1**, 1215–1220.

[45] M. Chudzicki, W. S. M. Werner, A. G. Shard, Y.-C. Wang, D. G. Castner and C. J. Powell, Evaluating the Internal Structure of Core-Shell Nanoparticles Using X-ray Photoelectron Intensities and Simulated Spectra., *The journal of physical chemistry. C, Nanomaterials and interfaces*, 2015, **119**, 17687–17696.

[46] B. G. Chae, J. H. Lee, S. Park, E. Lee, C. M. Kwak, M. Jafari, Y. K. Jeong, C. G. Park and J. B. Seol, Direct Three-Dimensional Observation of Core/Shell-Structured Quantum Dots with a Composition-Competitive Gradient, *ACS Nano*, 2018, **12**, 12109–12117.

[47] K. Tedsree, T. Li, S. Jones, C. W. A. Chan, K. M. K. Yu, P. A. J. Bagot, E. A. Marquis, G. D. W. Smith and S. C. E. Tsang, Hydrogen Production from Formic Acid Decomposition at Room Temperature Using a Ag–Pd Core–Shell Nanocatalyst, *Nature Nanotechnology*, 2011, **6**, 302–307.

[48] P. Felfer, P. Benndorf, A. Masters, T. Maschmeyer and J. M. Cairney, Revealing the Distribution of the Atoms within Individual Bimetallic Catalyst Nanoparticles, *Angewandte Chemie International Edition*, 2014, **53**, 11190–11193.

[49] P. Felfer, T. Li, K. Eder, H. Galinski, A. Magyar, D. Bell, G. Smith, N. Kruse, S. Ringer and J. Cairney, New Approaches to Nanoparticle Sample Fabrication for Atom Probe Tomography, *Ultramicroscopy*, 2015, **159**, 413–419.

[50] P. K. Jain, L. Amirav, S. Aloni and A. P. Alivisatos, Nanoheterostructure Cation Exchange: Anionic Framework Conservation, *Journal of the American Chemical Society*, 2010, **132**, 9997–9999.

[51] M. Shim, Colloidal Nanorod Heterostructures for Photovoltaics and Optoelectronics, *Journal of Physics D: Applied Physics*, 2017, **50**, 173002.

[52] S. Maiti, N. Ghorai, J. Dana and H. N. Ghosh, Disentangling the Electron and Hole Dynamics in Janus CdSe/PbSe Nanocrystals through Variable Pump Transient Absorption Spectroscopy, *The Journal of Physical Chemistry C*, 2018, **122**, 29075–29079.

[53] H. McDaniel, J.-M. Zuo and M. Shim, Anisotropic Strain-Induced Curvature in Type-II CdSe/CdTe Nanorod Heterostructures, *Journal of the American Chemical Society*, 2010, **132**, 3286–3288.

[54] A. Corrias, E. Conca, G. Cibin, G. Mountjoy, D. Gianolio, F. De Donato, L. Manna and M. F. Casula, Insights into the Structure of Dot@Rod and Dot@Octapod CdSe@CdS Heterostructures, *The Journal of Physical Chemistry C*, 2015, **119**, 16338–16348.

[55] L. Y. Chen, C. H. Chen, C. H. Tseng, F. L. Lai and B. J. Hwang, Synthesis $CdSe_xS_{1-x}$ Core/Shell Type Quantum Dots via One Injection Method, *Chemical Communications*, 2011, **47**, 1592–1594.

[56] I. J. Godfrey, A. J. Dent, I. P. Parkin, S. Maenosono and G. Sankar, Structure of Gold–Silver Nanoparticles, *The Journal of Physical Chemistry C*, 2017, **121**, 1957–1963.

[57] A. L. Bugaev *et al.*, Core-Shell Structure of Palladium Hydride Nanoparticles Revealed by Combined X-ray Absorption Spectroscopy and X-ray Diffraction, *Journal of Physical Chemistry C*, 2017, **121**, 18202–18213.

[58] H. Wei, J. Zhou, L. Zhang, F. Wang, J. Wang and C. Jin, The Core/Shell Structure of CdSe/ZnS Quantum Dots Characterized by X-Ray Absorption Fine Spectroscopy, *Journal of Nanomaterials*, 2015, **2015**, 1–7.

[59] L. Y. Chen, P. A. Yang, C. H. Tseng, B. J. Hwang and C. H. Chen, Internal Structure of Tunable Ternary $CdSe_xS_{1-x}$ Quantum Dots Unraveled by X-ray Absorption Spectroscopy, *Applied Physics Letters*, 2012, **100**, 163113.

[60] A. Saha, A. Shetty, A. R. Pavan, S. Chattopadhyay, T. Shibata and R. Viswanatha, Uniform Doping in Quantum-Dots-Based Dilute Magnetic Semiconductor, *Journal of Physical Chemistry Letters*, 2016, **7**, 2420–2428.

[61] D. Y. Cho, L. Xi, C. Boothroyd, B. Kardynal and Y. M. Lam, The Role of Ion Exchange in the Passivation of In(Zn)P Nanocrystals with ZnS, *Scientific Reports*, 2016, **6**, 22818.

[62] C. S. Schnohr and M. C. R. Editors, *X-Ray Absorption Spectroscopy of Semiconductors*, Springer Berlin Heidelberg, Berlin, Heidelberg, 2015, vol. 190.

[63] A. Balzarotti, N. Motta, A. Kisiel, M. Zimnal-Starnawska, M. T. Czyyk and M. Podgórny, Model of the Local Structure of Random Ternary Alloys: Experiment Versus Theory, *Physical Review B*, 1985, **31**, 7526–7539.

[64] J. C. Mikkelsen and J. B. Boyce, Atomic-Scale Structure of Random Solid Solutions: Extended X-Ray-Absorption Fine-Structure Study of $Ga_{1-x}In_xAs$, *Physical Review Letters*, 1982, **49**, 1412–1415.

[65] J. C. Mikkelsen and J. B. Boyce, Extended X-ray-Absorption Fine-Structure Study of $Ga_{1-x}In_xAs$ Random Solid Solutions, *Physical Review B*, 1983, **28**, 7130–7140.

[66] J. C. Woicik, J. G. Pellegrino, B. Steiner, K. E. Miyano, S. G. Bompadre, L. B. Sorensen, T.-L. Lee and S. Khalid, Bond-Length Distortions in Strained Semiconductor Alloys, *Physical Review Letters*, 1997, **79**, 5026–5029.

[67] J. C. Woicik, Random-Cluster Calculation of Bond Lengths in Strained-Semiconductor Alloys, *Physical Review B*, 1998, **57**, 6266–6269.

[68] G. M. Bhalerao *et al.*, High Pressure X-ray Diffraction and Extended X-Ray Absorption Fine Structure Studies on Ternary Alloy $Zn_{1x}Be_xSe$, *Journal of Applied Physics*, 2010, **108**, 083533.

[69] F. D'Acapito, Nearest-Neighbor Distances in Strained Thin Films of Random Pseudobinary Semiconductor Alloys: A Calculational Methodology, *Journal of Applied Physics*, 2004, **96**, 369–373.

[70] J. Timoshenko, D. Lu, Y. Lin and A. I. Frenkel, Supervised Machine-Learning-Based Determination of Three-Dimensional Structure of Metallic Nanoparticles, *The Journal of Physical Chemistry Letters*, 2017, **8**, 5091–5098.

[71] A. Witkowska, A. Di Cicco and E. Principi, Local Ordering of Nanostructured Pt Probed by Multiple-Scattering XAFS, *Physical Review B*, 2007, **76**, 104110.

[72] B. S. Clausen and J. K. Nørskov, Asymmetric Pair Distribution Functions in Catalysts, *Topics in Catalysis*, 2000, **10**, 221–230.

[73] A. Yevick and A. I. Frenkel, Effects of Surface Disorder on EXAFS Modeling of Metallic Clusters, *Physical Review B*, 2010, **81**, 115451.

[74] S. T. Chill, R. M. Anderson, D. F. Yancey, A. I. Frenkel, R. M. Crooks and G. Henkelman, Probing the Limits of Conventional Extended X-ray Absorption Fine Structure Analysis Using Thiolated Gold Nanoparticles, *ACS Nano*, 2015, **9**, 4036–4042.

[75] M. Kunisu, F. Oba, H. Ikeno, I. Tanaka and T. Yamamoto, Local Environment of Mn Dopant in ZnO by Near-Edge X-ray Absorption Fine Structure Analysis, *Applied Physics Letters*, 2005, **86**, 1–3.

[76] B. He, X. Zhang, S. Wei, H. Oyanagi, S. V. Novikov, K. W. Edmonds, C. T. Foxon, G. Zhou and Y. Jia, Local Structure Around Mn Atoms in Cubic (Ga,Mn)N Thin Films Probed by Fluorescence Extended X-Ray Absorption Fine Structure, url = http://aip.scitation.org/doi/10.1063/1.2168228, volume = 88, year = 2006, *Applied Physics Letters*, 1–3.

[77] S. Wei, W. Yan, Z. Sun, Q. Liu, W. Zhong, X. Zhang, H. Oyanagi and Z. Wu, Direct Determination of Mn Occupations in $Ga_{1-x}Mn_xN$ Dilute Magnetic Semiconductors by X-ray Absorption Near-Edge Structure Spectroscopy, *Applied Physics Letters*, 2006, **89**, 121901.

[78] Z. Sun *et al.*, Evidence of Substitutional Co Ion Clusters in Zn_{1-x} Co_x O Dilute Magnetic Semiconductors, *Physical Review B - Condensed Matter and Materials Physics*, 2008, **77**, 245208.

[79] J. Segura-Ruiz, G. Martínez-Criado, M. H. Chu, S. Geburt and C. Ronning, Nano-X-ray Absorption Spectroscopy of Single Co-Implanted ZnO Nanowires, *Nano Letters*, 2011, **11**, 5322–5326.

[80] Z. Sun *et al.*, Graphene Activating Room-Temperature Ferromagnetic Exchange in Cobalt-Doped Zno Dilute Magnetic Semiconductor Quantum Dots, *ACS Nano*, 2014, **8**, 10589–10596.

[81] W. Yan *et al.*, Realizing Ferromagnetic Coupling in Diluted Magnetic Semiconductor Quantum Dots, *Journal of the American Chemical Society*, 2014, **136**, 1150–1155.

[82] S. Coe-Sullivan, W. Liu, P. Allen and J. S. Steckel, Quantum Dots for LED Downconversion in Display Applications, *ECS Journal of Solid State Science and Technology*, 2013, **2**, R3026–R3030.

[83] B. T. Diroll, M. S. Kirschner, P. Guo and R. D. Schaller, Optical and Physical Probing of Thermal Processes in Semiconductor and Plasmonic Nanocrystals, *Annual Review of Physical Chemistry*, 2019, **70**, 353–377.

[84] L. X. Chen, X. Zhang and M. L. Shelby, Recent Advances on Ultrafast X-ray Spectroscopy in the Chemical Sciences, *Chem. Sci.*, 2014, **5**, 4136–4152.

[85] M.-F. Lin *et al.*, Carrier-Specific Femtosecond XUV Transient Absorption of PbI_2 Reveals Ultrafast Nonradiative Recombination, *The Journal of Physical Chemistry C*, 2017, **121**, 27886–27893.

[86] M. Chergui and E. Collet, Photoinduced Structural Dynamics of Molecular Systems Mapped by Time-Resolved X-ray Methods, *Chemical Reviews*, 2017, **117**, 11025–11065.

[87] L. X. Chen, Taking Snapshots of Photoexcited Molecules in Disordered Media by Using Pulsed Synchrotron X-rays, *Angewandte Chemie - International Edition*, 2004, **43**, 2886–2905.

[88] M. Chergui, Picosecond and Femtosecond X-ray Absorption Spectroscopy of Molecular Systems, *Acta Crystallographica Section A: Foundations of Crystallography*, 2010, **66**, 229–239.

[89] C. Bressler and M. Chergui, Molecular Structural Dynamics Probed by Ultrafast X-Ray Absorption Spectroscopy, *Annual Review of Physical Chemistry*, 2010, **61**, 263–282.

[90] L. Amidani, A. Naldoni, M. Malvestuto, M. Marelli, P. Glatzel, V. Dal Santo and F. Boscherini, Probing Long-Lived Plasmonic-Generated Charges in TiO_2/Au by High-Resolution X-ray Absorption Spectroscopy, *Angewandte Chemie International Edition*, 2015, **54**, 5413–5416.

[91] M. H. Rittmann-Frank, C. J. Milne, J. Rittmann, M. Reinhard, T. J. Penfold and M. Chergui, Mapping of the Photoinduced Electron Traps in TiO_2 by Picosecond X-ray Absorption Spectroscopy, *Angewandte Chemie International Edition*, 2014, **53**, 5858–5862.

[92] J. Huang, Y. Tang, K. L. Mulfort and X. Zhang, The Direct Observation of Charge Separation Dynamics in Cdse Quantum Dots/Cobaloxime Hybrids, *Phys. Chem. Chem. Phys.*, 2016, **18**, 4300–4303.

[93] J. E. Katz, X. Zhang, K. Attenkofer, K. W. Chapman, C. Frandsen, P. Zarzycki, K. M. Rosso, R. W. Falcone, G. a. Waychunas and B. Gilbert, Electron Small Polarons and Their Mobility in Iron (Oxyhydr)oxide Nanoparticles, *Science*, 2012, **337**, 1200–1203.

[94] Y. Tang, B. Pattengale, J. Ludwig, A. Atifi, A. V. Zinovev, B. Dong, Q. Kong, X. Zuo, X. Zhang and J. Huang, Direct Observation of Photoinduced Charge Separation in Ruthenium Complex/$Ni(OH)_2$ Nanoparticle Hybrid, *Scientific Reports*, 2015, **5**, 18505.

[95] M. W. Mara *et al.*, Electron Injection from Copper Diimine Sensitizers into TiO_2: Structural Effects and Their Implications for Solar Energy Conversion Devices, *Journal of the American Chemical Society*, 2015, **137**, 9670–9684.

[96] J. Huang *et al.*, Highly Efficient Ultrafast Electron Injection from the Singlet MLCT Excited State of Copper(I) Diimine Complexes to TiO_2 Nanoparticles, *Angewandte Chemie International Edition*, 2012, **51**, 12711–12715.

[97] X. Zhang, G. Smolentsev, J. Guo, K. Attenkofer, C. Kurtz, G. Jennings, J. V. Lockard, A. B. Stickrath and L. X. Chen, Visualizing Interfacial Charge Transfer in Ru-Dye-Sensitized TiO_2 Nanoparticles Using X-ray Transient Absorption Spectroscopy, *The Journal of Physical Chemistry Letters*, 2011, **2**, 628–632.

[98] F. Zamponi, T. J. Penfold, M. Nachtegaal, A. Lübcke, J. Rittmann, C. J. Milne, M. Chergui and J. a. van Bokhoven, Probing the Dynamics of Plasmon-Excited Hexanethiol-Capped Gold Nanoparticles by Picosecond X-Ray Absorption Spectroscopy, *Phys. Chem. Chem. Phys.*, 2014, **16**, 23157–23163.

[99] J. Ludwig, L. An, B. Pattengale, Q. Kong, X. Zhang, P. Xi and J. Huang, Ultrafast Hole Trapping and Relaxation Dynamics in p-Type CuS Nanodisks, *The Journal of Physical Chemistry Letters*, 2015, 2671–2675.

[100] F. G. Santomauro *et al.*, Localized Holes and Delocalized Electrons in Photoexcited Inorganic Perovskites: Watching Each Atomic Actor by Picosecond X-Ray Absorption Spectroscopy, *Structural Dynamics*, 2017, **4**, 044002.

[101] Y. Uemura, H. Uehara, Y. Niwa, S. Nozawa, T. Sato, S. Adachi, B. Ohtani, S. Takakusagi and K. Asakura, In Situ Picosecond XAFS Study of an Excited State of Tungsten Oxide, *Chemistry Letters*, 2014, **43**, 977–979.

[102] S. Bose, S. Shendre, Z. Song, V. K. Sharma, D. H. Zhang, C. Dang, W. Fan and H. V. Demir, Temperature-Dependent Optoelectronic Properties of Quasi-2D Colloidal Cadmium Selenide Nanoplatelets, *Nanoscale*, 2017, **9**, 6595–6605.

[103] J. H. Olshansky, A. D. Balan, T. X. Ding, X. Fu, Y. V. Lee and A. P. Alivisatos, Temperature-Dependent Hole Transfer from Photoexcited Quantum Dots to Molecular Species: Evidence for Trap-Mediated Transfer, *ACS Nano*, 2017, **11**, 8346–8355.

[104] R. R. Letfullin, T. F. George, G. C. Duree and B. M. Bollinger, Ultrashort Laser Pulse Heating of Nanoparticles: Comparison of Theoretical Approaches, *Advances in Optical Technologies*, 2008, **2008**, year.

[105] D. Kushavah, P. K. Mohapatra and P. Ghosh, Reduced Carrier Trapping in CdSe/ZnS/CdSe Heterostructure Quantum Dots Inferred from Temperature Dependent Spectral Studies, *Physica E: Low-dimensional Systems and Nanostructures*, 2018, **102**, 58–65.

[106] R. P. Sabatini, G. Bappi, K. T. Bicanic, F. Fan, S. Hoogland, M. I. Saidaminov, L. K. Sagar, O. Voznyy and E. H. Sargent, Temperature-Induced Self-Compensating Defect Traps and Gain Thresholds in Colloidal Quantum Dots, *ACS Nano*, 2019, **13**, 8970–8976.

[107] J. K. Utterback, J. L. Ruzicka, H. Hamby, J. D. Eaves and G. Dukovic, Temperature-Dependent Transient Absorption Spectroscopy Elucidates Trapped-Hole Dynamics in CdS and CdSe Nanorods, *The Journal of Physical Chemistry Letters*, 2019, **10**, 2782–2787.

[108] A. V. Malko, A. A. Mikhailovsky, M. A. Petruska, J. A. Hollingsworth and V. I. Klimov, Interplay Between Optical Gain and Photoinduced Absorption in CdSe Nanocrystals, *Journal of Physical Chemistry B*, 2004, **108**, 5250–5255.

[109] X. Wang *et al.*, Ultrafast Lattice Dynamics in Lead Selenide Quantum Dot Induced by Laser Excitation, *Applied Physics Letters*, 2016, **109**, 153105.

[110] M. S. Kirschner *et al.*, Transient Melting and Recrystallization of Semiconductor Nanocrystals Under Multiple Electron–Hole Pair Excitation, *Nano Letters*, 2017, **17**, 5314–5320.

[111] M. S. Kirschner *et al.*, Photoinduced, Reversible Phase Transitions in All-Inorganic Perovskite Nanocrystals, *Nature Communications*, 2019, **10**, 504.

[112] D. Hayes *et al.*, Electronic and Nuclear Contributions to Time-Resolved Optical and X-Ray Absorption Spectra of Hematite and Insights into Photoelectrochemical Performance, *Energy Environ. Sci.*, 2016, **9**, 3754–3769.

[113] J. Mahl *et al.*, Decomposing Electronic and Lattice Contributions in Optical Pump – X-ray Probe Transient Inner-Shell Absorption Spectroscopy of CuO, *Faraday Discussions*, 2019, **216**, 414–433.

[114] D. Attwood, *Soft X-Rays and Extreme Ultraviolet Radiation*, Cambridge University Press, 1999.

[115] S. Seltzer, *X-Ray Form Factor, Attenuation, and Scattering Tables*, 1995, `https://www.nist.gov/pml/x-ray-form-factor-attenuation-and-scattering-tables`.

[116] J. Als-Nielsen and D. McMorrow, *Elements of Modern X-ray Physics*, 2011.

[117] P. Willmott, *An Introduction to Synchrotron Radiation: Techniques and Applications*, 2011, pp. 1–352.

[118] B. K. Teo, *EXAFS: Basic Principles and Data Analysis*, 1986, vol. 9, p. 359.

[119] M. Newville, Fundamentals of XAFS, *Reviews in Mineralogy and Geochemistry*, 2014, **78**, 33–74.

[120] G. Bunker, *Introduction to XAFS: A Practical Guide to X-ray Absorption Fine Structure Spectroscopy*, Cambridge University Press, 2010, p. 260.

[121] *Reference X-ray Spectra of Metal Foils*, `http://exafsmaterials.com/`.

[122] J. J. Rehr, J. J. Kas, M. P. Prange, A. P. Sorini, Y. Takimoto and F. Vila, Ab Initio Theory and Calculations of X-ray Spectra, *Comptes Rendus Physique*, 2009, **10**, 548–559.

[123] R. Iwanowski and K. Ławniczak-Jabłońska, EXAFS Determination of Bond Lengths in $Z_{1-x}Fe_xS$ Ternary Alloys, *Acta Physica Polonica A*, 2016, **91**, 797–801.

[124] B. Ravel and M. Newville, ATHENA, ARTEMIS, HEPHAESTUS: Data Analysis for X-ray Absorption Spectroscopy Using IFEFFIT, *Journal of Synchrotron Radiation*, 2005, **12**, 537–541.

[125] S. Bordiga, S. Coluccia, C. Lamberti, L. Marchese, A. Zecchina, F. Boscherini, F. Buffa, F. Genoni and G. Leofanti, XAFS Study of Ti-Silicalite: Structure of Framework Ti(IV) in the Presence and Absence of Reactive Molecules ($H2_2O$, NH_3) and Comparison with Ultraviolet-Visible and IR Results, *The Journal of Physical Chemistry*, 1994, **98**, 4125–4132.

[126] D. Li, G. Bancroft, M. Kasrai, M. Fleet, X. Feng, K. Tan and B. Yang, High-Resolution Si K- and $L_{2,3}$-edge XANES of α-Quartz and Stishovite, *Solid State Communications*, 1993, **87**, 613–617.

[127] M. Benfatto and C. Meneghini, in *Synchrotron Radiation*, Springer Berlin Heidelberg, Berlin, Heidelberg, 2015, pp. 213–240.

[128] J. Rehr and A. Ankudinov, Progress in the Theory and Interpretation of XANES, *Coordination Chemistry Reviews*, 2005, **249**, 131–140.

[129] G. Smolentsev, S. E. Canton, J. V. Lockard, V. Sundstrom and L. X. Chen, Local Structure of Photoexcited Bimetallic Complexes Refined by Quantitative XANES Analysis, *Journal of Electron Spectroscopy and Related Phenomena*, 2011, **184**, 125–128.

[130] W. Xu, D. Chen, W. Chu, Z. Wu, A. Marcelli, A. Mottana, A. Soldatov and M. F. Brigatti, Quantitative Local Structure Determination in Mica Crystals: Ab Initio Simulations of Polarization XANES at the Potassium K-Edge, *Journal of Synchrotron Radiation*, 2011, **18**, 418–426.

[131] J. Bansmann, G. Kučerová, A. M. Abdel-Mageed, A. Abd El-Moemen and R. J. Behm, Influence of Re-activation and Ongoing CO Oxidation Reaction on the Chemical and Electronic Properties of Au on a Au/CeO_2 Catalyst: A XANES Study at the Au L_{III} Edge, *Journal of Electron Spectroscopy and Related Phenomena*, 2017, **220**, 86–90.

[132] Y. Joly, X-Ray Absorption Near-Edge Structure Calculations Beyond the Muffin-Tin Approximation, *Physical Review B*, 2001, **63**, 125120.

[133] J. J. Rehr and R. C. Albers, Theoretical Approaches to X-Ray Absorption Fine Structure, *Reviews of Modern Physics*, 2000, **72**, 621–654.

[134] J. J. Rehr, J. J. Kas, F. D. Vila, M. P. Prange and K. Jorissen, *Parameter-Free Calculations of X-Ray Spectra with FEFF9*, 2010, `http://xlink.rsc.org/?DOI=b926434e`.

[135] G. Donval, P. Moreau, J. Danet, S. J. S. Larbi, P. Bayle-Guillemaud and F. Boucher, A Hybrid Method Using the Widely-Used WIEN2k and VASP Codes to Calculate the Complete Set of XAS/EELS Edges in a Hundred-Atoms System, *Physical Chemistry Chemical Physics*, 2017, **19**, 1320–1327.

[136] K. Schwarz and P. Blaha, Computational Materials Science, 2003, pp. 259–273.

[137] F. Neese, The ORCA Program System, *Wiley Interdisciplinary Reviews: Computational Molecular Science*, 2012, **2**, 73–78.

[138] P. Giannozzi *et al.*, QUANTUM ESPRESSO: A Modular and Open-Source Software Project for Quantum Simulations of Materials, *Journal of Physics Condensed Matter*, 2009, **21**, 395502.

[139] O. Bunău and Y. Joly, Self-Consistent Aspects of X-Ray Absorption Calculations, *Journal of Physics: Condensed Matter*, 2009, **21**, 345501.

[140] S. A. Guda *et al.*, Optimized Finite Difference Method for the Full-Potential XANES Simulations: Application to Molecular Adsorption Geometries in MOFs and Metal–Ligand Intersystem Crossing Transients, *Journal of Chemical Theory and Computation*, 2015, **11**, 4512–4521.

[141] Y. Nicolau, Solution Deposition of Thin Solid Compound Films by a Successive Ionic-Layer Adsorption and Reaction Process, url = http://linkinghub.elsevier.com/retrieve/pii/0378596385902417, volume = 22-23, year = 1985, *Applications of Surface Science*, 1061–1074.

[142] A. M. Smith and S. Nie, Semiconductor Nanocrystals: Structure, Properties, and Band Gap Engineering, *Accounts of Chemical Research*, 2010, **43**, 190–200.

[143] L. De Trizio and L. Manna, Forging Colloidal Nanostructures via Cation Exchange Reactions, *Chemical Reviews*, 2016, **116**, 10852–10887.

[144] P. Yang, S. Wang, M. Ando and N. Murase, CdSe/$Cd_{1x}Zn_{\ x}S$ Core/Shell Quantum Dots with Tunable Emission: Growth and Morphology Evolution, *Journal of Materials Science*, 2013, **48**, 651–658.

[145] D. Dorfs, T. Franzl, R. Osovsky, M. Brumer, E. Lifshitz, T. A. Klar and A. Eychmüller, Type-I and Type-II Nanoscale Heterostructures Based on CdTe Nanocrystals: A Comparative Study, *Small*, 2008, **4**, 1148–1152.

[146] S. Kasap and P. Capper, Handbook of Electronic and Photonic Materials, *Materials Today*, 2006, **10**, 55.

[147] A. Kisiel, B. Robouch and A. Marcelli, Local Crystalline Structure of Multinary Semiconducting Alloys: Random Vs. Ordered Distributions, *Opto-Electronics Review*, 2017, **25**, 242–250.

[148] X. Cai, H. Mirafzal, K. Nguyen, V. Leppert and D. F. Kelley, Spectroscopy of CdTe/CdSe Type-II Nanostructures: Morphology, Lattice Mismatch, and Band-Bowing Effects, *Journal of Physical Chemistry C*, 2012, **116**, 8118–8127.

[149] *Partial Differential Equation Toolbox Documentation*, `https://www.mathworks.com/help/pde/index.html`.

[150] M. Şahin, S. Nizamoglu, O. Yerli and H. Volkan Demir, Reordering Orbitals of Semiconductor Multi-Shell Quantum Dot-Quantum Well Heteronanocrystals, *Journal of Applied Physics*, 2012, **111**, 023713.

[151] A. Rubio-Ponce, D. Olguín and I. Hernández-Calderón, Calculation of the Effective Masses of II-VI Semiconductor Compounds, *Superficies y vacío*, 2003, **16**, 26–28.

[152] J. Dong, K. Zhang, X. Li, Y. Qian, H. Zhu, D. Yuan, Q.-H. Xu, J. Jiang and D. Zhao, Ultrathin Two-Dimensional Porous Organic Nanosheets with Molecular Rotors for Chemical Sensing, *Nature Communications*, 2017, **8**, 1142.

[153] S. Adachi, *Properties of Semiconductor Alloys: Group-IV, III-V and II-VI Semiconductors*, Wiley, 2009, p. 400.

[154] G. Kresse and J. Furthmüller, Efficient Iterative Schemes for Ab Initio Total-Energy Calculations Using a Plane-Wave Basis Set, *Physical Review B*, 1996, **54**, 11169–11186.

[155] J. P. Perdew, K. Burke and M. Ernzerhof, Generalized Gradient Approximation Made Simple, *Physical Review Letters*, 1996, **77**, 3865–3868.

[156] A. V. Krukau, O. A. Vydrov, A. F. Izmaylov and G. E. Scuseria, Influence of the exchange screening parameter on the performance of screened hybrid functionals, *Journal of Chemical Physics*, 2006, **125**, 224106.

[157] G. Kresse and D. Joubert, From ultrasoft pseudopotentials to the projector augmented-wave method, *Physical Review B*, 1999, **59**, 1758–1775.

[158] A. Hjorth Larsen *et al.*, The Atomic Simulation Environment—a Python Library for Working with Atoms, *Journal of Physics: Condensed Matter*, 2017, **29**, 273002.

[159] P. Erhart, B. Sadigh, A. Schleife and D. Åberg, First-Principles Study of Codoping in Lanthanum Bromide, *Physical Review B*, 2015, **91**, 165206.

[160] L. Teles, J. Furthmüller, L. Scolfaro, J. Leite and F. Bechstedt, First-Principles Calculations of the Thermodynamic and Structural Properties of Strained $In_xGa_{1-x}N$ and $Al_xGa_{1-x}N$ Alloys, *Physical Review B - Condensed Matter and Materials Physics*, 2000, **62**, 2475–2485.

[161] F. D. Murnaghan, The Compressibility of Media under Extreme Pressures, *Proceedings of the National Academy of Sciences*, 1944, **30**, 244–247.

[162] *Overview of the Advanced Photon Source*, `https://www.aps.anl.gov/About/Overview`.

[163] G. Bunker, *Estimating Photon Flux from Ion Chamber Currents*, 1988, `http://gbxafs.iit.edu/training/Photon{\_}estimate.pdf`.

[164] L. Tröger, D. Arvanitis, K. Baberschke, H. Michaelis, U. Grimm and E. Zschech, Full Correction of The Self-Absorption in Soft-Fluorescence Extended X-Ray-Absorption Fine Structure, *Physical Review B*, 1992, **46**, 3283–3289.

[165] P. Pfalzer, J.-P. Urbach, M. Klemm, S. Horn, M. L. DenBoer, A. I. Frenkel and J. P. Kirkland, Elimination of Self-Absorption in Fluorescence Hard-X-Ray Absorption Spectra, *Physical Review B*, 1999, **60**, 9335–9339.

[166] D. C. Koningsberger and R. Prins, *X-Ray Absorption: Principles, Applications, Techniques of EXAFS, SEXAFS, and XANES*, Wiley, 1988, p. 673.

[167] A. M. March, A. Stickrath, G. Doumy, E. P. Kanter, B. Krässig, S. H. Southworth, K. Attenkofer, C. A. Kurtz, L. X. Chen and L. Young, Development of High-Repetition-Rate Laser Pump/X-Ray Probe Methodologies for Synchrotron Facilities, *Review of Scientific Instruments*, 2011, **82**, 073110.

[168] A. M. March *et al.*, Elucidation of the Photoaquation Reaction Mechanism in Ferrous Hexacyanide Using Synchrotron X-Rays with Sub-Pulse-Duration Sensitivity, url = http://aip.scitation.org/doi/10.1063/1.5117318, volume = 151, year = 2019, *The Journal of Chemical Physics*, 144306.

[169] J. R. Welty, G. L. Rorrer and D. G. Foster, *Fundamentals of Momentum, Heat, and Mass Transfer*.

[170] D. C. Hannah, J. D. Gezelter, R. D. Schaller and G. C. Schatz, Reverse Non-Equilibrium Molecular Dynamics Demonstrate That Surface Passivation Controls Thermal Transport at Semiconductor–Solvent Interfaces, *ACS Nano*, 2015, **9**, 6278–6287.

[171] C. M. Gentle, Y. Wang, T. N. Haddock, C. P. Dykstra and R. M. van der Veen, Internal Atomic-Scale Structure Determination and Band Alignment of II–VI Quantum Dot Heterostructures, *The Journal of Physical Chemistry C*, 2020, **124**, 3895–3904.

[172] S. Kim, B. Fisher, H.-J. Eisler and M. Bawendi, Type-II Quantum Dots: CdTe/CdSe(Core/Shell) and CdSe/ZnTe(Core/Shell) Heterostructures, *Journal of the American Chemical Society*, 2003, **125**, 11466–11467.

[173] M. A. Boles, D. Ling, T. Hyeon and D. V. Talapin, The Surface Science of Nanocrystals, *Nature Materials*, 2016, **15**, 141–153.

[174] C. Giansante and I. Infante, Surface Traps in Colloidal Quantum Dots: A Combined Experimental and Theoretical Perspective, *Journal of Physical Chemistry Letters*, 2017, **8**, 5209–5215.

[175] S. J. Lim, A. Schleife and A. M. Smith, Optical Determination of Crystal Phase in Semiconductor Nanocrystals, *Nature Communications*, 2017, **8**, 14849.

[176] M. C. Biesinger, L. W. Lau, A. R. Gerson and R. S. Smart, Resolving Surface Chemical States in XPS Analysis of First Row Transition Metals, Oxides And Hydroxides: Sc, Ti, V, Cu and Zn, *Applied Surface Science*, 2010, **257**, 887–898.

[177] A. V. Naumkin, A. Kraut-Vass, S. W. Gaarenstroom and C. J. Powell, *NIST X-ray Photoelectron Spectroscopy Database*, 2012, `https://srdata.nist.gov/xps/http://srdata.nist.gov/xps/Default.aspx`.

[178] M. S. Nashner, A. I. Frenkel, D. L. Adler, J. R. Shapley and R. G. Nuzzo, Structural Characterization of Carbon-Supported Platinum-Ruthenium Nanoparticles from the Molecular Cluster Precursor $PtRu_5C(CO)_{16}$, *Journal of the American Chemical Society*, 1997, **119**, 7760–7771.

[179] J. Rockenberger, L. Tröger, A. Kornowski, T. Vossmeyer, A. Eychmüller, J. Feldhaus and H. Weller, EXAFS Studies on the Size Dependence of Structural and Dynamic Properties of CdS Nanoparticles, *The Journal of Physical Chemistry B*, 1997, **101**, 2691–2701.

[180] B.-J. Hwang, L. S. Sarma, J.-M. Chen, C.-H. Chen, S.-C. Shih, G.-R. Wang, D.-G. Liu, J.-F. Lee and M.-T. Tang, Structural Models and Atomic Distribution of Bimetallic Nanoparticles as Investigated by X-ray Absorption Spectroscopy, *Journal of the American Chemical Society*, 2005, **127**, 11140–11145.

[181] J. Rockenberger, L. Tröger, A. L. Rogach, M. Tischer, M. Grundmann, H. Weller and A. Eychmüller, An EXAFS Study on Thiolcapped CdTe Nanocrystals, *Berichte der Bunsengesellschaft für physikalische Chemie*, 1998, **102**, 1561–1564.

[182] R. E. Bailey and S. Nie, Alloyed Semiconductor Quantum Dots: Tuning the Optical Properties without Changing the Particle Size., *Journal of the American Chemical Society*, 2003, **125**, 7100–6.

[183] S. Lee, J. C. Flanagan, J. Kim, A. J. Yun, B. Lee, M. Shim and B. Park, Efficient Type-II Heterojunction Nanorod Sensitized Solar Cells Realized by Controlled Synthesis of Core/Patchy-Shell Structure and CdS Cosensitization, *ACS Applied Materials and Interfaces*, 2019, **11**, 19104–19114.

[184] E. P. Jahrman *et al.*, An Improved Laboratory-Based X-Ray Absorption Fine Structure and X-Ray Emission Spectrometer for Analytical Applications in Materials Chemistry Research, *Review of Scientific Instruments*, 2019, **90**, 024106.

[185] E. A. Stern, Number of Relevant Independent Points in X-Ray-Absorption Fine-Structure Spectra, *Physical Review B*, 1993, **48**, 9825–9827.

[186] G. Materlik, J. E. Müller and J. W. Wilkins, L-Edge Absorption Spectra of the Rare Earths: Assessment of the Single-Particle Picture, *Phys. Rev. Lett.*, 1983, **50**, 267–270.

[187] R. D. Mattuck, *A Guide to Feynman Diagrams in the Many-Body Problem*, p. 429.

[188] P. Romaniello, S. Guyot and L. Reining, The Self-Energy Beyond GW: Local and Nnonlocal Vertex Corrections, *The Journal of Chemical Physics*, 2009, **131**, 154111.

[189] J. J. Rehr and R. C. Albers, Theoretical Approaches to X-Ray Absorption Fine Structure, *Reviews of Modern Physics*, 2000, **72**, 621–654.

[190] J. J. Rehr, Lars Hedin and the Quest for a Theory of Excited States, *Physica Scripta*, 2006, **T115**, 19–23.

[191] J. E. Penner-Hahn, in *Encyclopedia of Life Sciences*, John Wiley & Sons, Ltd, Chichester, UK, 2005.

[192] M. Marcus, L. Brus, C. Murray, M. Bawendi, A. Prasad and A. Alivisatos, EXAFS Studies of Cd Chalcogenide Nanocrystals, *Nanostructured Materials*, 1992, **1**, 323–335.

[193] M. M. Krause and P. Kambhampati, Linking Surface Chemistry to Optical Properties of Semiconductor Nanocrystals, *Physical Chemistry Chemical Physics*, 2015, **17**, 18882–18894.

[194] R. D. Shannon, Revised Effective Ionic Radii and Systematic Studies of Interatomic Distances in Halides and Chalcogenides, *Acta Crystallographica Section A*, 1976, **32**, 751–767.

[195] L. Vegard, Die Konstitution der Mischkristalle und die Raumfüllung der Atome, *Zeitschrift für Physik*, 1921, **5**, 17–26.

[196] J. Spitaler and S. K. Estreicher, Perspectives on the Theory of Defects, *Frontiers in Materials*, 2018, **5**, 70.

[197] C. R. Natoli, in *C. R. Natoli*, Springer, Berlin, Heidelberg, 1984, pp. 38–42.

[198] D. S. Sholl and J. A. Steckel, *Density Functional Theory*, Wiley, 2009.

[199] J. Perdew, Density Functional Theory and the Band Gap Problem, *Int. J. Quantum Chem.*, 1986, **19**, 497–523.

[200] A. Schleife, M. D. Neumann, N. Esser, Z. Galazka, A. Gottwald, J. Nixdorf, R. Goldhahn and M. Feneberg, Optical properties of In_2O_3 from Experiment and First-Principles Theory: Influence of Lattice Screening, *New J Phys*, 2018, **20**, 053016–13.

[201] I. N. Remediakis and E. Kaxiras, Band-Structure Calculations for Semiconductors within Generalized-Density-Functional Theory, *Physical Review B - Condensed Matter and Materials Physics*, 1999, **59**, 5536–5543.

[202] K. Gilmore, J. Vinson, E. L. Shirley, D. Prendergast, C. D. Pemmaraju, J. J. Kas, F. D. Vila and J. J. Rehr, Efficient Implementation of Core-Excitation Bethe-Salpeter Equation Calculations, *Computer Physics Communications*, 2015, **197**, 109–117.

[203] J. Vinson and J. J. Rehr, Ab Initio Bethe-Salpeter Calculations of the X-Ray Absorption Spectra of Transition Metals at the L-Shell Edges, *Physical Review B - Condensed Matter and Materials Physics*, 2012, **86**, 195135.

[204] A. Ankudinov and B. Ravel, Real-space multiple-scattering calculation and interpretation of x-ray-absorption near-edge structure, *Physical Review B - Condensed Matter and Materials Physics*, 1998, **58**, 7565–7576.

[205] C. Vorwerk, C. Cocchi and C. Draxl, Addressing electron-hole correlation in core excitations of solids: An all-electron many-body approach from first principles, *Physical Review B*, 2017, **95**, 155121.

[206] J. Vinson, J. J. Rehr, J. J. Kas and E. L. Shirley, Bethe-Salpeter Equation Calculations of Core Excitation Spectra, *Physical Review B - Condensed Matter and Materials Physics*, 2011, **83**, 115106.

[207] C. V. Shank, R. L. Fork, R. F. Leheny and J. Shah, Dynamics of Photoexcited GaAs Band-Edge Absorption with Subpicosecond Resolution, *Physical Review Letters*, 1979, **42**, 112–115.

[208] M. D. Peterson, L. C. Cass, R. D. Harris, K. Edme, K. Sung and E. A. Weiss, The Role of Ligands in Determining the Exciton Relaxation Dynamics in Semiconductor Quantum Dots, *Annual Review of Physical Chemistry*, 2014, **65**, 317–339.

[209] D. C. Hannah, N. J. Dunn, S. Ithurria, D. V. Talapin, L. X. Chen, M. Pelton, G. C. Schatz and R. D. Schaller, Observation of Size-Dependent Thermalization In CdSe Nanocrystals Using Time-Resolved Photoluminescence Spectroscopy, *Physical Review Letters*, 2011, **107**, 177403.

[210] V. I. Klimov and D. W. McBranch, Femtosecond 1P-to-1S Electron Relaxation in Strongly Confined Semiconductor Nanocrystals, *Physical Review Letters*, 1998, **80**, 4028–4031.

[211] P. Guyot-Sionnest, B. Wehrenberg and D. Yu, Intraband Relaxation in Cdse Nanocrystals and the Strong Influence of the Surface Ligands, *Journal of Chemical Physics*, 2005, **123**, 074709.

[212] A. Pandey and P. Guyot-Sionnest, Slow Electron Cooling in Colloidal Quantum Dots, *Science*, 2008, **322**, 929–932.

[213] V. Klimov, P. Haring Bolivar and H. Kurz, Hot-Phonon Effects in Femtosecond Luminescence Spectra of Electron-Hole Plasmas in CdS, *Physical Review B*, 1995, **52**, 4728–4731.

[214] R. Pässler, Basic Model Relations for Temperature Dependencies of Fundamental Energy Gaps in Semiconductors, *Physica Status Solidi (B) Basic Research*, 1997, **200**, 155–172.

[215] L. Viña, S. Logothetidis and M. Cardona, Temperature Dependence of the Dielectric Function of Germanium, *Physical Review B*, 1984, **30**, 1979–1991.

[216] Y. P. Varshni, Temperature Dependence of the Energy Gap in Semiconductors, *Physica*, 1967, **34**, 149–154.

[217] J. Wang, J. K. Carson, M. F. North and D. J. Cleland, A New Approach to Modelling the Effective Thermal Conductivity of Heterogeneous Materials, *International Journal of Heat and Mass Transfer*, 2006, **49**, 3075–3083.

[218] W. L. Ong, S. M. Rupich, D. V. Talapin, A. J. McGaughey and J. A. Malen, Surface Chemistry Mediates Thermal Transport in Three-Dimensional Nanocrystal Arrays, *Nature Materials*, 2013, **12**, 410–415.

[219] J. L. Brooks, C. L. Warkentin, D. Saha, E. L. Keller and R. R. Frontiera, Toward a Mechanistic Uunderstanding of Plasmon-Mediated Photocatalysis, *Nanophotonics*, 2018, **7**, 1697–1724.

[220] M. G. Williams, R. D. Tomlinson and M. J. Hampshire, X-Ray Determination of the Lattice Parameters and Thermal Expansion of Cadmium Telluride in the Temperature Range 20-420°C, *Solid State Communications*, 1969, **7**, 1831–1832.

[221] A. Hassan *et al.*, Charge Carriers Modulate the Bonding of Semiconductor Nanoparticle Dopants As Revealed by Time-Resolved X-ray Spectroscopy, *ACS Nano*, 2017, **11**, 10070–10076.

[222] A. Hassan, X. Zhang, C. Liu and P. T. Snee, Electronic Structure and Dynamics of Copper-Doped Indium Phosphide Nanocrystals Studied with Time-Resolved X-ray Absorption and Large-Scale DFT Calculations, *The Journal of Physical Chemistry C*, 2018, **122**, 11145–11151.

[223] W. Hu, J. Ludwig, B. Pattengale, S. Yang, C. Liu, X. Zuo, X. Zhang and J. Huang, Unravelling the Correlation of Electronic Structure and Carrier Dynamics in $CuInS_2$ Nanoparticles, *The Journal of Physical Chemistry C*, 2018, **122**, 974–980.

[224] Y. Obara *et al.*, Femtosecond Time-Resolved X-Ray Absorption Spectroscopy of Anatase TiO_2 Nanoparticles Using XFEL, *Structural Dynamics*, 2017, **4**, 044033.

[225] F. G. Santomauro *et al.*, Femtosecond X-ray Absorption Study of Electron Localization in Photoexcited Anatase $TiO2_2$, *Scientific Reports*, 2015, **5**, 14834.

[226] J. Chen, H. Zhang, I. V. Tomov, X. Ding and P. M. Rentzepis, Photochemistry and Electron-Transfer Mechanism of Transition Metal Oxalato Complexes Excited in the Charge Transfer Band, *Proceedings of the National Academy of Sciences*, 2008, **105**, 15235–15240.

[227] A. El Nahhas *et al.*, X-Ray Absorption Spectroscopy of Ground and Excited Rhenium-Carbonyl-Diimine Complexes: Evidence for a Two-Center Electron Transfer, *The journal of physical chemistry A*, 2013, **117**, 361–9.

[228] S. E. Canton *et al.*, Toward Highlighting the Ultrafast Electron Transfer Dynamics at the Optically Dark Sites of Photocatalysts, *The Journal of Physical Chemistry Letters*, 2013, **4**, 1972–1976.

[229] S. E. Canton *et al.*, Visualizing the Non-Equilibrium Dynamics of Photoinduced Intramolecular Electron Transfer with Femtosecond X-Ray Pulses, url = http://arxiv.org/abs/gr-qc/9809069 http://dx.doi.org/10.1080/01422419908228843 http://www.nature.com/articles/ncomms7359, volume = 6, year = 2015, *Nature Communications*, 6359.

[230] J. Huang *et al.*, A Strong Steric Hindrance Effect on Ground State, Excited State, and Charge Separated State Properties of a Cu^I-Diimine Complex Captured by X-Ray Transient Absorption Spectroscopy, *Dalton Trans.*, 2014, **43**, 17615–17623.

[231] G. C. O'Neil *et al.*, Ultrafast Time-Resolved X-ray Absorption Spectroscopy of Ferrioxalate Photolysis with a Laser Plasma X-ray Source and Microcalorimeter Array, *The Journal of Physical Chemistry Letters*, 2017, **8**, 1099–1104.

[232] Z. J. Li *et al.*, Tracking Co(I) Intermediate in Operando in Photocatalytic Hydrogen Evolution by X-ray Transient Absorption Spectroscopy and DFT Calculation, *Journal of Physical Chemistry Letters*, 2016, **7**, 5253–5258.

[233] J. Cheng, Y. Yang, Y. Li, P. Dong, Y. Wang and S. Liu, Electron Transfer and Local Atomic Displacement in Sr1-xCexFBiS2 Revealed by X-ray Absorption Spectroscopy, *Journal of Physical Chemistry C*, 2017, **121**, 8525–8530.

[234] C. Stamm *et al.*, Femtosecond Modification of Electron Localization and Transfer of Angular Momentum in Nickel, *Nature Materials*, 2007, **6**, 740–743.

[235] C. R. Natoli, in *C. R. Natoli*, Springer, Berlin, Heidelberg, 1983, pp. 43–56.

[236] Y. Uemura *et al.*, Dynamics of Photoelectrons and Structural Changes of Tungsten Trioxide Observed by Femtosecond Transient XAFS, *Angewandte Chemie International Edition*, 2016, **55**, 1364–1367.

[237] Y. Uemura *et al.*, Capturing Local Structure Modulations of Photoexcited $BiVO_4$ By Ultrafast Transient XAFS, *Chemical Communications*, 2017, **53**, 7314–7317.

[238] R. M. van der Veen *et al.*, Structural Determination of a Photochemically Active Diplatinum Molecule by Time-Resolved EXAFS Spectroscopy, *Angewandte Chemie International Edition*, 2009, **48**, 2711–2714.

[239] W. Gawelda, M. Johnson, F. M. F. de Groot, R. Abela, C. Bressler and M. Chergui, Electronic and Molecular Structure of Photoexcited $[Ru^{II}(bpy)_3]^{2+}$ Probed by Picosecond X-ray Absorption Spectroscopy, *Journal of the American Chemical Society*, 2006, **128**, 5001–5009.

[240] P. Wernet *et al.*, Orbital-Specific Mapping of the Ligand Exchange Dynamics of $Fe(CO)_5$ in Solution, *Nature*, 2015, **520**, 78–81.

[241] F. A. Lima, T. J. Penfold, R. M. van der Veen, M. Reinhard, R. Abela, I. Tavernelli, U. Rothlisberger, M. Benfatto, C. J. Milne and M. Chergui, Probing the Electronic And Geometric Structure of Ferric and Ferrous Myoglobins in Physiological Solutions by Fe K-Edge Absorption Spectroscopy, *Physical chemistry chemical physics : PCCP*, 2014, **16**, 1617–31.

[242] S. A. Wilson, E. Green, I. I. Mathews, M. Benfatto, K. O. Hodgson, B. Hedman and R. Sarangi, X-Ray Absorption Spectroscopic Investigation of The Electronic Structure Differences in Solution and Crystalline Oxyhemoglobin, *Proceedings of the National Academy of Sciences of the United States of America*, 2013, **110**, 16333–16338.

[243] E. Borfecchia *et al.*, X-ray Transient Absorption Structural Characterization of the ^{3}MLCT triplet excited state of cis-$[Ru(bpy)_2(py)_2]^{2+}$, *Dalton transactions (Cambridge, England : 2003)*, 2013, **42**, 6564–71.

[244] X. Zhang *et al.*, Highly Accurate Excited-State Structure of $[Os(bpy)2dcbpy]^{2+}$Determined by X-ray Transient Absorption Spectroscopy, *Journal of the American Chemical Society*, 2014, **136**, 8804–8809.

[245] T. J. Penfold *et al.*, Revealing Hole Trapping in Zinc Oxide Nanoparticles by Time-Resolved X-Ray Spectroscopy, *Nature Communications*, 2018, **9**, 478.

[246] S. Abdollahi Pour, B. Movaghar and M. Razeghi, Tight-Binding Theory for the Thermal Evolution of Optical Band Gaps in Semiconductors and Superlattices, *Physical Review B - Condensed Matter and Materials Physics*, 2011, **83**, 1–8.

[247] P. Lautenschlager, P. B. Allen and M. Cardona, Temperature Dependence of Band Gaps in Si and Ge, *Physical Review B*, 1985, **31**, 2163–2171.

[248] A. Walsh, J. L. F. Da Silva and S.-H. Wei, Origins of Band-Gap Renormalization in Degenerately Doped Semiconductors, *Physical Review B*, 2008, **78**, 075211.

[249] A. Kronenberger, A. Polity, D. M. Hofmann, B. K. Meyer, A. Schleife and F. Bechstedt, Structural, Electrical, and Ooptical properties of Hydrogen-Doped ZnO Films, *Physical Review B*, 2012, **86**, 115334.

[250] D. Manuel, D. Cabaret, C. Brouder, P. Sainctavit, A. Bordage and N. Trcera, Experimental Evidence of Thermal Fluctuations on the X-Ray Absorption Near-Edge Structure at the Aluminum K Edge, *Physical Review B - Condensed Matter and Materials Physics*, 2012, **85**, 224108.

[251] F. Farges and G. E. Brown, Ti-Edge XANES Studies of Ti Coordination and Disorder in Oxide Compounds: Comparison Between Theory and Experiment, *Physical Review B - Condensed Matter and Materials Physics*, 1997, **56**, 1809–1819.

[252] I. Jonane, A. Anspoks, G. Aquilanti and A. Kuzmin, High-Temperature X-Ray Absorption Spectroscopy Study of Thermochromic Copper Molybdate, *Acta Materialia*, 2019, **179**, 26–35.

[253] F. D. Vila, J. J. Rehr, H. H. Rossner and H. J. Krappe, Theoretical X-Ray Absorption Debye-Waller Factors, *Physical Review B - Condensed Matter and Materials Physics*, 2007, **76**, 014301.

[254] Z. K. Liu, S. L. Shang and Y. Wang, Fundamentals of Thermal Expansion and Thermal Contraction, *Materials*, 2017, **10**, year.

[255] M. Boucharef, S. Benalia, D. Rached, M. Merabet, L. Djoudi, B. Abidri and N. Benkhettou, First-Principles Study of the Electronic and Structural Properties Of $(CdTe)_n/(ZnTe)_n$ Superlattices, url = https://www.sciencedirect.com/science/article/pii/S0749603614003401, volume = 75, year = 2014, *Superlattices and Microstructures*, 818–830.

[256] A. Koide *et al.*, Photoinduced Anisotropic Distortion as the Electron Trapping Site of Tungsten Trioxide by Ultrafast W L1-Edge X-Ray Absorption Spectroscopy with Full Potential Multiple Scattering Calculations, *Physical Chemistry Chemical Physics*, 2020, **22**, 2615–2621.

[257] J. S. Owen, J. Park, P.-E. Trudeau and A. P. Alivisatos, Reaction Chemistry and Ligand Exchange at CadmiumSelenide Nanocrystal Surfaces, *Journal of the American Chemical Society*, 2008, **130**, 12279–12281.

[258] R. S. Selinsky, Q. Ding, M. S. Faber, J. C. Wright and S. Jin, Quantum Dot Nanoscale Heterostructures for Solar Energy Conversion, *Chem. Soc. Rev.*, 2013, **42**, 2963–2985.

[259] K. P. Acharya, E. Khon, T. O'Connor, T. O'Conner, I. Nemitz, A. Klinkova, R. S. Khnayzer, P. Anzenbacher and M. Zamkov, Heteroepitaxial Growth of Colloidal Nanocrystals onto Substrate Films via Hot-Injection routes., *ACS nano*, 2011, **5**, 4953–64.

[260] E. Cánovas, P. Moll, S. A. Jensen, Y. Gao, A. J. Houtepen, L. D. A. Siebbeles, S. Kinge and M. Bonn, Size-Dependent Electron Transfer from PbSe Quantum Dots to SnO_2 Monitored by Picosecond Terahertz Spectroscopy, *Nano Letters*, 2011, **11**, 5234–5239.

[261] E. Cánovas, H. Wang, M. Karakus and M. Bonn, Hot Electron Transfer from Pbse Quantum Dots Molecularly Bridged to Mesoporous Tin and Titanium Oxide Films, *Chemical Physics*, 2016, **471**, 54–58.

[262] B. R. Hyun, A. C. Bartnik, L. Sun, T. Hanrath and F. W. Wise, Control of Electron Transfer from Lead-Salt Nanocrystals to TiO_2, *Nano Letters*, 2011, **11**, 2126–2132.

[263] K. Tvrdy, P. A. Frantsuzov and P. V. Kamat, Photoinduced Electron Transfer from Semiconductor Quantum Dots to Metal Oxide Nanoparticles, *Proceedings of the National Academy of Sciences of the United States of America*, 2011, **108**, 29–34.

[264] B.-R. Hyun, Y.-W. Zhong, A. C. Bartnik, L. Sun, H. D. Abruña, F. W. Wise, J. D. Goodreau, J. R. Matthews, T. M. Leslie and N. F. Borrelli, Electron Injection from Colloidal Pbs Quantum Dots into Titanium Dioxide Nanoparticles, *ACS nano*, 2008, **2**, 2206–2212.

[265] H. Wang, E. R. McNellis, S. Kinge, M. Bonn and E. Cánovas, Tuning Electron Transfer Rates Through Molecular Bridges in Quantum Dot Sensitized Oxides, *Nano Letters*, 2013, **13**, 5311–5315.

[266] K. P. Acharya, T. R. Alabi, N. Schmall, N. N. Hewa-Kasakarage, M. Kirsanova, A. Nemchinov, E. Khon and M. Zamkov, Linker-Free Modification of TiO_2 Nanorods with PbSe Nanocrystals, *Journal of Physical Chemistry C*, 2009, **113**, 19531–19535.

[267] J. J. Pijpers, R. Koole, W. H. Evers, A. J. Houtepen, S. Boehme, C. De Mello Donegá, D. Vanmaekelbergh and M. Bonn, Spectroscopic Studies of Electron Injection in Quantum Dot Sensitized Mesoporous Oxide Films, *Journal of Physical Chemistry C*, 2010, **114**, 18866–18873.